CHAPTER 4

# Numerical and Experimental Results

## 4.1 INTRODUCTORY REMARKS

The spectral-domain moment-method (SDMM) formulation of Chapter 3 was implemented in the *C* programming language and, as such, this implementation can now be used to analyse any antenna configuration consisting of microstrip patches with capacitive feed probes. In this chapter, it is shown how this implementation can be applied to a variety of applications. Throughout most most of this chapter, the results of the SDMM are compared to those of two other commercial codes, as well as some measured results. The two commercial codes are IE3D from Zeland Software [186] and FEKO from EM Software and Systems [187], while the circuit analysis module of Sonnet, from Sonnet Software [188], was also used. The measurements were all performed at the Centre for Electromagnetism at the University of Pretoria. This facility houses a Scientific Atlanta compact antenna test range, integrated with a dedicated Hewlett-Packard 8510C vector network analyser. For more general *S*-parameter measurements, a Hewlett-Packard 8510B vector network analyser is also used. Antenna gain in this facility is typically measured by using the gain-transfer method.

The SDMM implementation is validated in Section 4.2 for isolated parts of the antenna structure. In Section 4.3, the new antenna elements are characterised in order to determine the effect of the various geometrical parameters on the behaviour of the different elements. In Section 4.4, a number of applications are presented. These include vertically- and horizontally-polarised arrays, as well as $\pm 45^{\circ}$ slant-polarised arrays. The latter are often required for cellular base-stations antennas. Finally, in Section 4.5, it is shown how the capacitive feed probes can be used with alternatively-shaped resonant patches.

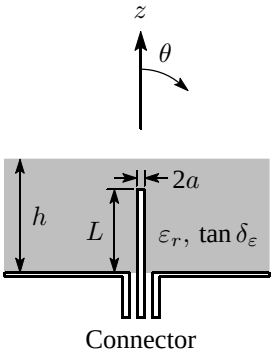


**Figure 4.1** Geometry of a probe that is embedded within a grounded substrate.

## 4.2 VALIDATION OF THE SPECTRAL-DOMAIN MOMENT-METHOD IMPLEMENTATION

In order to validate the accuracy of the SDMM implementation, it is advisable to first analyse isolated parts of the antenna structure. In doing so, one can obtain a better understanding of the capabilities of the formulation. The input impedance is usually a sensitive parameter and can give a good indication of how well the code performs. As such, it is used as the basis for comparison throughout most of the validation process. A single probe that is embedded within a grounded substrate, is probably the most basic part of the structure and is therefore firstly considered. Thereafter, the structure is extended by adding a capacitor patch to the probe, and finally a resonant patch. This then would be the equivalent of a single antenna element. A detailed investigation into the capabilities of the various attachment modes also forms part of this validation.

### 4.2.1 Single Probe in a Grounded Substrate

Consider the probe of Figure 4.1, with length $L$ and radius $a$, which is embedded within a grounded substrate of thickness $h$. The probe can be realised by extending the inner conductor of a coaxial cable through the ground plane into the substrate, while the outer conductor of the coaxial cable is connected to the ground plane. This problem has been addressed before and published results for the input impedance of such a probe are available within the open literature [189, 190].

Figure 4.2 shows simulated and published results for the input impedance versus normalised length of a probe that is totally embedded within a grounded substrate. For the SDMM formulation, between two and seven basis functions were used on the probe. It can be seen that the agreement between all the codes is very good and that it also compares exceptionally well with the published results.

Another interesting phenomena that can be validated here, is that far-field radiation towards the horizon (i.e. $\theta = \pm 90^{\circ}$) should always go down to zero, except under special conditions when the

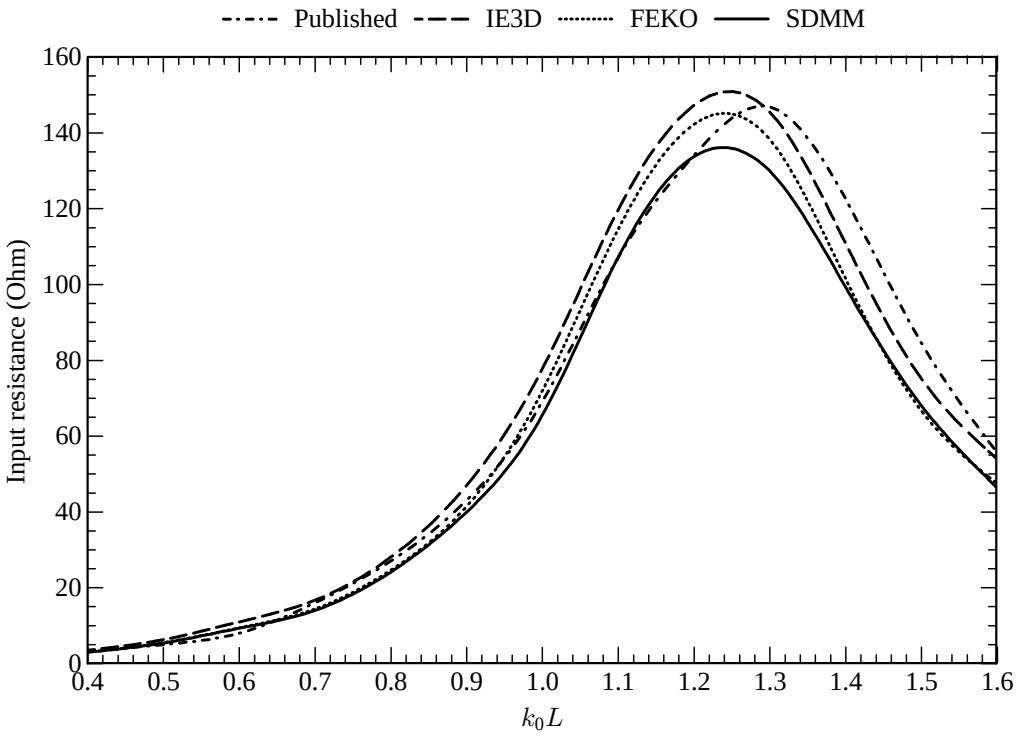


(a)

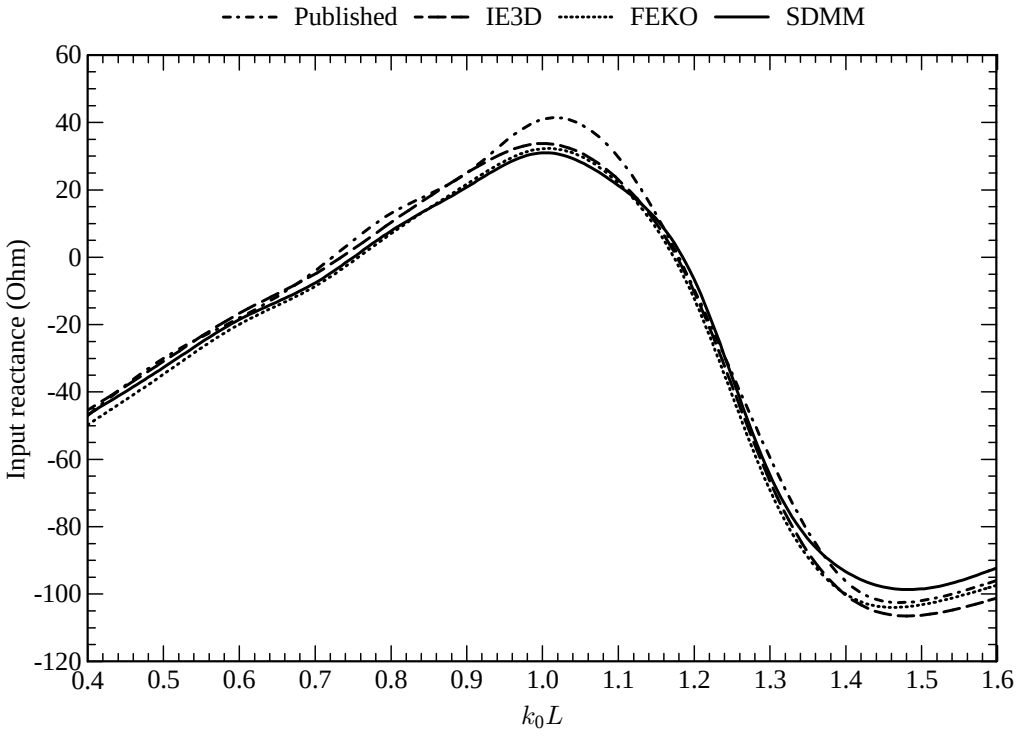


(b)

**Figure 4.2** Input impedance of a probe that is embedded within a grounded substrate. Parameters: $a$ = 1.5 mm, $h = 0.3\lambda_0$, $\varepsilon_r$ = 3.9 and $\tan\delta_\varepsilon = 0$. (a) Input resistance. (b) Input reactance.

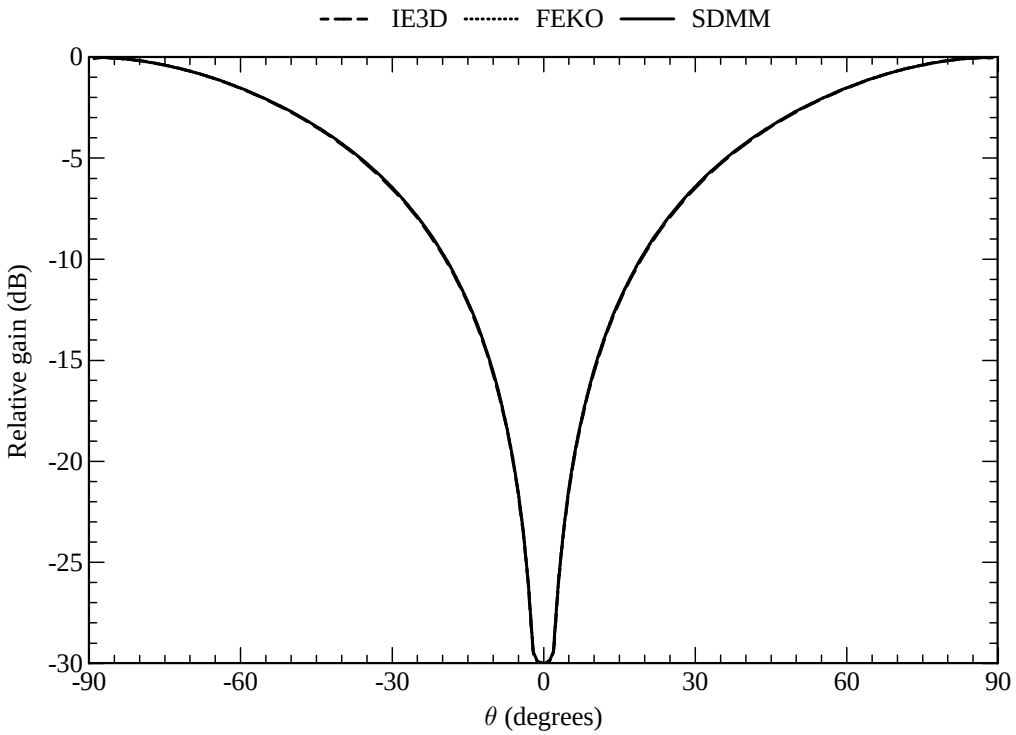


**Figure 4.3** Radiation pattern of a probe that is embedded within a grounded substrate. Parameters: $L$ = 48 mm, $a$ = 1.5 mm, $h$ = 90 mm, $\varepsilon_r$ = 3.78, tan $\delta_\varepsilon$ = 0 and $f$ = 1 GHz.

relation

$$h = \frac{i\lambda_0}{2\sqrt{\varepsilon_r - 1}}, \quad i = 1, 2, 3 \ldots \tag{4.1}$$

is satisfied [189, 191]. Figure 4.3 shows the radiation pattern for the case where $i = 1$. In this case, four basis functions were used on the probe. From this figure, it can indeed be seen that there is far-field radiation towards the horizon and that the results of the SDMM are virtually indistinguishable from those of the two commercial codes. Note that although there is radiation towards the horizon, all the codes give zero far fields at exactly $\theta = \pm 90^\circ$. This is due to the stationary-phase evaluation of the far fields.

From the results that have been presented here, it is clear that the SDMM, as implemented here, can model probes in multilayered substrates very successfully.

### 4.2.2 Circular Versus Rectangular Attachment Modes

In order to model the connection between a probe and a patch, a special basis function, also known as an attachment mode, is required. As discussed in Chapter 3, there are two common approaches: the rectangular attachment mode and the circular attachment mode. However, the performance of these attachment modes under a wide variety of geometrical parameters, is not well documented. In order to get a better understanding of the abilities of these two approaches, both of them are used

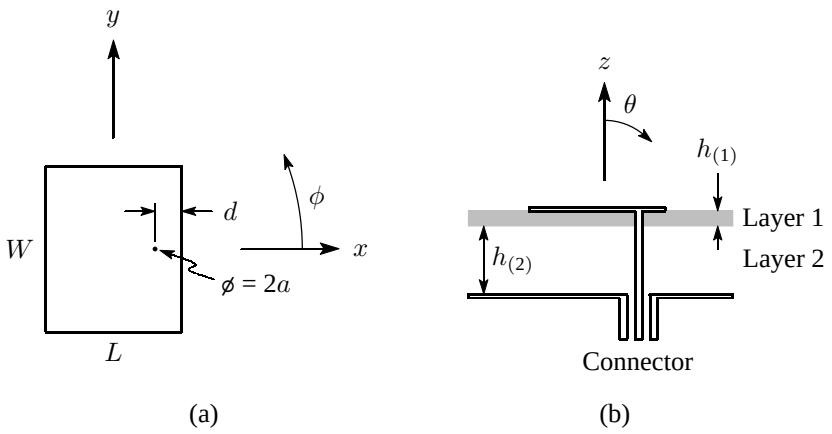


**Figure 4.4** Geometry of a rectangular probe-fed patch. (a) Top view of the patch. (b) Side view of the multilayered substrate.

in this section to analyse various rectangular probe-fed patch configurations. The general geometry of such a patch is shown in Figure 4.4. The simulated results are then compared to experimental results, which have either been published or measured specifically for this study. The simulated results are first compared to published results for a conventional narrowband microstrip antenna on a thin substrate, in order to verify that both approaches yield the correct results as claimed in the literature. Both approaches are then tested for small and resonant probe-fed patches that reside on multilayered substrates of varying thickness.

Shaubert *et al.* [192], as well as Aberle *et al.* [132,133], have published input-impedance results for a narrowband probe-fed microstrip patch antenna on a thin substrate. Figure 4.5 shows the input impedance of this antenna, as measured by them, together with two sets of numerical results that were calculated by using the two different attachment-mode approaches. Both sets of calculated results were obtained by using nine entire-domain sinusoidal basis functions on the patch and one piecewise sinusoidal (PWS) basis function (excluding the one associated with the attachment mode) on the probe. For the entire-domain sinusoidal basis functions, the (1,0), (1,2), (2,0), (3,0), (5,0), (7,0) and (9,0) modes were used for the $x$-directed current, while the (2,0) and (2,1) modes were used for the $y$-directed current. The best results for the circular attachment mode were achieved by extending the radius of the attachment mode to the closest edge of the patch. As can be seen from the results in Figure 4.5, both approaches are capable of generating results that agree very well with measurements. This is specifically for the case of a resonant patch on a relatively thin substrate.

It is not clear from the literature how the attachment modes would perform for much smaller patch sizes and thick substrates. To gain a better understanding of how they would perform, two sets of patches were constructed, the one set having resonant patches (at frequencies between 1.4 GHz and 2.1 GHz) of 50 mm $\times$ 50 mm, and the other set having much smaller patches (below

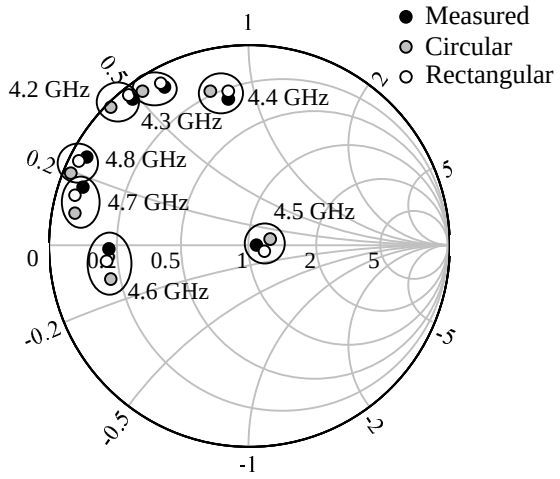


**Figure 4.5** Input impedance (normalised to 50 Ω) of a rectangular probe-fed patch as modelled with the circular and rectangular attachment modes. Parameters: $L$ = 9.5 mm, $W$ = 12.5 mm, $a$ = 0.45 mm, $d$ = 3.2 mm, $h_{(1)}$ = 1.27 mm, $\varepsilon_{r(1)}$ = 10.53, tan $\delta_{\varepsilon(1)}$ = 0.002 and $h_{(2)}$ = 0.

resonance) at 5 mm × 10 mm. Both sets contained four patches and were etched on a 1.6 mm layer of FR-4. Three of the four patches contained air gaps, ranging from more or less 5 mm to 15 mm, between the FR-4 layer and the ground plane. The two sets of patches would therefore represent a combination of different sizes and substrate thicknesses.

Figure 4.6 shows the measured and calculated input-impedance results for the set of resonant patches. Both sets of calculated results were obtained by using nine entire-domain basis functions on the patches, and one to seven PWS basis functions (excluding the one associated with the attachment mode) on the probe, depending on the substrate thickness. Once again, for the entire-domain sinusoidal basis functions, the (1,0), (1,2), (2,0), (3,0), (5,0), (7,0) and (9,0) modes were used for the $x$-directed current, while the (2,0) and (2,1) modes were used for the $y$-directed current. It is apparent that both attachment-mode approaches yield results that compare very well with the measured results. It would therefore appear that both approaches can handle thick multilayered substrates with very good accuracy, provided that the patch is of a resonant size. A radius of 10 mm provided the best results for the circular attachment mode.

Figure 4.7 shows the measured and calculated input-impedance results for the set of small patches. In this case, both sets of calculated results were obtained by using forty-five subdomain rooftop basis functions on the patches, and one to seven piecewise sinusoidal basis functions (excluding the one associated with the attachment mode) on the probe, depending on the substrate thickness. In this case it is clear that the circular attachment mode still yields results that compare favourably with the measurements, but that the rectangular attachment mode has difficulty in modelling the small patches. For all of the substrate thicknesses, it would appear as though the rectangular

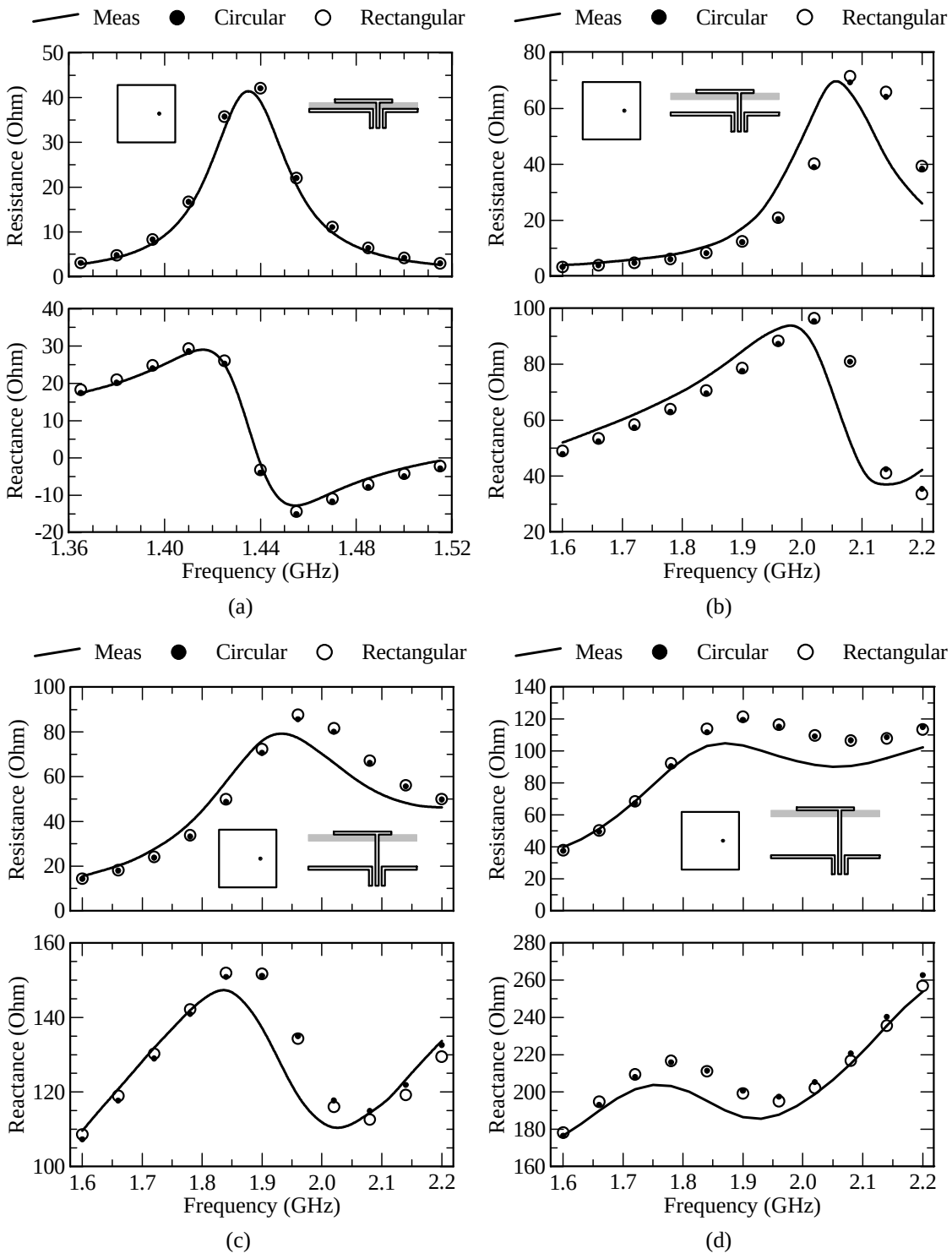


**Figure 4.6** Input impedance of a square resonant probe-fed patch as modelled with the circular and rectangular attachment modes. Parameters: $L$ = 50 mm, $W$ = 50 mm, $d$ = 15 mm, $h_{(1)}$ = 1.6 mm, $\varepsilon_{r(1)}$ = 4.25, $\tan\delta_{\varepsilon(1)}$ = 0.02 and $\tan\delta_{\varepsilon(2)}$ = 0. (a) $h_{(2)}$ = 0, $a$ = 0.64 mm. (b) $h_{(2)}$ = 5.4 mm, $a$ = 0.45 mm. (c) $h_{(2)}$ = 11.1 mm, $a$ = 0.45 mm. (d) $h_{(2)}$ = 15.8 mm, $a$ = 0.45 mm.

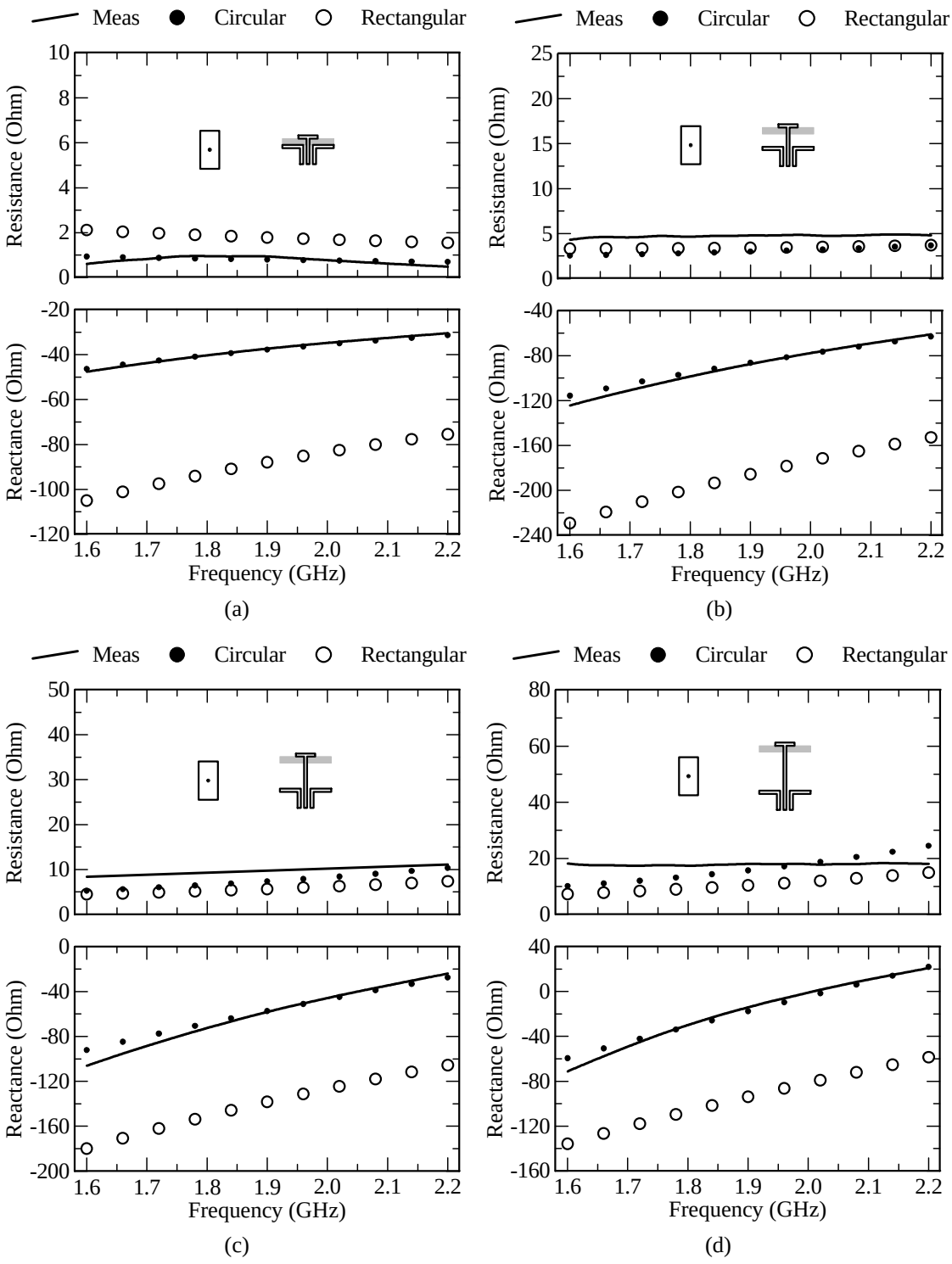


**Figure 4.7** Input impedance of a small rectangular probe-fed patch as modelled with the circular and rectangular attachment modes. Parameters: $L$ = 5 mm, $W$ = 10 mm, $d$ = 2.5 mm, $h_{(1)}$ = 1.6 mm, $\varepsilon_{r(1)}$ = 4.25, tan $\delta_{\varepsilon(1)}$ = 0.02 and tan $\delta_{\varepsilon(2)}$ = 0. (a) $h_{(2)}$ = 0, $a$ = 0.64 mm. (b) $h_{(2)}$ = 5.3 mm, $a$ = 0.45 mm. (c) $h_{(2)}$ = 10.2 mm, $a$ = 0.45 mm. (d) $h_{(2)}$ = 15.3 mm, $a$ = 0.45 mm.

attachment mode mainly yields an offset in the reactive part of the input impedance. In this case, the radius of the circular attachment mode was extended to the two closest edges for the best results.

This investigation was an attempt to gain a better understanding of the abilities of two widely-used attachment modes for a SDMM analysis of probe-fed microstrip patch antennas. It is clear from the results that have been presented here, that the circular attachment mode treats all patch sizes and substrate thicknesses with good accuracy, but that the rectangular attachment mode only works well for resonant patches, albeit it on thin and thick substrates. It would appear that the magnetic-wall cavity model with a uniform current filament source, upon which the rectangular attachment mode is based, is not a good approximation when dealing with very small patches, thereby resulting in the inaccuracies that have been observed. Some other benefits of the circular attachment mode over the rectangular attachment mode, is that it can be used with any shape of patch and that it is faster to evaluate. Furthermore, attachment modes, analogous to the rectangular attachment mode, which is based on the eigenmodes of the magnetic-wall cavity model, must be derived from scratch for other shapes of patches. One uncertainty related to the circular attachment mode, however, is the choice of the radius over which the current spreads on the surface of the patch. In all cases that were considered, the accuracy increased as the radius of the disk was increased. It has been stated by Taboada [108] that for triangular Rao, Wilton and Glisson (RWG) basis functions [104], the support of the attachment mode should be larger than the underlying subdomain basis functions. It also seems to be true in this case, implying that it should be possible to use a smaller radius for the attachment mode together with underlying subdomain basis functions, if these basis functions are also decreased in size. Finally, taking into account all of the observations, it would appear that the circular attachment mode is the more versatile of the two. The circular attachment mode, as well as a higher-order circular attachment mode that was developed in Chapter 3, will now be used to analyse both the circular and rectangular probe-fed capacitor patches.

### 4.2.3 Capacitor Patches

Following from the investigation into the attachment modes, it makes sense to retain only the circular attachment mode, as it is more versatile than the rectangular one. It will now be used to further validate the SDMM implementation in terms of its ability to model both the circular and rectangular probe-fed capacitor patches as shown in Figures 4.8 to 4.10.

Consider the circular capacitor patch as shown in Figure 4.8. The electric current density on the patch was modelled with only the circular attachment mode, having a radius of $b$, while the current density on the probe, having a radius of $a$, was modelled with four PWS basis functions (excluding the one associated with the attachment mode). Figure 4.11 shows the simulated input impedance of the circular capacitor patch, as a function of the probe radius. Additionally, it is also shown for two different radii of the capacitor patch. Here, SDMM refers to the implementation using the normal

circular attachment mode, while SDMM (HO) refers to the implementation using the higher-order circular attachment mode. It can be seen that the higher-order circular attachment mode predicts a slightly higher input reactance than the normal circular attachment mode. Furthermore, as far as the input reactance goes, the results for the higher-order circular attachment mode seem to follow the IE3D results rather closely, while the results of the normal circular attachment mode seem to be closer to the FEKO results. In general, however, all the results agree fairly well.

In order to make sure that the SDMM implementation can also calculate the coupling between two capacitor patches accurately, two probe-fed circular capacitor patches in fairly close proximity, were analysed. The geometry is shown in Figure 4.9. The same number of basis functions on each patch and probe was used as for the previous example. In this case, the higher-order circular attachment mode was used (the normal one basically gives the same results). Figure 4.12 shows the simulated coupling between the two capacitor patches. It can be seen that both the magnitude and the phase of the coupling, as predicted by the SDMM implementation, agrees very well with the results of both IE3D and FEKO.

Consider the rectangular capacitor patch as shown in Figure 4.10. The electric current density on the patch, having a size of $l \times w$, was modelled with subdomain rooftop basis functions, while the current density on the probe, having a radius of $a$, was modelled with four piecewise sinusoidal basis functions (excluding the one associated with the attachment mode). Figure 4.13 shows the simulated input impedance of the rectangular capacitor patch, as a function of the probe radius. Additionally, it is also shown for two sizes of the rectangular patch. For the patch size of 5 mm $\times$ 5 mm, twelve subdomain rooftop basis were used on the patch, while for the patch size of 5 mm $\times$ 20 mm, forty-seven were used. In both cases, a radius of 2.5 mm was used for the circular attachment mode. Once again, SDMM refers to the implementation using the normal circular attachment mode, while SDMM (HO) refers to the implementation using the higher-order circular attachment mode. In this case it can be seen that, apart from a small difference in the input reactance for the larger patch, there is not much difference between the results of the normal circular attachment mode and the higher-order version. For the small patch, there is good agreement between the various codes, but for the larger patch, there seem to be more variation in the results. Overall though, it would appear that the agreement is not far off.

The results in this section have shown that the SDMM implementation can model the probe-fed capacitor patches quite successfully. The validation will now continue by adding a square resonant patch to the structure, resulting in a single patch antenna element with a capacitive feed probe.

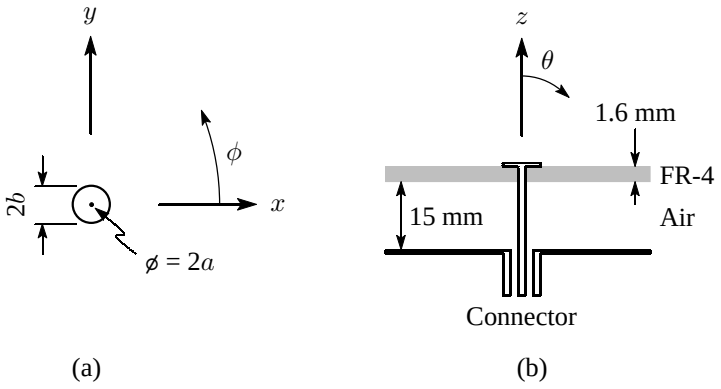


**Figure 4.8** Geometry of the circular capacitor patch. (a) Top view of the patch. (b) Side view of the multilayered substrate with $\varepsilon_r = 4.25$ and $\tan\delta_\varepsilon = 0.02$ for the FR-4 layer and with $\varepsilon_r = 1$ and $\tan\delta_\varepsilon = 0$ for the air layer.

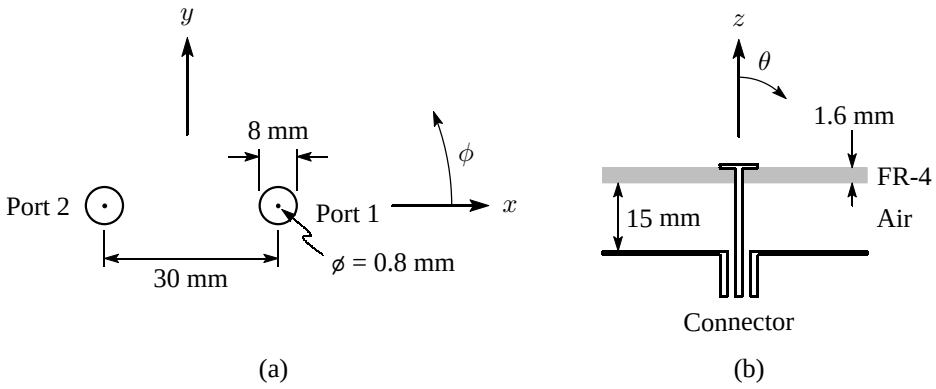


**Figure 4.9** Geometry of two circular capacitor patches in close proximity. (a) Top view of the patches. (b) Side view of the multilayered substrate with $\varepsilon_r = 4.25$ and $\tan\delta_\varepsilon = 0.02$ for the FR-4 layer and with $\varepsilon_r = 1$ and $\tan\delta_\varepsilon = 0$ for the air layer.

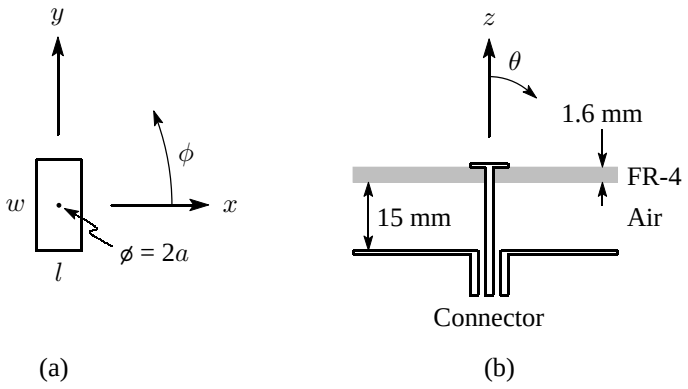


**Figure 4.10** Geometry of the rectangular capacitor patch. (a) Top view of the patch. (b) Side view of the multilayered substrate with $\varepsilon_r = 4.25$ and $\tan\delta_\varepsilon = 0.02$ for the FR-4 layer and with $\varepsilon_r = 1$ and $\tan\delta_\varepsilon = 0$ for the air layer.

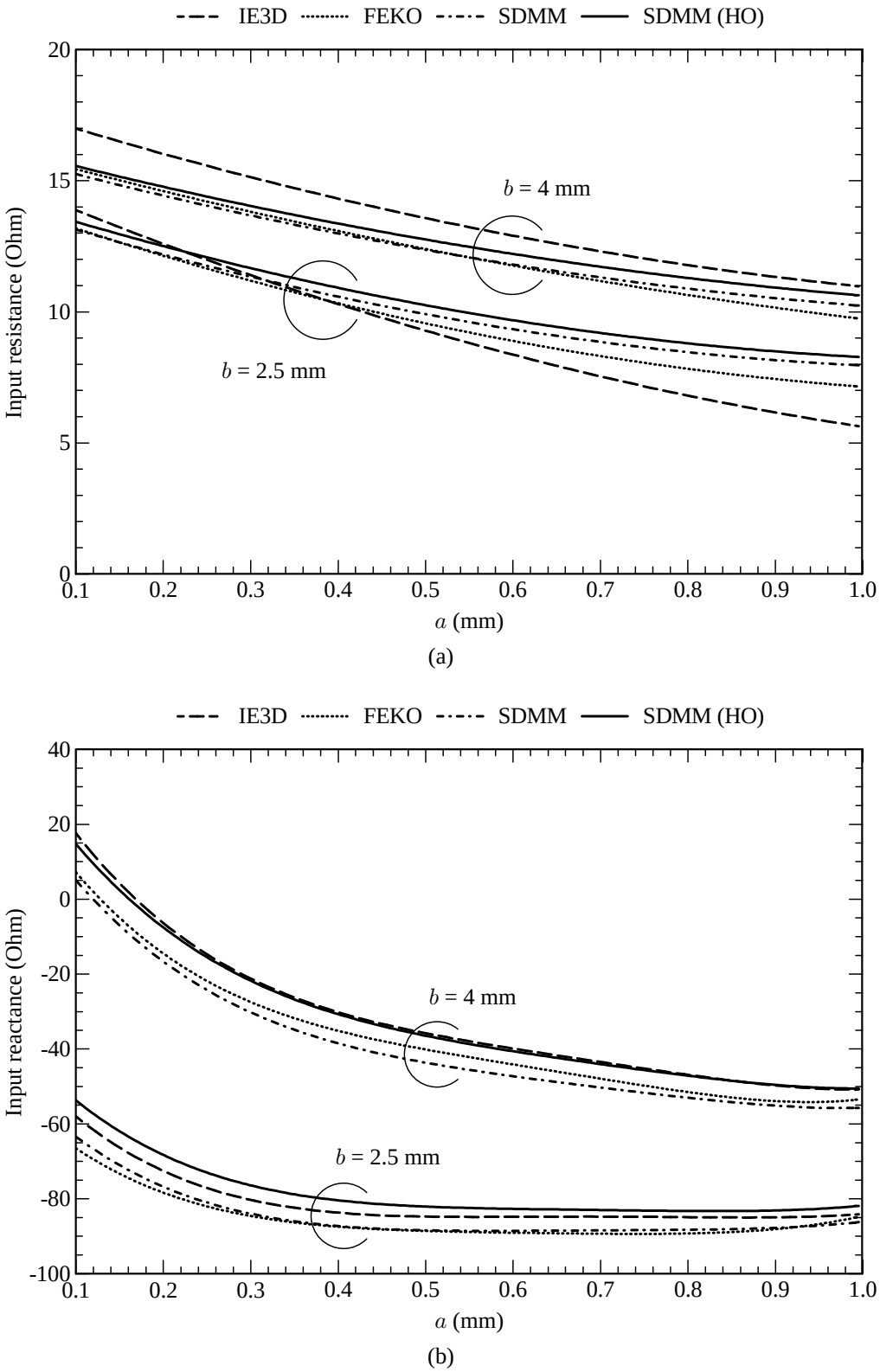


**Figure 4.11** Input impedance (at 1.8 GHz) of the circular capacitor patch. (a) Input resistance. (b) Input reactance.

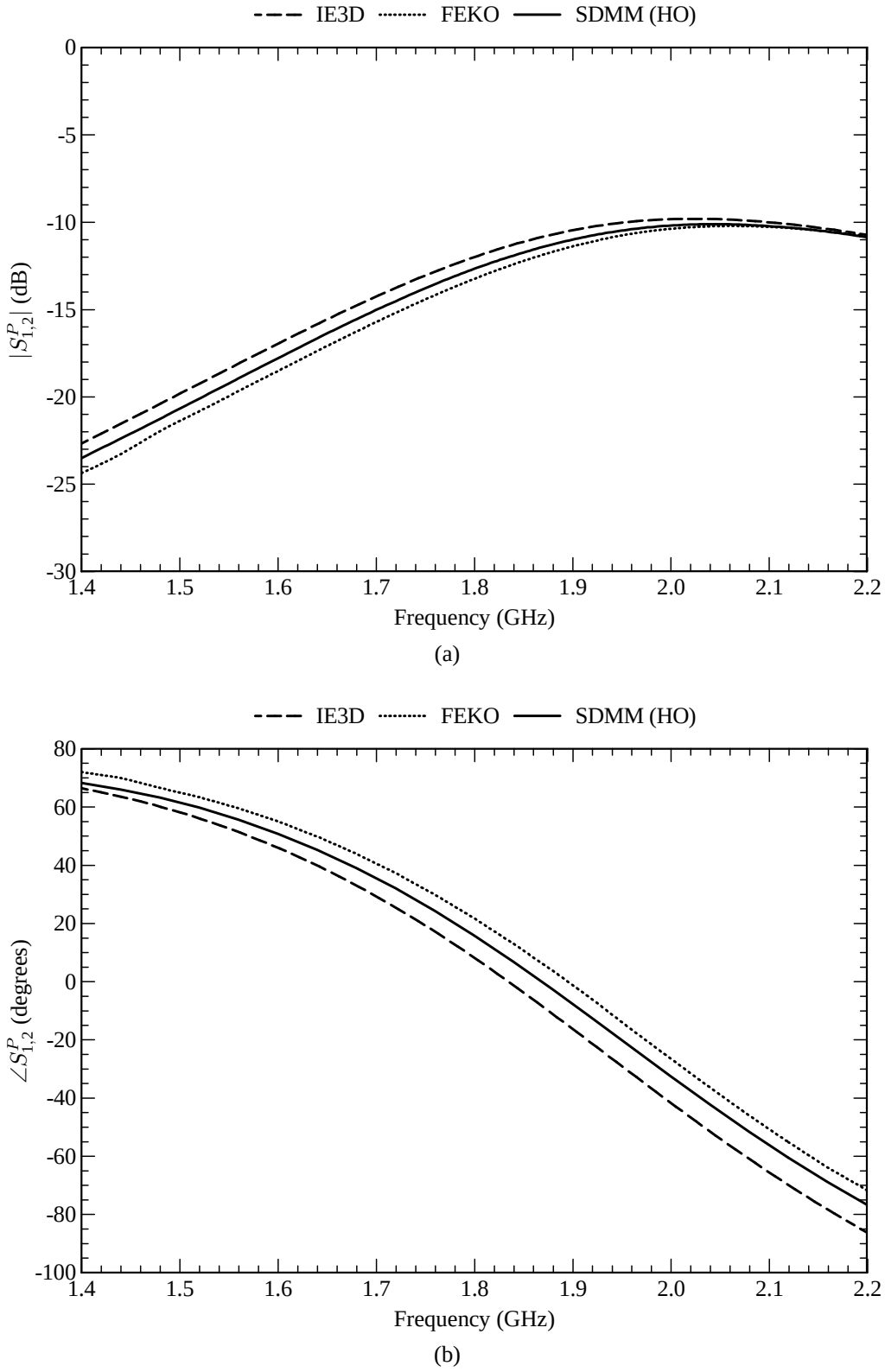


**Figure 4.12** Coupling between the two circular capacitor patches. (a) Magnitude. (b) Phase.

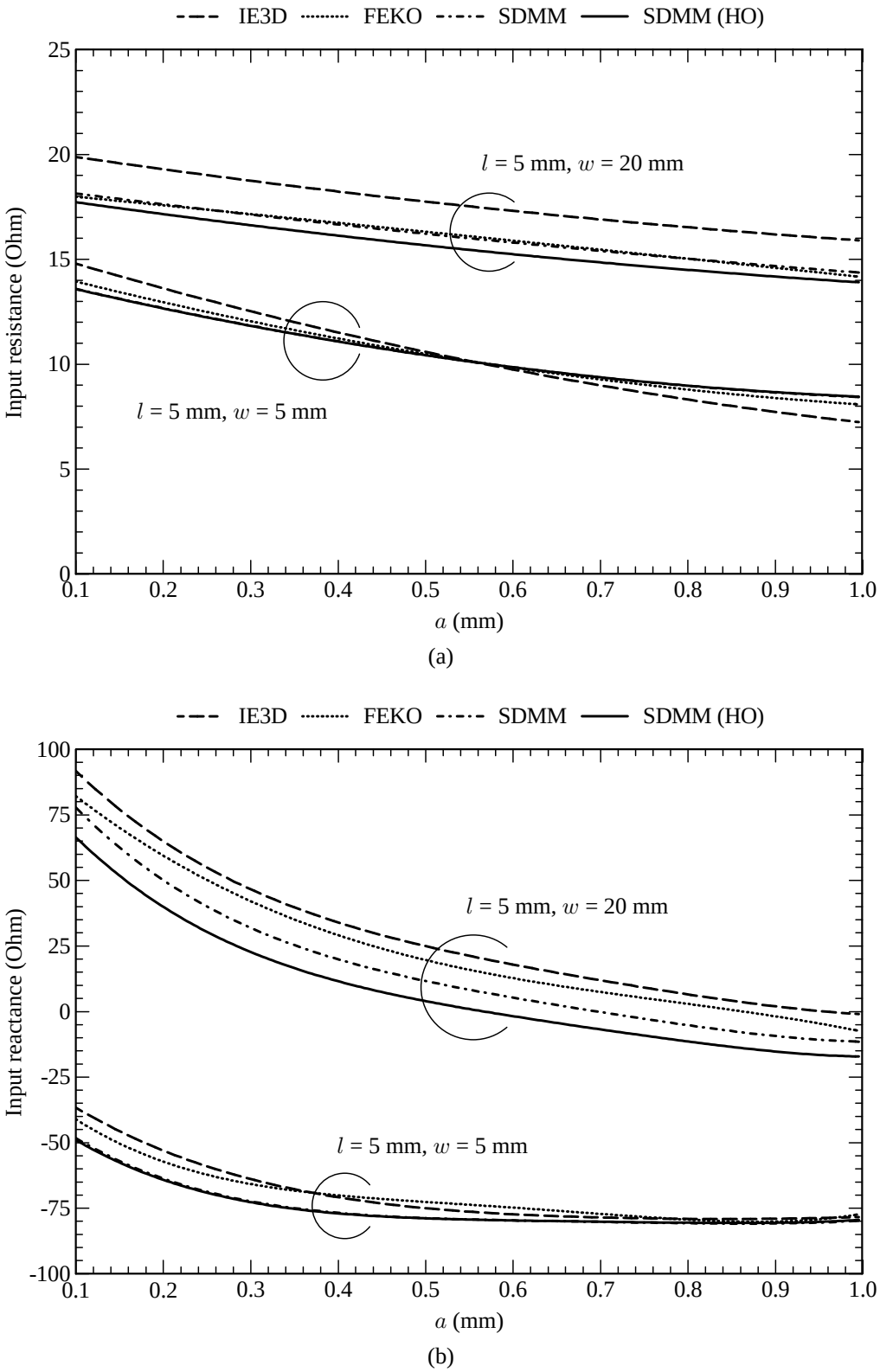


**Figure 4.13** Input impedance (at 1.8 GHz) of the rectangular capacitor patch. (a) Input resistance. (b) Input reactance.

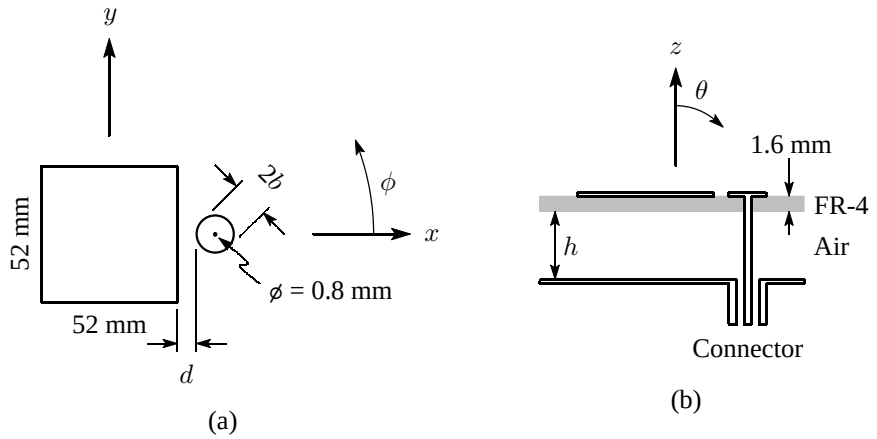


**Figure 4.14** Geometry of the antenna element with a circular capacitor patch. (a) Top view of the antenna element. (b) Side view of the multilayered substrate with $\varepsilon_r = 4.25$ and $\tan\delta_\varepsilon = 0.02$ for the FR-4 layer and with $\varepsilon_r = 1$ and $\tan\delta_\varepsilon = 0$ for the air layer.

### 4.2.4 Antenna Elements with Capacitive Feed Probes

The new antenna element is excited by making use of capacitive coupling through either a circular probe-fed capacitor patch or a rectangular probe-fed capacitor patch. In terms of validating the SDMM implementation, both configurations will now be considered.

First consider the antenna element with a circular capacitor patch, as shown in Figure 4.14. In order to obtain a better understanding in terms of the choice and number of basis functions that are required to model the antenna element, Figures 4.15 and 4.16 provide some convergence tests. The results in Figure 4.15 show how the input impedance of the antenna varies as a function of the number of sinusoidal entire-domain modes on the resonant patch when keeping the number of segments on the probe fixed. Each curve in Figures 4.15(a) and (b) starts with the (1,0) $x$-directed mode on the left-hand side of the $x$ axis, after which other $x$-directed modes are added accumulatively as one moves towards the right-hand side of the $x$ axis (i.e. for a specific $x$-directed mode, all the modes towards its left are also included). Furthermore, in the two graphs, each curve corresponds with a specific number of $y$-directed modes. The first curve assumes that there is no $y$-directed mode, after which $y$-directed modes are added accumulatively for the rest of the curves. From these results it can definitely be seen that the results converge as the number of $x$- and $y$-directed modes is increased. The results in Figure 4.16 show how the input impedance of the antenna varies as a function of the number of segments on the probe (each full PWS basis function spans two adjacent segments) when keeping the number of sinusoidal entire-domain basis functions on the resonant patch fixed. Here too, it can be seen that the results converge as the number of segments is increased.

Based on the convergence tests, the electric current density on the structure was finally modelled with eleven entire-domain sinusoidal basis functions on the resonant patch, the single circular

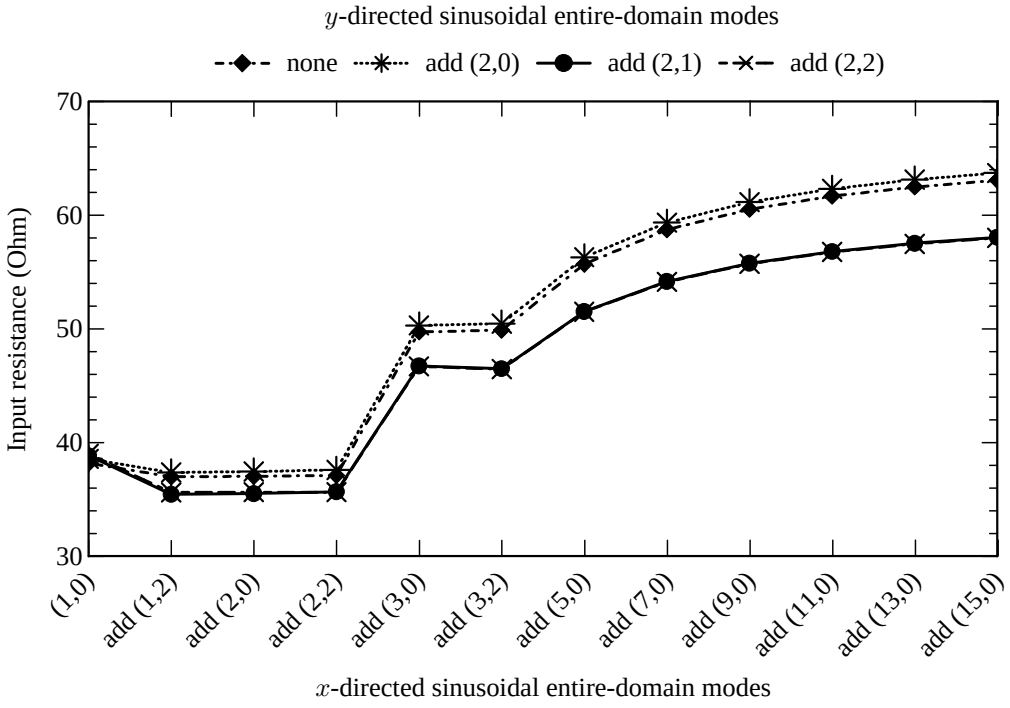


(a)

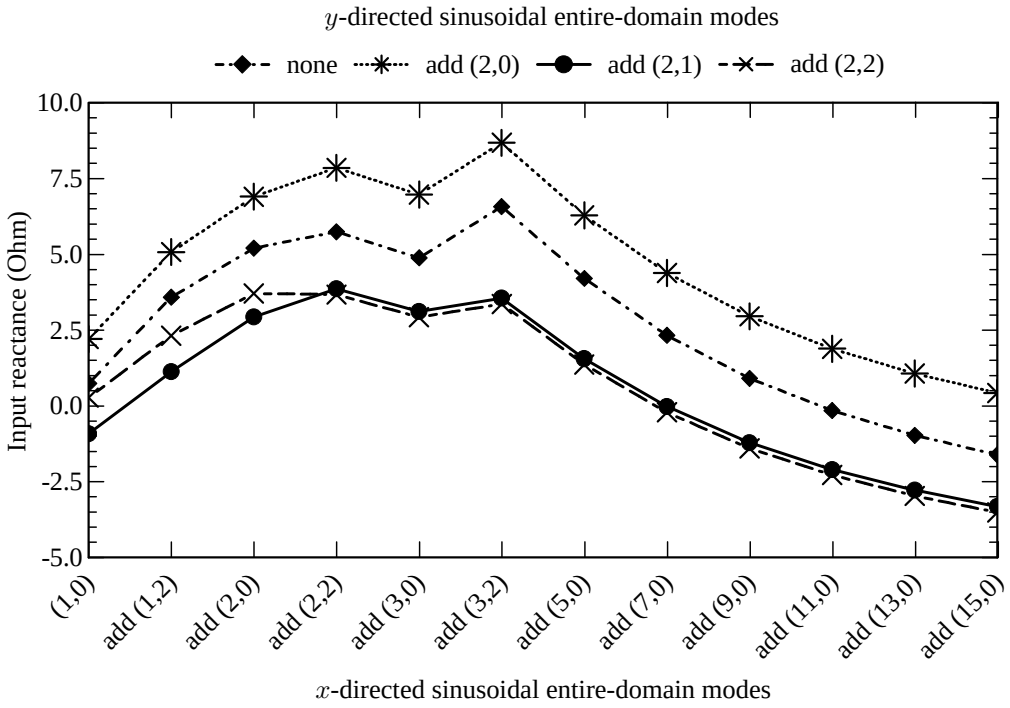


(b)

**Figure 4.15** Input impedance (at 1.8 GHz and with four segments on the probe) of the antenna element with a circular capacitor patch, but as a function of the entire-domain sinusoidal basis functions on the resonant patch. Parameters: $b$ = 4.5 mm and $d$ = 4 mm. (a) Input resistance. (b) Input reactance.

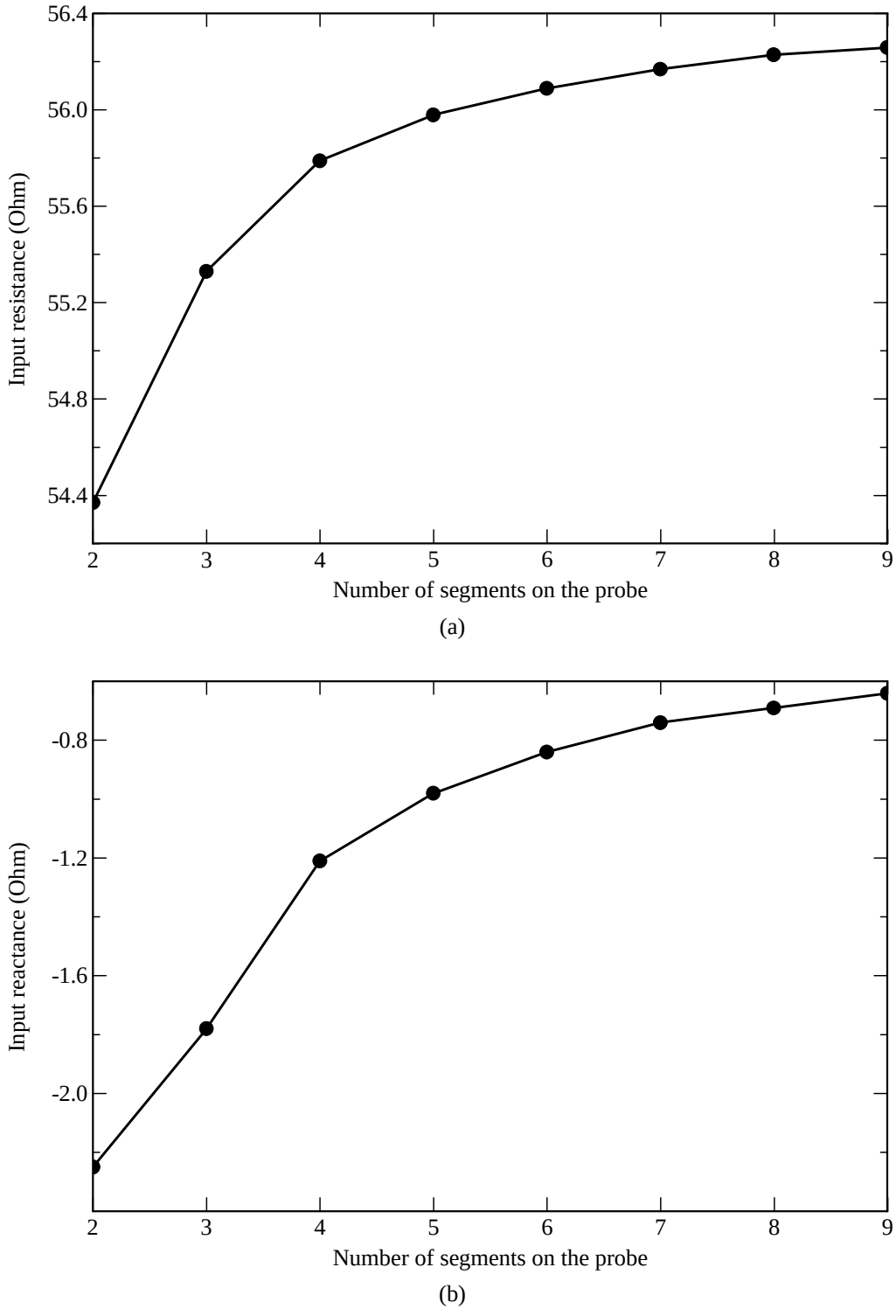


**Figure 4.16** Input impedance (at 1.8 GHz) of the antenna element with a circular capacitor patch, but as a function of the number of segments on the probe. For the entire-domain sinusoidal basis functions on the resonant patch, the (1,0), (1,2), (2,0), (2,2), (3,0), (3,2), (5,0), (7,0) and (9,0) modes were used for the $x$-directed current, while the (2,0) and (2,1) modes were used for the $y$-directed current. Parameters: $b$ = 4.5 mm and $d$ = 4 mm. (a) Input resistance. (b) Input reactance.

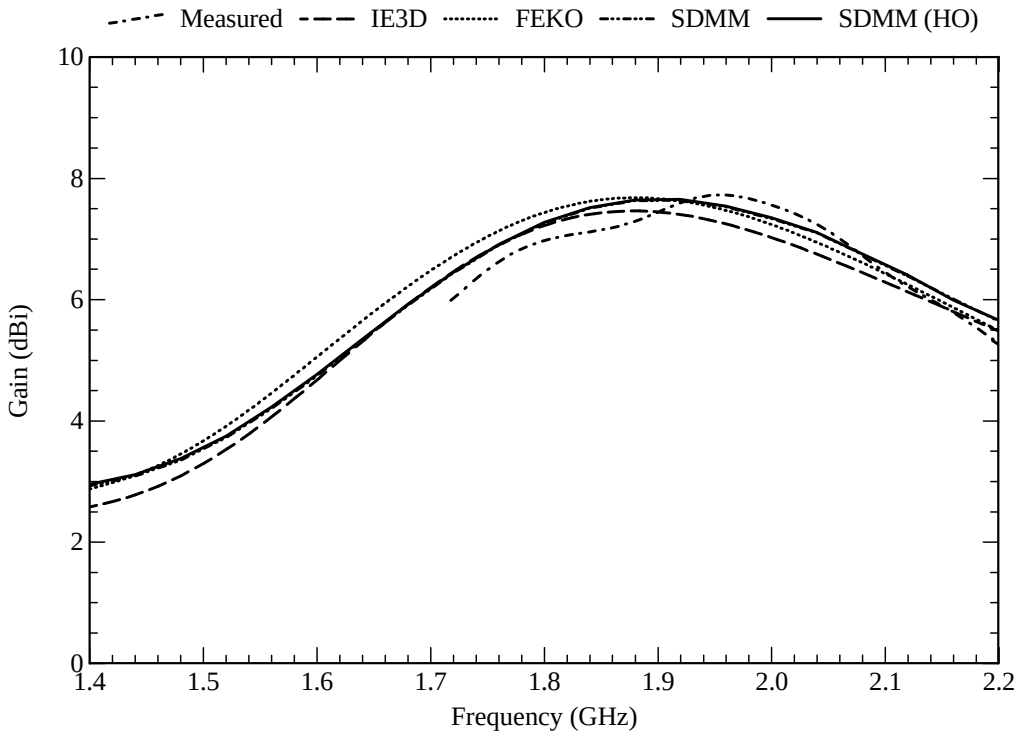


**Figure 4.17** Gain of the patch antenna with a circular capacitor patch. Parameters: $b$ = 4.5 mm and $d$ = 4 mm.

attachment mode on the capacitor patch, and four PWS basis functions on the probe (excluding the one associated with the attachment mode). For the entire-domain sinusoidal basis functions, the (1,0), (1,2), (2,0), (2,2), (3,0), (3,2), (5,0), (7,0) and (9,0) modes were used for the $x$-directed current, while the (2,0) and (2,1) modes were used for the $y$-directed current. The electric current density on the resonant patch is primarily directed along the $x$ direction. Figure 4.17 shows the simulated and measured gain of the antenna element, from which it can be seen that the agreement between the three codes and the measurements, is very good. Here, SDMM refers to the implementation using the normal circular attachment mode, while SDMM (HO) refers to the implementation using the higher-order circular attachment mode. As can be seen, there is practically no difference in the results obtained with the two circular attachment modes. Figure 4.18 shows the simulated and measured input impedance of the antenna element, from which it can also be seen that the agreement between the three codes and the measurements, is fairly good. The simulation with the higher-order circular attachment mode appears to provide results that agree better with those of the two commercial codes and the measurements than that of the normal circular attachment mode, especially for the reactive part of the input impedance. Figure 4.19 shows the simulated radiation patterns in the *E*-plane and the *H*-plane of the antenna element. From these it can be seen that, once again, the agreement between the three codes is fairly good, while there is practically no difference in the results obtained with the two circular attachment modes. The cross-polarised pattern in the *E*-plane of the antenna element is very low and therefore has not

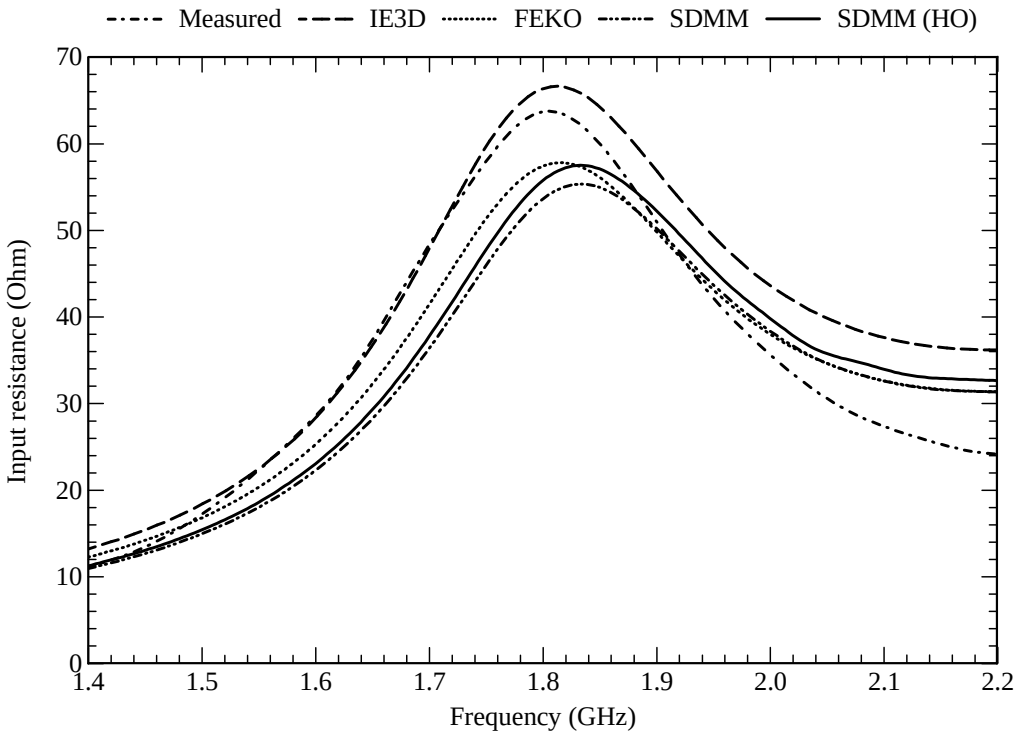


(a)

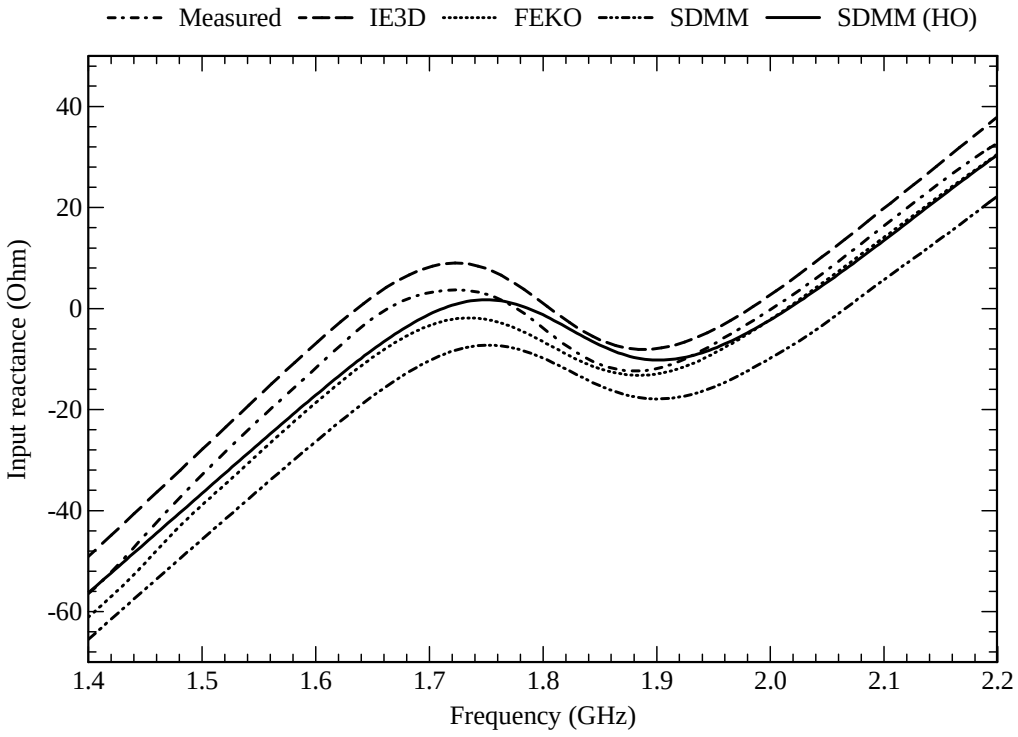


(b)

**Figure 4.18** Input impedance of the antenna element with a circular capacitor patch. Parameters: $b$ = 4.5 mm and $d$ = 4 mm. (a) Input resistance. (b) Input reactance.

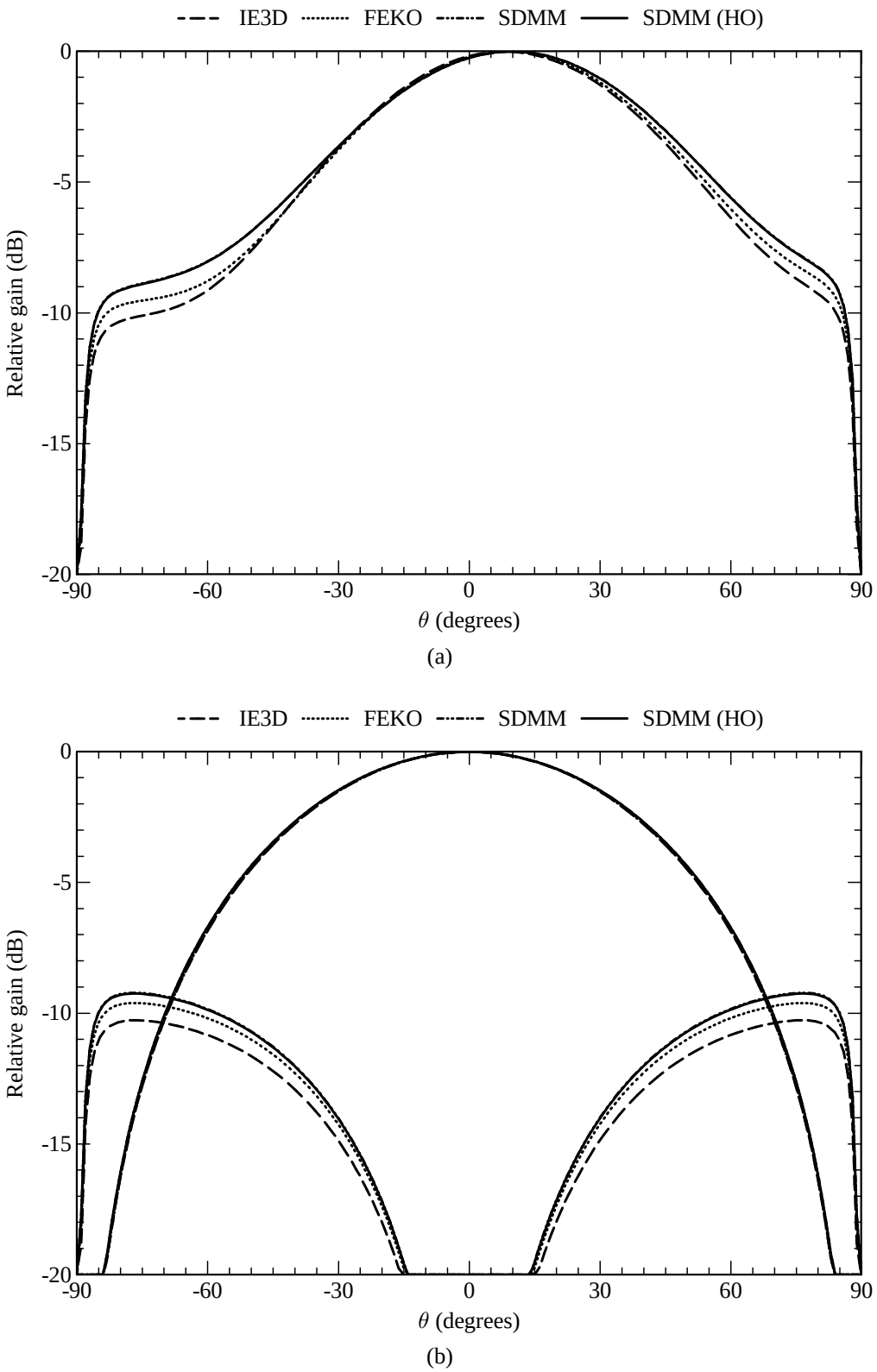


**Figure 4.19** Radiation patterns (at 1.8 GHz) of the antenna element with a circular capacitor patch. Parameters: $b$ = 4.5 mm and $d$ = 4 mm. (a) Radiation pattern in the $E$-plane ($\phi = 0^\circ$). (b) Radiation pattern in the $H$-plane ($\phi = 90^\circ$).

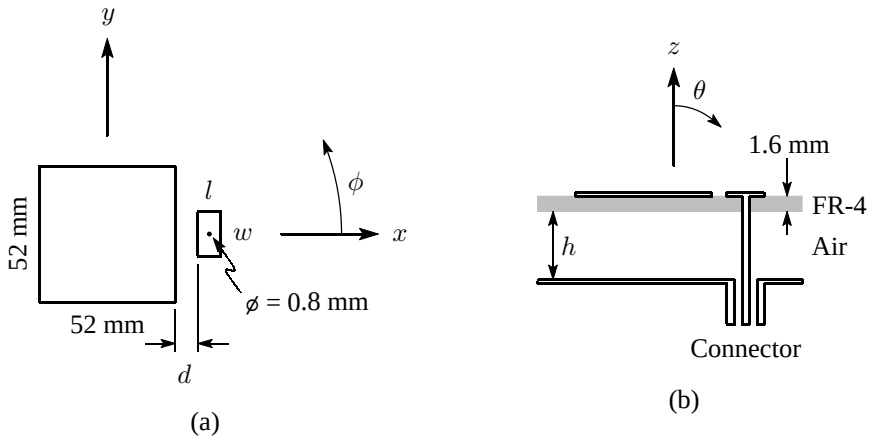


**Figure 4.20** Geometry of the antenna element with a rectangular capacitor patch. (a) Top view of the antenna element. (b) Side view of the multilayered substrate with $\varepsilon_r = 4.25$ and $\tan\delta_\varepsilon = 0.02$ for the FR-4 layer and with $\varepsilon_r = 1$ and $\tan\delta_\varepsilon = 0$ for the air layer.

been shown. On the other hand, it can be seen that the cross-polarised pattern in the *H*-plane is somewhat higher, especially towards the horizon (i.e. as $\theta$ approaches $\pm 90^\circ$). This behaviour is due to the symmetry in one plane of the structure, but the asymmetry in the orthogonal plane.

Now, consider the patch antenna element with a rectangular capacitor patch, as shown in Figure 4.20. The electric current density on the structure was modelled with eleven entire-domain sinusoidal basis functions on the resonant patch, the circular attachment mode, and twenty-two subdomain rooftop basis functions on the capacitor patch. Four PWS basis functions were used on the probe (excluding the one associated with the attachment mode). For the entire-domain sinusoidal basis functions, the (1,0), (1,2), (2,0), (2,2), (3,0), (3,2), (5,0), (7,0) and (9,0) modes were used for the $x$-directed current, while the (2,0) and (2,1) modes were used for the $y$-directed current. A radius of 2.5 mm was used for the attachment mode. Figure 4.21 shows the simulated and measured gain of the antenna element, from which it can be seen that the agreement between the three codes and the measurements, is very good. Here too, there is practically no difference in the results obtained with the two circular attachment modes. Figure 4.22 shows the simulated and measured input impedance of the antenna element, from which it can also be seen that the agreement between the three codes and the measurements, is fairly good. The input reactance as simulated by the SDMM implementation, seems to be slightly lower when compared to the rest. Also, as compared to the antenna element with the circular capacitor patch, there is not so much difference between the results obtained with the two circular attachment modes. Figure 4.23 shows the simulated radiation patterns in the *E*-plane and the *H*-plane of the antenna element. From these it can be seen that, once again, the agreement between the three codes is fairly good and that there is also practically no difference in the results obtained with the two circular attachment modes. The cross-polarised pattern in the *H*-plane shows some spread between the results of the three codes. However, the SDMM results lie in between those of the other two codes. Also,

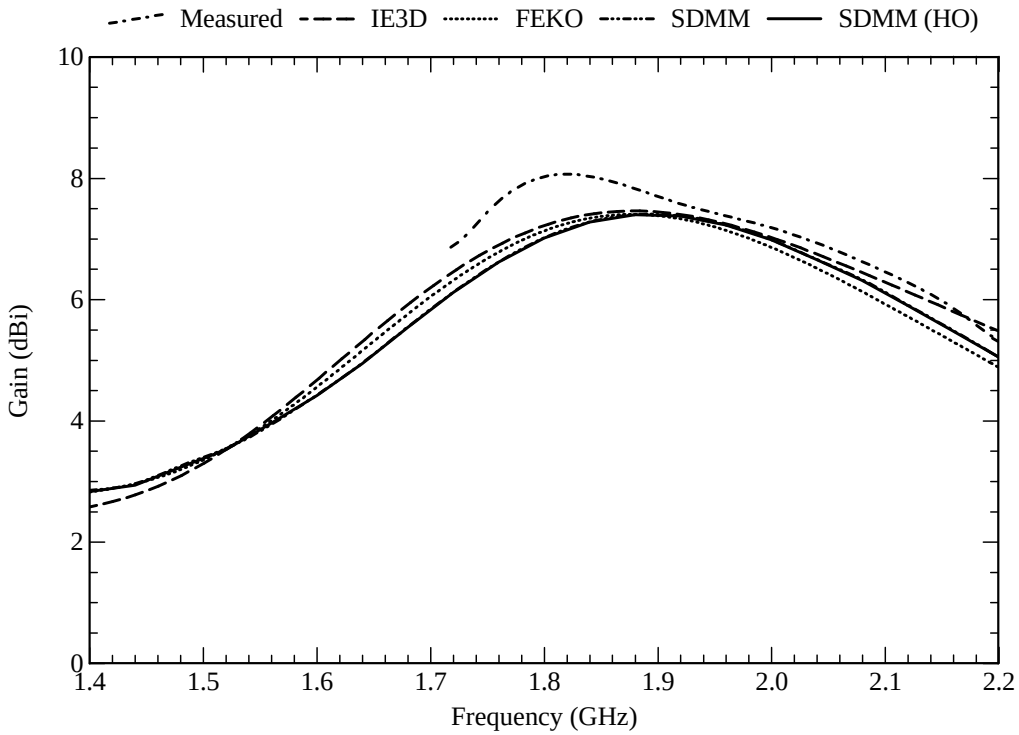


**Figure 4.21** Gain of the antenna element with a rectangular capacitor patch. Parameters: $l$ = 5 mm, $w$ = 10 mm and $d$ = 8 mm.

the cross-polarised pattern of this antenna element appears to be slightly higher than the one for the element with the circular capacitor patch.

Following from all of the results that have been presented in this section, it can be concluded that the SDMM implementation compares very well with measurements and also with the two commercial codes. In the next section, it will now be used to characterise antenna elements with capacitive feed probes. The higher-order circular attachment mode will be used henceforth, as it appears to provide results that agree well with those of the two commercial codes and the measurements when considering all the configurations that were used for the validation.

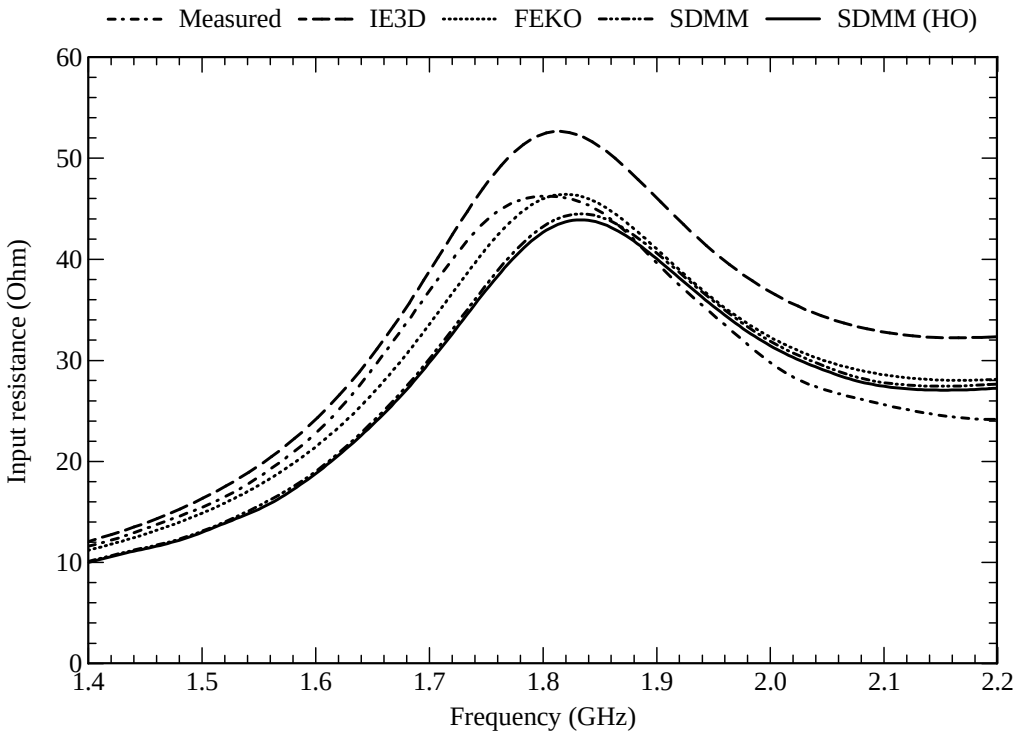


(a)

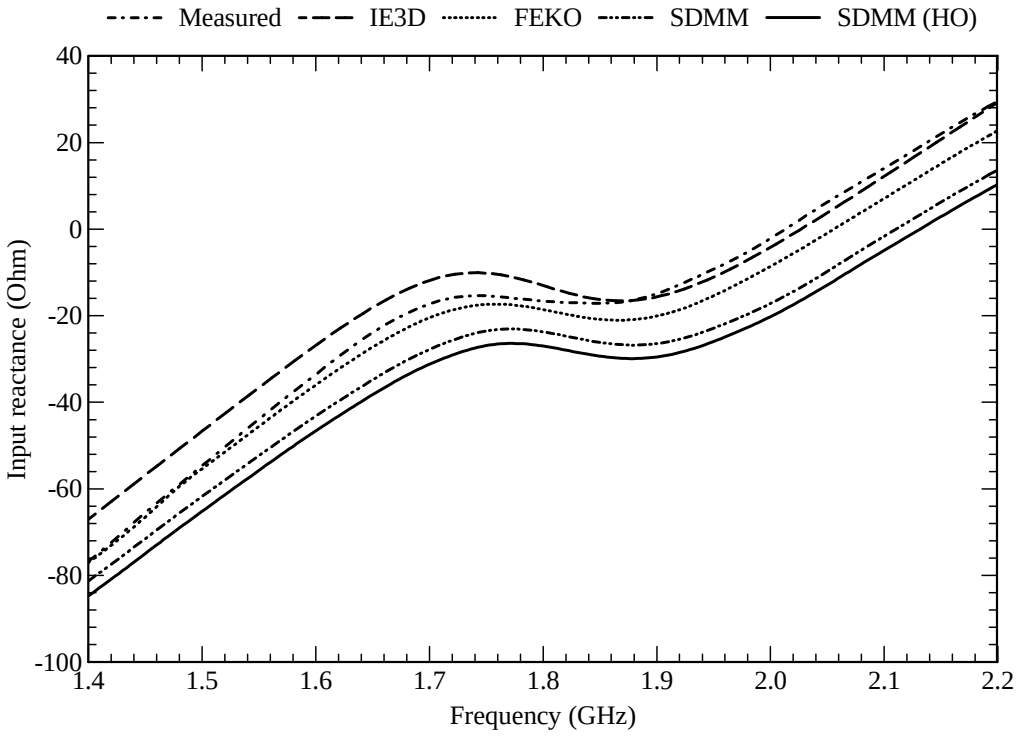


(b)

**Figure 4.22** Input impedance of the antenna element with a rectangular capacitor patch. Parameters: $l$ = 5 mm, $w$ = 10 mm and $d$ = 8 mm. (a) Input resistance. (b) Input reactance.

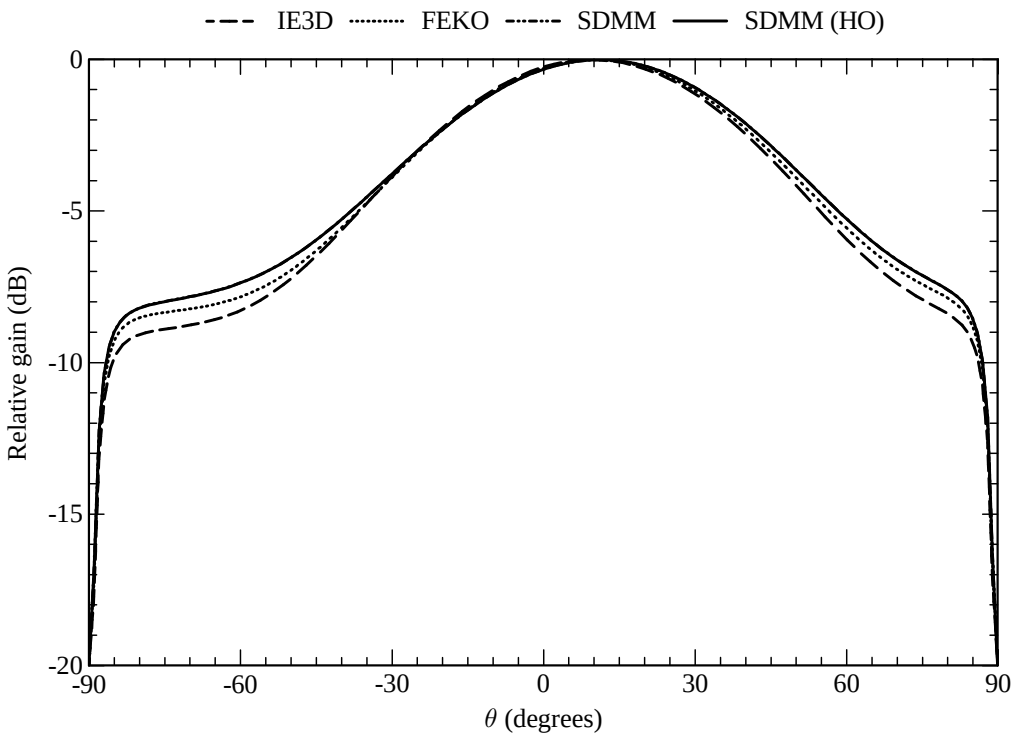


(a)

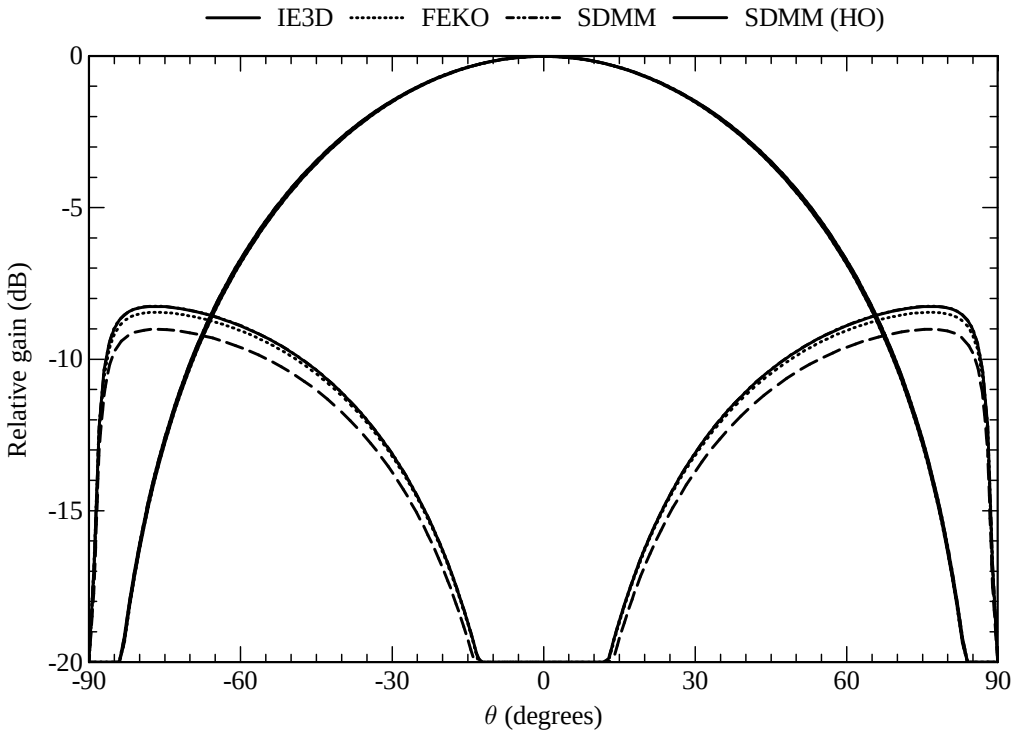


(b)

**Figure 4.23** Radiation patterns (at 1.8 GHz) of the antenna element with a rectangular capacitor patch. Parameters: $l$ = 5 mm, $w$ = 10 mm and $d$ = 8 mm. (a) Radiation pattern in the *E*-plane ($\phi = 0^\circ$). (b) Radiation pattern in the *H*-plane ($\phi = 90^\circ$).

## 4.3 CHARACTERISATION OF ANTENNA ELEMENTS WITH CAPACITIVE FEED PROBES

For both the antenna element with the circular capacitor patch, as shown in Figure 4.14, and the one with the rectangular capacitor patch, as shown in Figure 4.20, there are some key geometrical parameters that can be used to control the antenna's input impedance and bandwidth. In both cases, the size of the capacitor patch, as well as the gap-width between the resonant patch and the capacitor patch, mainly determines the input impedance of the antenna element. The bandwidth of the antenna element is mainly determined by the thickness of the substrate. The effect of these parameters will now be addressed in more detail.

### 4.3.1 Input Impedance of the Antenna Element

Consider the antenna element with the circular capacitor patch, as shown in Figure 4.14. The radius of the capacitor patch is denoted by $b$, while the gap width between the resonant patch and the capacitor patch is denoted by $d$. Figure 4.24(a) shows the effect of the gap width on the antenna input impedance, while Figure 4.24(b) shows the effect of the radius of the capacitor patch on the antenna's input impedance. The same basis functions as in Section 4.2.4 were used for the analysis. From the results it can be seen that the gap width affects both the input resistance and the input reactance, but that its effect on the input resistance is more significant than on the input reactance. Both the input resistance and input reactance decrease as the gap is widened. Furthermore, it can be seen that the radius of the capacitor patch mainly affects the input reactance, while it has hardly any effect on the input resistance. The input reactance becomes more inductive as the radius (and therefore the size) of the capacitor patch is increased.

Now, consider the antenna element with the rectangular capacitor patch, as shown in Figure 4.20. The length of the capacitor patch is denoted by $l$ and its width by $w$, while the gap width between the resonant patch and the capacitor patch is denoted by $d$. Figure 4.25(a) shows the effect of the gap width on the antenna's input impedance, Figure 4.25(b) shows the effect of the length of the capacitor patch on the antenna's input impedance, while Figure 4.25(c) shows the effect of the width of the capacitor patch on the antenna's input impedance. Once again, the same basis functions as in Section 4.2.4 were used for the analysis. From the results it can be seen that the gap width once again affects both the input resistance and the input reactance, but that its effect on the input resistance is more significant than on the input reactance. Both the input resistance and input reactance decrease as the gap is widened. Both the length and the width of the capacitor patch mainly affects the input reactance, while they only have a very small effect on the input resistance. The input reactance becomes more inductive as the dimensions (and therefore the size) of the capacitor patch are increased.

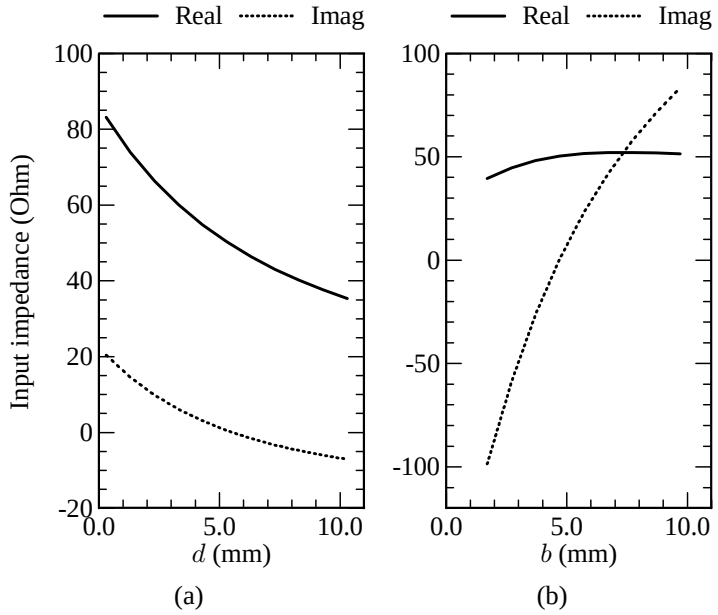


**Figure 4.24** Effect (at 1.8 GHz) of some geometrical parameters on the input impedance of the antenna element with the circular capacitor patch. (a) Gap width between rectangular resonant patch and capacitor patch (keep $b$ = 4.5 mm). (b) Radius of the capacitor patch (keep $d$ = 4 mm).

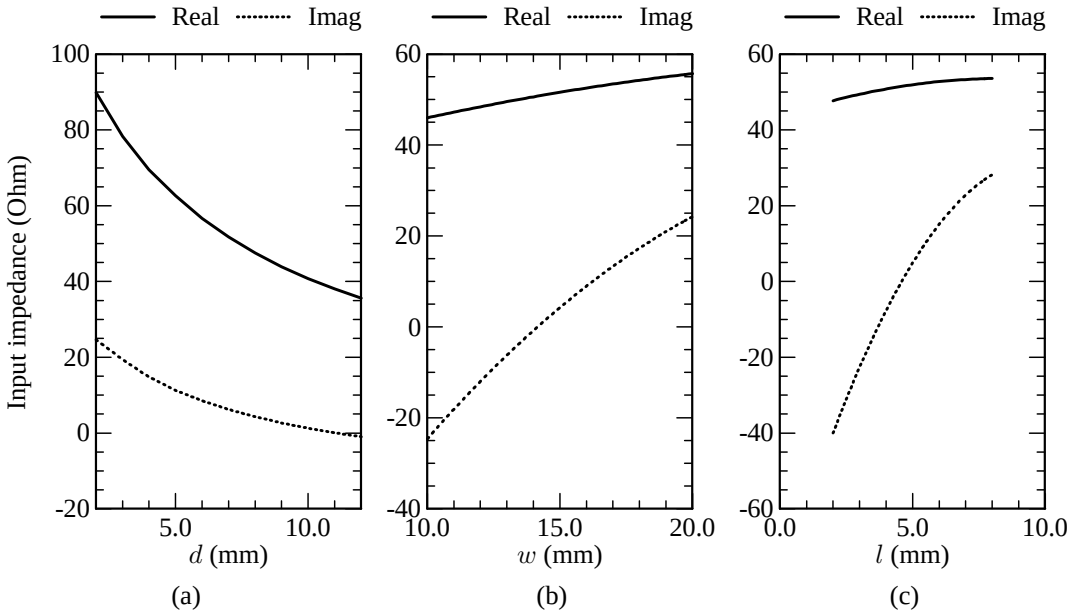


**Figure 4.25** Effect (at 1.8 GHz) of some geometrical parameters on the input impedance of the antenna element with the rectangular capacitor patch. (a) Gap width between rectangular resonant patch and capacitor patch (keep $l$ = 5 mm and $w$ = 10 mm). (b) Length of the capacitor patch (keep $d$ = 8 mm and $l$ = 5 mm). (c) Width of the capacitor patch (keep $d$ = 8 mm and $w$ = 10 mm).

### 4.3.2 Impedance Bandwidth of the Antenna Element

Figures 4.26 and 4.27 show the impedance bandwidth, at various substrate thicknesses, for the antenna elements with the circular and rectangular capacitor patches respectively. Here, the same basis functions as in Section 4.2.4 were also used for the analysis. The bandwidths that correspond to voltage standing-wave ratios (VSWRs) of 1.5:1 and 2:1, are shown. For both sets of results, the thickness of the air layer, denoted by $h$ in Figures 4.14 and 4.20, was varied from 12.5 mm to 25 mm. At every thickness of the air layer, an attempt was made to maximise the impedance bandwidth of the antenna element (i.e. to have as much as possible of the input impedance loci inside the relevant constant VSWR circles on the Smith chart).

It can be seen that the impedance bandwidth increases with increasing substrate thickness, up to a certain point where it more or less seems to taper off and decrease again. A possible explanation for this behaviour is that the coupling mechanism between the various parts of the antenna element is quite complex and also that an attempt was made to match the antenna to 50 $\Omega$ at each substrate thickness that was evaluated. For an impedance match on the thinner substrates, the capacitor patch has to be relatively large and closely spaced to the resonant patch. As the substrate thickness is increased, the capacitor patch has to become smaller and also spaced farther apart from the resonant patch. Therefore, the fact that the overall size of the structure and the spacing between the different parts change with substrate thickness, most probably explains the unusual trend (i.e. the relation between impedance bandwidth and substrate thickness does not remain linear). In this context, it is worthwhile to also refer to some results in [193], concerning probe-fed microstrip patch antennas on electrically thick substrates. In [193], the authors indeed show that the impedance bandwidth of probe-fed microstrip patch antennas increases with substrate thickness up to a certain point, after which it decreases again.

As has already been pointed out, the capacitor patch has to be bigger in size and closer to the resonant patch for the thinner air layers, while for thicker air layers, it has to be smaller in size and farther away from the resonant patch. These relationships clearly place a limit on the range of substrate thicknesses that can be used, and therefore also the achievable bandwidths that can be obtained. For example, if the substrate is too thin, the capacitor patch cannot be placed close enough to the resonant patch and would probably have to be positioned below the resonant patch. It can be seen that for these particular antenna elements and specific operating frequency, the optimum bandwidth is achieved for air layers that are between 15 mm and 20 mm thick. Figure 4.28 shows the behaviour of the impedance loci on a Smith chart for the antenna element with the circular capacitor patch. It can be seen that, for a thinner substrate thickness, the loci exhibits a rather wide loop, but that for thicker substrates, the loop becomes tighter.

From the results that have been presented in this section, it is apparent that there are a number of parameters that can be used to control the behaviour of these antenna elements. Such a knowledge, of which parameters are responsible for which behaviour, is very important, especially in an array

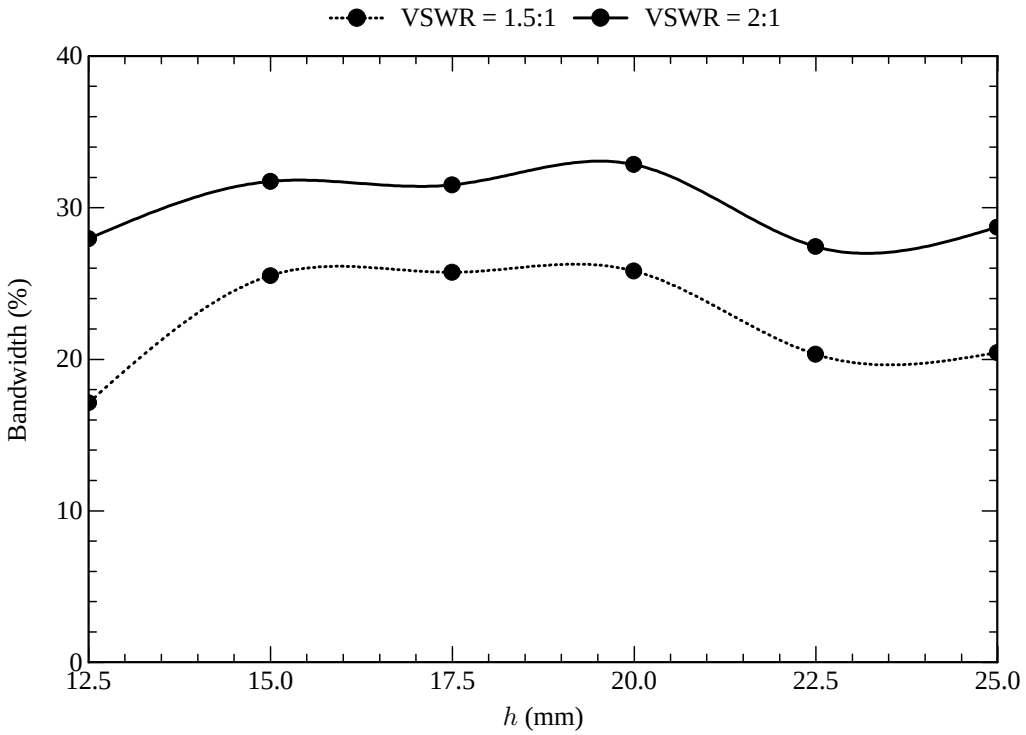


**Figure 4.26** Bandwidth (more or less around 1.8 GHz) versus substrate thickness for the antenna element with the circular capacitor patch.

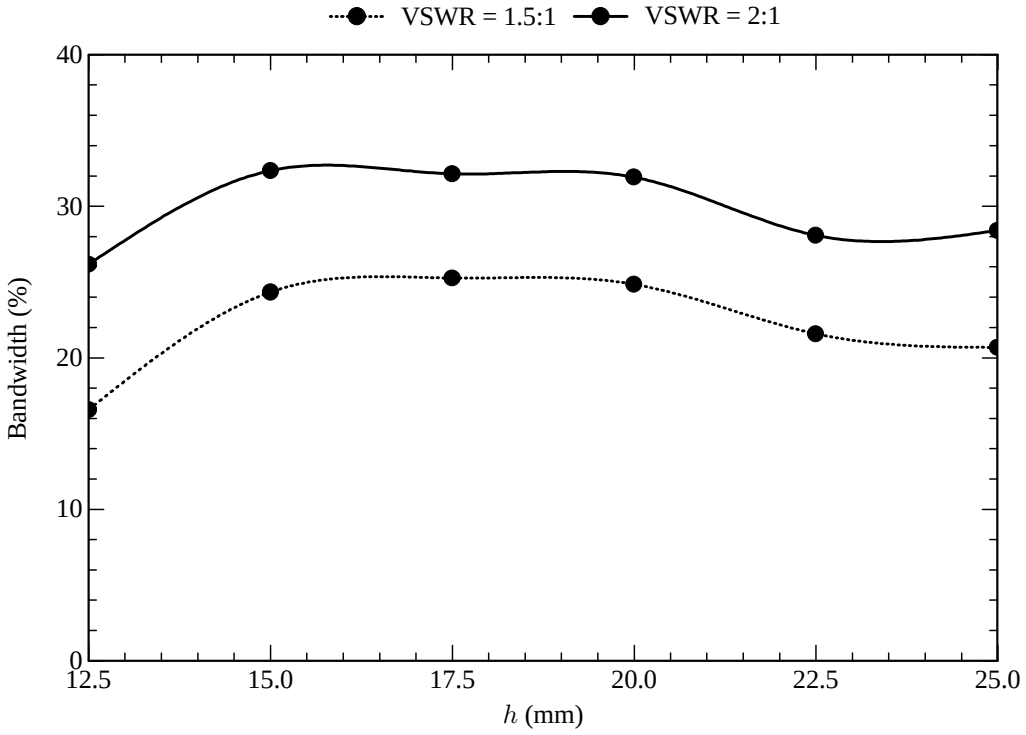


**Figure 4.27** Bandwidth (more or less around 1.8 GHz) versus substrate thickness for the antenna element with the rectangular capacitor patch.

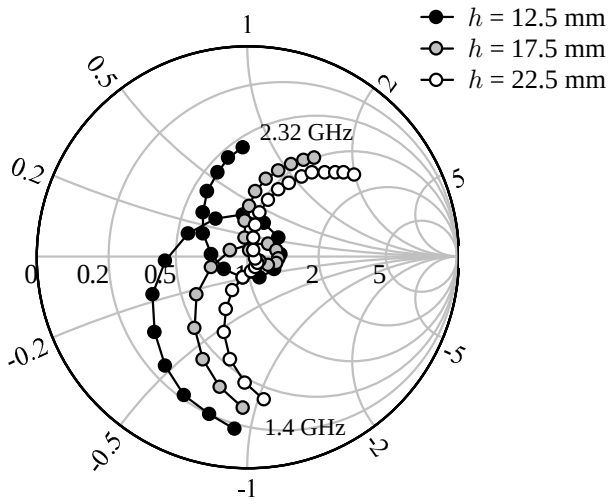


**Figure 4.28** Impedance loci (normalised to 50 Ω) of the antenna element with the circular capacitor patch.

environment where there are even more parameters that have an influence on the behaviour of each element. In the next section, it will now be shown how these antenna elements can be used in typical antenna applications.

## 4.4 APPLICATIONS

Microstrip patch antennas are very often used in array configurations where there might be specific requirements in terms of antenna gain, beamwidth and polarisation. In this section, a number of applications are addressed where patch antennas with capacitive feed probes can be very useful. In Section 4.4.1, it is first shown how the cross-polarisation levels can be reduced for a single antenna element. This is then followed by a discussion on dual-polarised elements in Section 4.4.2. The building block for some of the arrays that are investigated, consists of two elements that are positioned in a back-to-back configuration. The characteristics of such a configuration are addressed in Section 4.4.3. In Sections 4.4.4 and 4.4.5, vertically- and horizontally-polarised arrays are presented, while Sections 4.4.6, 4.4.7 and 4.4.8 are devoted to various $\pm 45^\circ$ slant-polarised arrays. Finally, in Section 4.5, it is shown how the capacitive feed can be used with resonant patches that are not rectangular in shape.

### 4.4.1 Antenna Element with Reduced Cross-Polarisation Levels

As is evident from the results in Section 4.2.4, an antenna element with a single probe-fed capacitor patch might have cross-polarisation levels in the *H*-plane that are unacceptably high for some applications. It is possible to reduce these levels by making the structure more symmetric. This can be done by adding another probe-fed capacitor patch on the opposite side of the resonant patch, as illustrated in Figure 4.29. However, it is important that the second capacitor patch gets excited exactly out of phase (i.e. a $180^\circ$ phase difference) with the first capacitor patch. The only

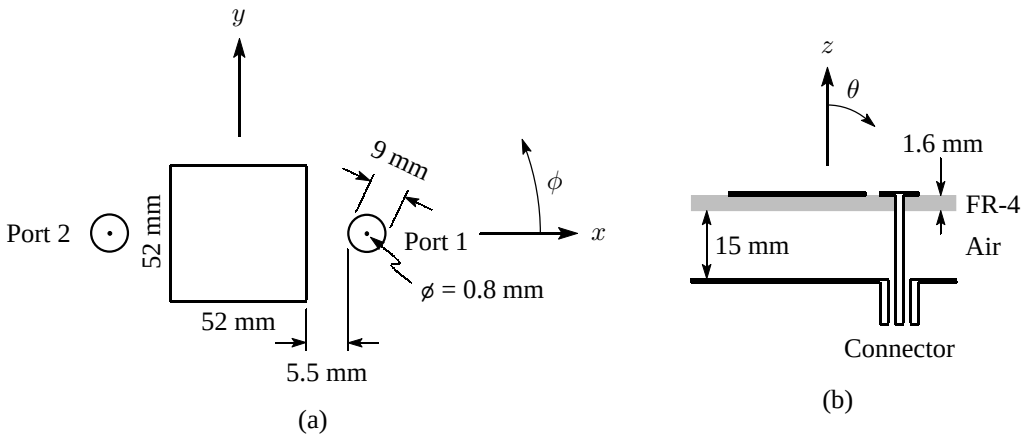


**Figure 4.29** Geometry of the antenna element with two capacitor patches for reduced cross-polarisation levels. (a) Top view of the antenna element. (b) Side view of the multilayered substrate with $\varepsilon_r = 4.25$ and $\tan\delta_\varepsilon = 0.02$ for the FR-4 layer and with $\varepsilon_r = 1$ and $\tan\delta_\varepsilon = 0$ for the air layer.

drawback of such an element is that it requires some sort of feed network below the ground plane in order to split the signal and to provide the phase shift. However, this is usually not a problem in an antenna array, as it requires a feed network anyway.

Due to the fact that the antenna element is driven by two ports, the input impedance at a specific port is a function of the self-impedance at that port as well as the mutual impedance between the two ports. It is possible to express the input impedance at any of the ports by making use of the $Z$-parameters associated with the two ports. The $Z$-parameters relate the port voltages to the port currents through

$$\begin{Bmatrix} V_1 \\ V_2 \end{Bmatrix} = \begin{bmatrix} Z^P_{1,1} & Z^P_{1,2} \\ Z^P_{2,1} & Z^P_{2,2} \end{bmatrix} \cdot \begin{Bmatrix} I_1 \\ I_2 \end{Bmatrix}, \tag{4.2}$$

where $V_1$ and $V_2$ are the voltages at ports 1 and 2 respectively, and $I_1$ and $I_2$ are the currents at these ports. The voltage at port 1 can therefore be expressed as

$$V_1 = Z^P_{1,1} I_1 + Z^P_{1,2} I_2. \tag{4.3}$$

From (4.3), it then follows that the input impedance at port 1, $Z^{\text{in}}_1$, can be expressed as

$$\begin{aligned} Z^{\text{in}}_1 &= \frac{V_1}{I_1} \\ &= Z^P_{1,1} + Z^P_{1,2}\left(\frac{I_2}{I_1}\right). \end{aligned} \tag{4.4}$$

Now, due to the 180° phase difference between $I_1$ and $I_2$, $I_2 = -I_1$. The input impedance at port 1 then reduces to

$$Z^{\text{in}}_1 = Z^P_{1,1} - Z^P_{1,2}. \tag{4.5}$$

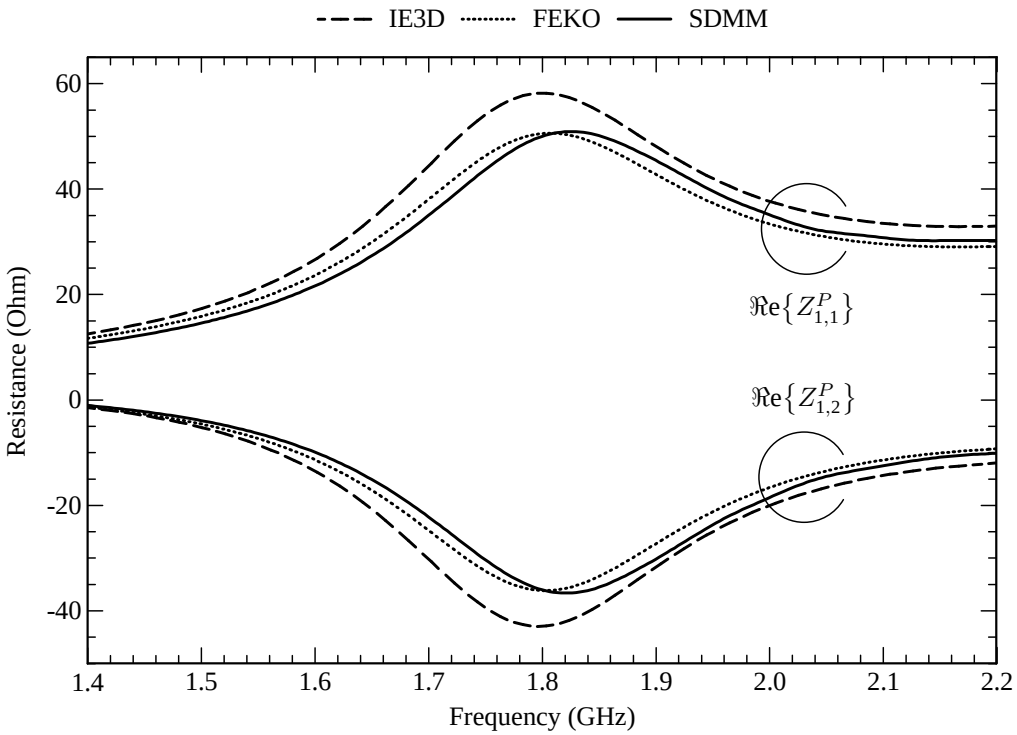


(a)

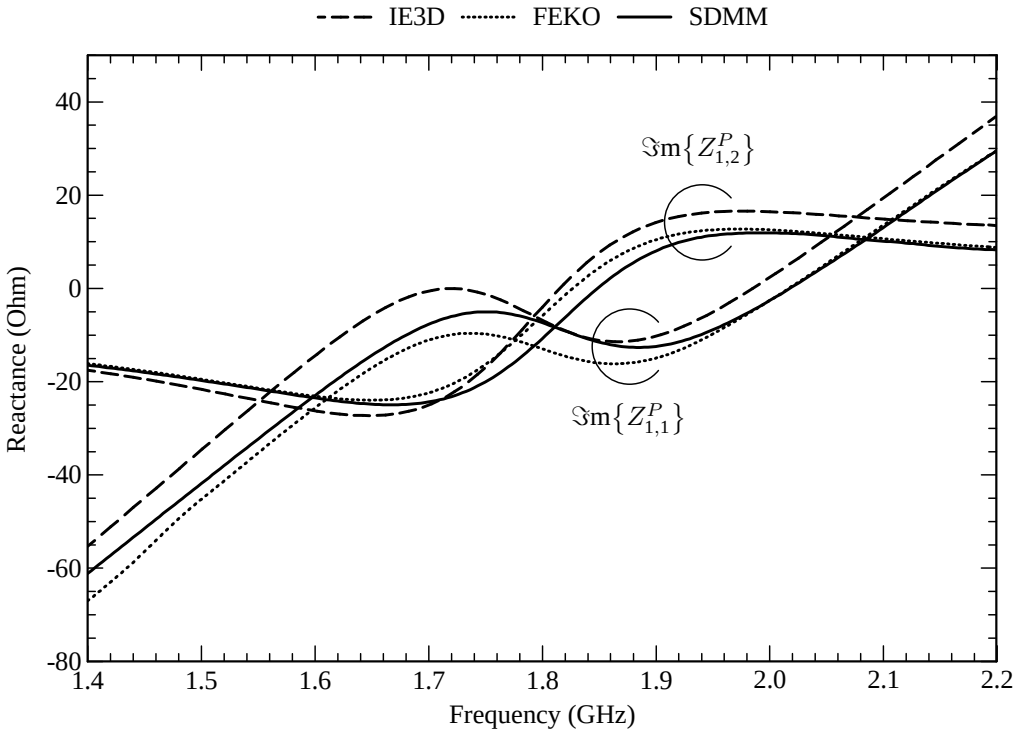


(b)

**Figure 4.30** *Z*-parameters of the two ports of the antenna element with two capacitor patches for reduced cross-polarisation levels. (a) Resistive part of the *Z*-parameters. (b) Reactive part of the *Z*-parameters.

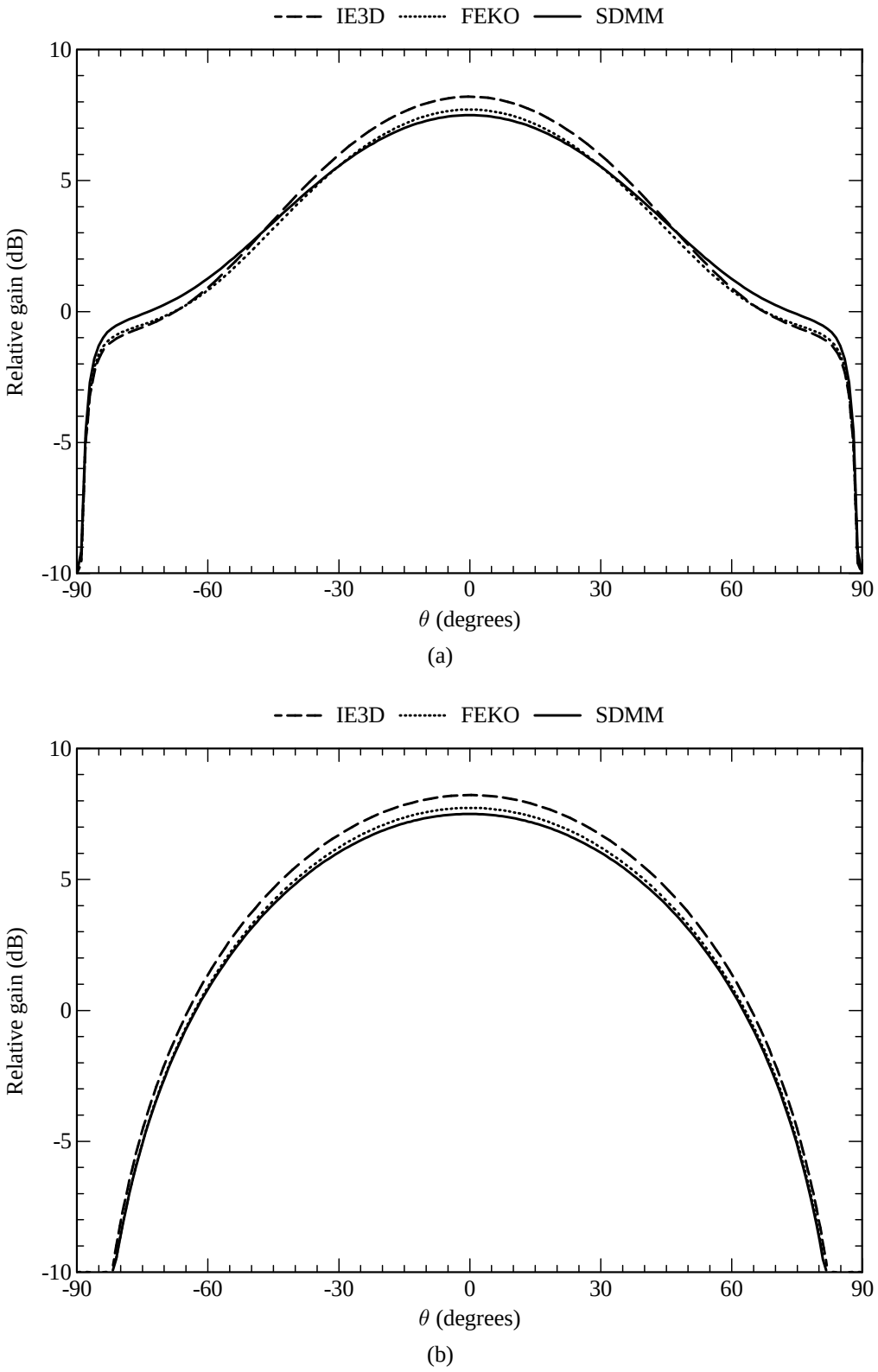


**Figure 4.31** Radiation patterns (at 1.8 GHz) of the antenna element with two capacitor patches for reduced cross-polarisation levels. (a) Radiation pattern in the $E$-plane ($\phi = 0^\circ$). (b) Radiation pattern in the $H$-plane ($\phi = 90^\circ$).

If one now wants to set the input impedance at port 1 equal to $Z_0$, it implies that

$$\Re\mathrm{e}\{Z^P_{1,1}\} - \Re\mathrm{e}\{Z^P_{1,2}\} = Z_0 \tag{4.6}$$

and that

$$\Im\mathrm{m}\{Z^P_{1,1}\} = \Im\mathrm{m}\{Z^P_{1,2}\}. \tag{4.7}$$

Of course, the expression for the input impedance at port 2 follows in a similar way. For a $Z_0$ input impedance at port 2,

$$\Re\mathrm{e}\{Z^P_{2,2}\} - \Re\mathrm{e}\{Z^P_{2,1}\} = Z_0 \tag{4.8}$$

and

$$\Im\mathrm{m}\{Z^P_{2,2}\} = \Im\mathrm{m}\{Z^P_{2,1}\} \tag{4.9}$$

have to be satisfied. The antenna element can be designed through an iterative process. As in Section 4.3, the size of the capacitor patches, as well as the separation distance between each capacitor patch and the resonant patch, can be used to control $Z^P_{1,1}$ and $Z^P_{2,2}$. For specific values of $Z^P_{1,2}$ and $Z^P_{2,1}$, which should be equal by the way, $Z^P_{1,1}$ and $Z^P_{2,2}$ can then be changed until (4.6) to (4.9) are satisfied.

Figure 4.30 shows the simulated *Z*-parameters of the antenna element in Figure 4.29. This element was designed for an input impedance of 100 Ω at each port. As stated before, the element will usually be implemented with a power splitter below the ground plane, which can then transform the overall input impedance down to 50 Ω. From the results it can be seen that the agreement between all three codes is quite good. Figure 4.31 shows the simulated radiation patterns in the *E*-plane and the *H*-plane of the antenna element. The cross-polar levels in the *H*-plane have now effectively been reduced to levels that fall well below the range of the graph. Once again, the three codes show good agreement. The same basis functions as in Section 4.2.4 were used for the SDMM analysis.

### 4.4.2 Dual-Polarised Antenna Element

In many applications, it is necessary to have antenna elements with two orthogonal polarisations. This can be achieved with the antenna element depicted in Figure 4.32. Here, one port is used to generate the one polarisation, while the other port is used to generate the orthogonal polarisation. The electric current density on the resonant patch will primarily be directed along the $x$ direction for port 1, while that for port 2, will primarily be directed along the $y$ direction.

The dimensions of the dual-polarised element of Figure 4.32 are similar to those of the single-polarised element of Section 4.2.4. The electric current density on the structure was modelled with eighteen entire-domain sinusoidal basis functions on the resonant patch, the single higher-order circular attachment mode on each capacitor patch, and four PWS basis functions on each probe (excluding the one associated with the attachment mode). For the entire-domain sinusoidal

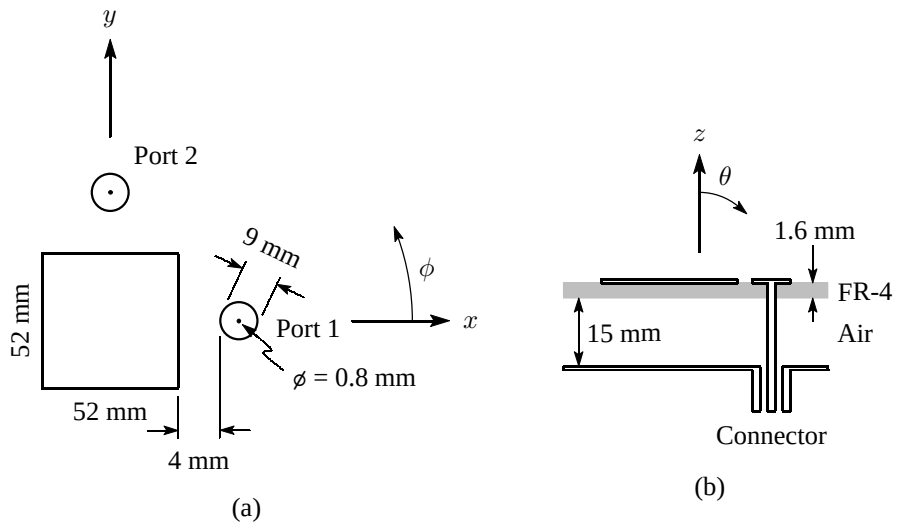


**Figure 4.32** Geometry of the dual-polarised antenna element. (a) Top view of the antenna element. (b) Side view of the multilayered substrate with $\varepsilon_r = 4.25$ and $\tan\delta_\varepsilon = 0.02$ for the FR-4 layer and with $\varepsilon_r = 1$ and $\tan\delta_\varepsilon = 0$ for the air layer.

basis functions, the (1,0), (1,2), (2,0), (2,1), (3,0), (3,2), (5,0), (7,0) and (9,0) modes were used for the $x$-directed current, while the same set of modes were also used for the $y$-directed current.

Figure 4.33(a) shows the simulated and measured reflection coefficient at port 1 of the antenna element, while Figure 4.33(b) shows the simulated and measured coupling between the two ports of the antenna element. From these it can be seen that the element remains well matched over a wide bandwidth, although a second port was introduced (note that the dimensions of the capacitor patches, as well as the distance between each capacitor patch and the resonant patch, were kept equal to those of Section 4.2.4 for the single-polarised antenna element). It can also be seen that the coupling between the two ports vary between approximately $-15$ dB and $-20$ dB over the operating frequency band. In both cases, the agreement between the measurements and the simulations, is quite good. In this case, the results of FEKO, as well as those of the SDMM, seems to compare slightly better to the measurements than the results of IE3D do.

For some applications, the coupling between the two ports of the dual-polarised antenna element might be too high. This can be improved by using symmetric feeds, similar to those in Section 4.4.1. It might, however, require a more complex feed network. In some of the following sections, it will also be shown how various array configurations can be used to realise dual-polarised antennas with less coupling between the two ports.

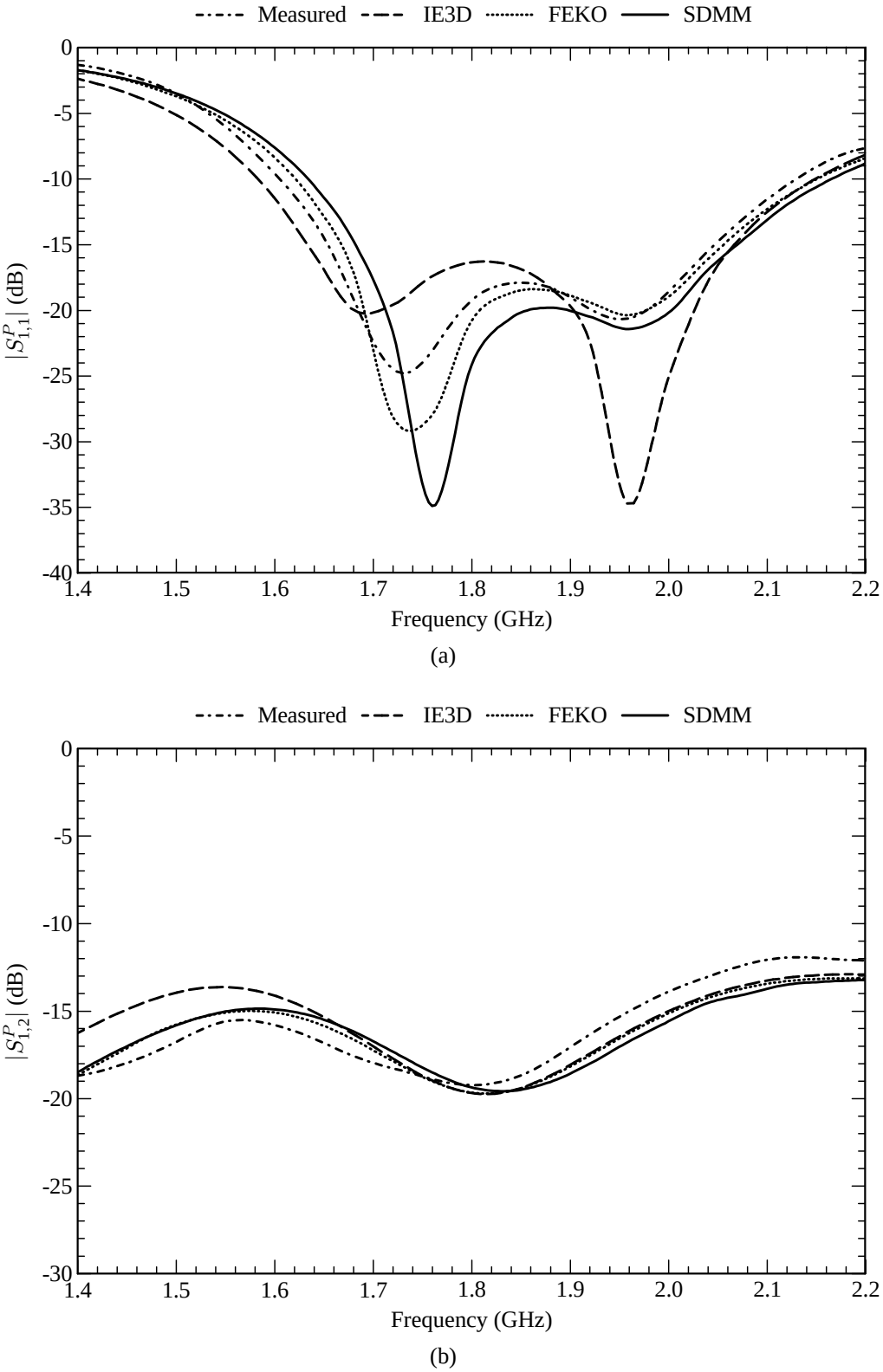


**Figure 4.33** *S*-parameters of the dual-polarised antenna element. (a) Reflection coefficient at port 1. (b) Coupling between the two ports.

### 4.4.3 Two-Element Linearly-Polarised Array

An alternative way to reduce the cross-polarisation levels of a probe-fed patch antenna, is to use two elements that are positioned in a back-to-back configuration, as shown in Figure 4.34. Here, as is the case in Section 4.4.1, the two ports have to be excited exactly out of phase (i.e. a 180° phase difference). The resulting effect is that the co-polarised currents on the two resonant patches are aligned, but that the fields radiated by the cross-polarised currents, cancel out.

The two-element array has to be excited by a feed network, similar to the one in Section 4.4.1, and therefore the input impedance at each port is a function of the self-impedance at that port as well as the mutual impedance between the two ports. In order to design such a two-element array, it is important to know how the separation distance between the two elements affects both the self-impedance at each port and the mutual impedances between the two ports. Figure 4.35(a) shows how the self-impedance at port 1, $Z^P_{1,1}$, varies with the separation distance, $s$, between the two patches, while Figure 4.35(b) shows how the mutual impedance, $Z^P_{1,2}$, varies with the separation distance. Both these have been simulated with the SDMM. It can be seen that separation distance has a more profound effect on the mutual impedance between the two ports, than on the self-impedance at each port. Once again, the antenna element can be designed through an iterative process. As in Section 4.3, the size of the capacitor patches, as well as the separation distance between them and the resonant patches, can be used to control $Z^P_{1,1}$ and $Z^P_{2,2}$. For specific values of $Z^P_{1,2}$ and $Z^P_{2,1}$, which should be equal, $Z^P_{1,1}$ and $Z^P_{2,2}$ can then be changed until (4.6) to (4.9) are satisfied.

Figure 4.36 shows the simulated $Z$-parameters of the two-element antenna array in Figure 4.34, which was designed for an input impedance of 50 Ω at each port (this corresponds to a separation distance, $s$, of 30 mm). From the results it can be seen that the agreement between the measurements and all three codes, is quite good. Figure 4.37 shows the simulated radiation patterns in the $E$-plane and the $H$-plane of the two-element antenna array. The cross-polar levels in both planes fall well below the range of the graph. Once again, the three codes show good agreement. It can be seen that the beamwidth in the $E$-plane is narrowed due to the alignment of the two elements. The electric current density on the structure was modelled with eleven entire-domain sinusoidal basis functions on each resonant patch, the single higher-order circular attachment mode on each capacitor patch, and four PWS basis functions on each probe (excluding the one associated with the attachment mode). For the entire-domain sinusoidal basis functions, the (1,0), (1,2), (2,0), (2,2), (3,0), (3,2), (5,0), (7,0) and (9,0) modes were used for the $x$-directed current, while the (2,0) and (2,1) modes were used for the $y$-directed current.

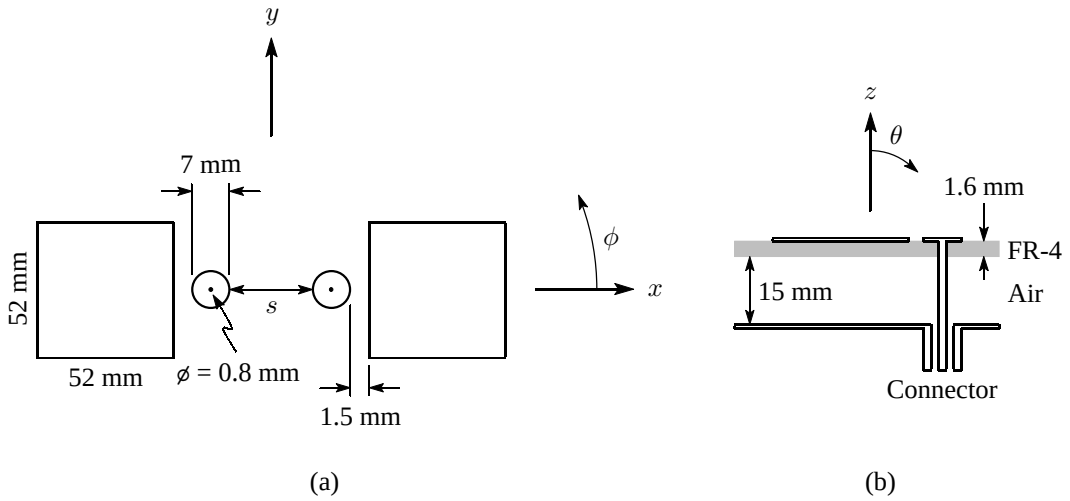


**Figure 4.34** Geometry of the two-element linearly-polarised array. (a) Top view of the array. (b) Side view of the multilayered substrate with $\varepsilon_r = 4.25$ and $\tan\delta_\varepsilon = 0.02$ for the FR-4 layers and with $\varepsilon_r = 1$ and $\tan\delta_\varepsilon = 0$ for the air layer.

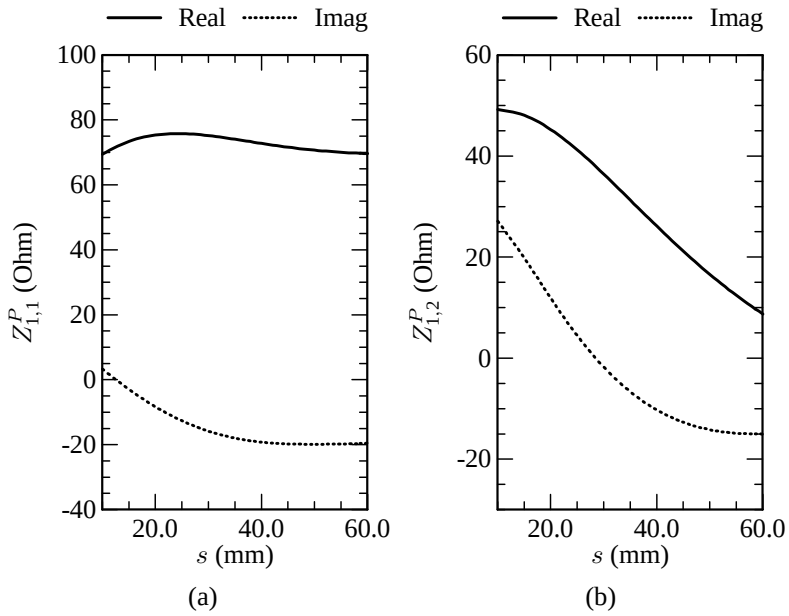


**Figure 4.35** Effect (at 1.8 GHz) of the separation distance on the *Z*-parameters of the two-element linearly-polarised array. (a) Self-impedance at port 1. (b) Mutual impedance between the two ports.

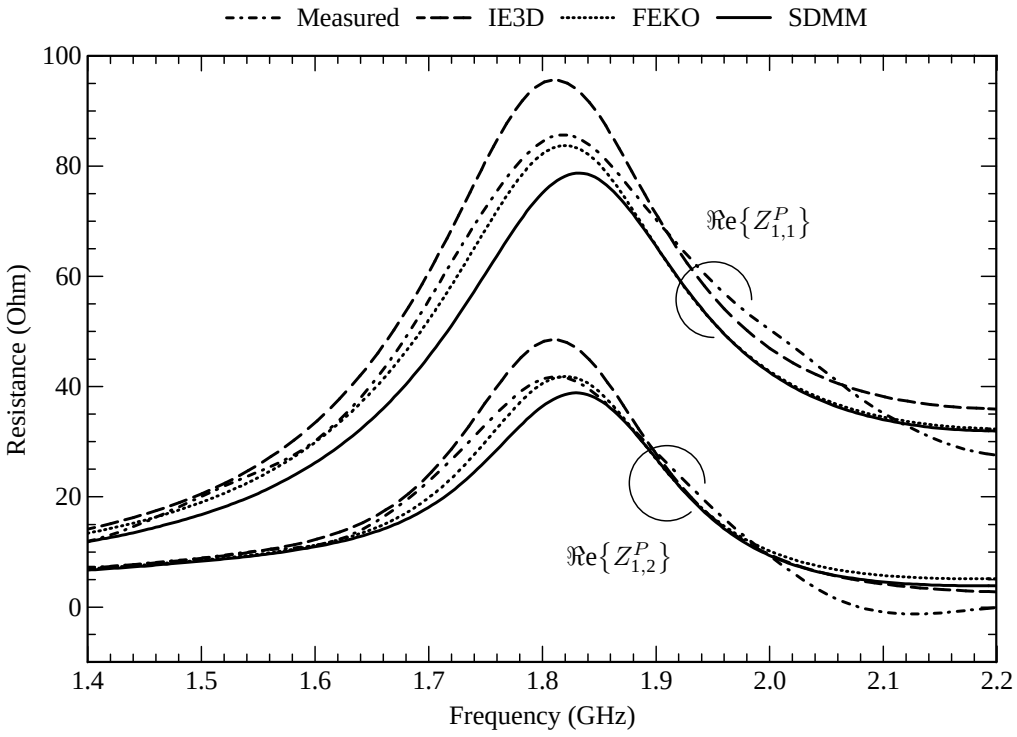


(a)

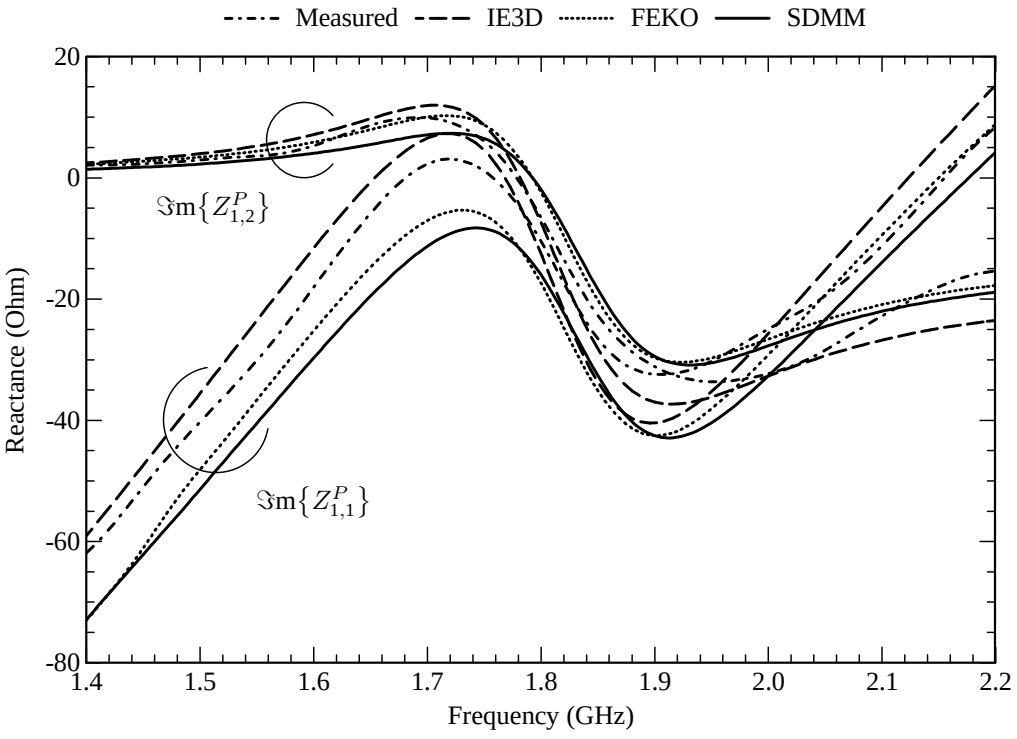


(b)

**Figure 4.36** $Z$-parameters of the two-element linearly-polarised array ($s$ = 30 mm). (a) Resistive part of the $Z$-parameters. (b) Reactive part of the $Z$-parameters.

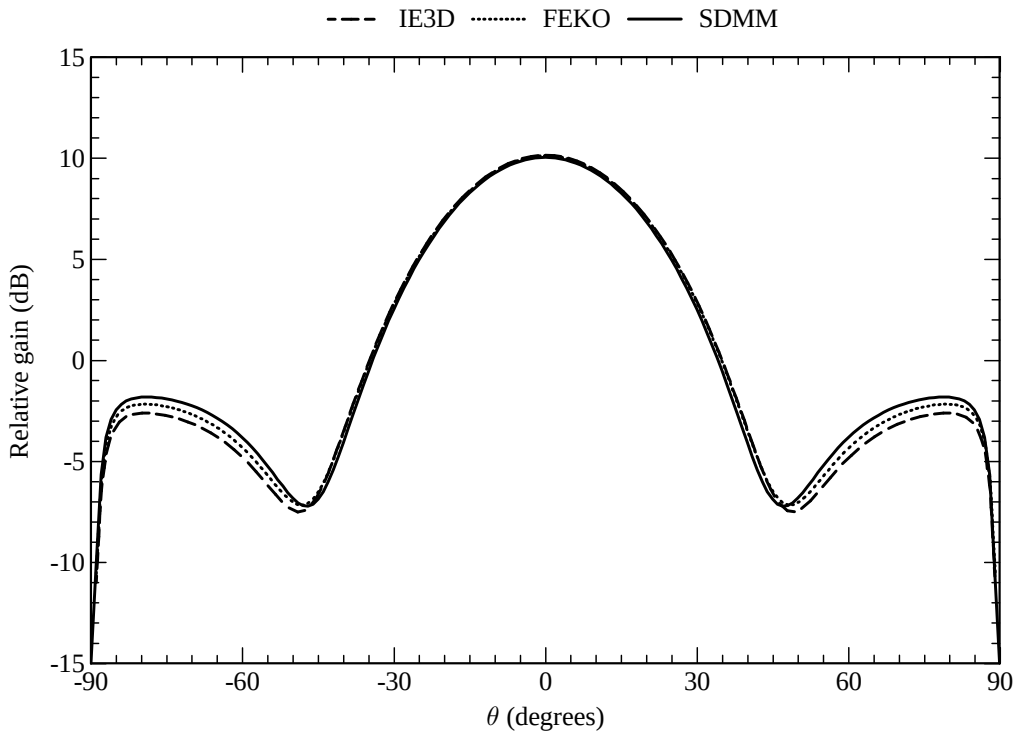


(a)

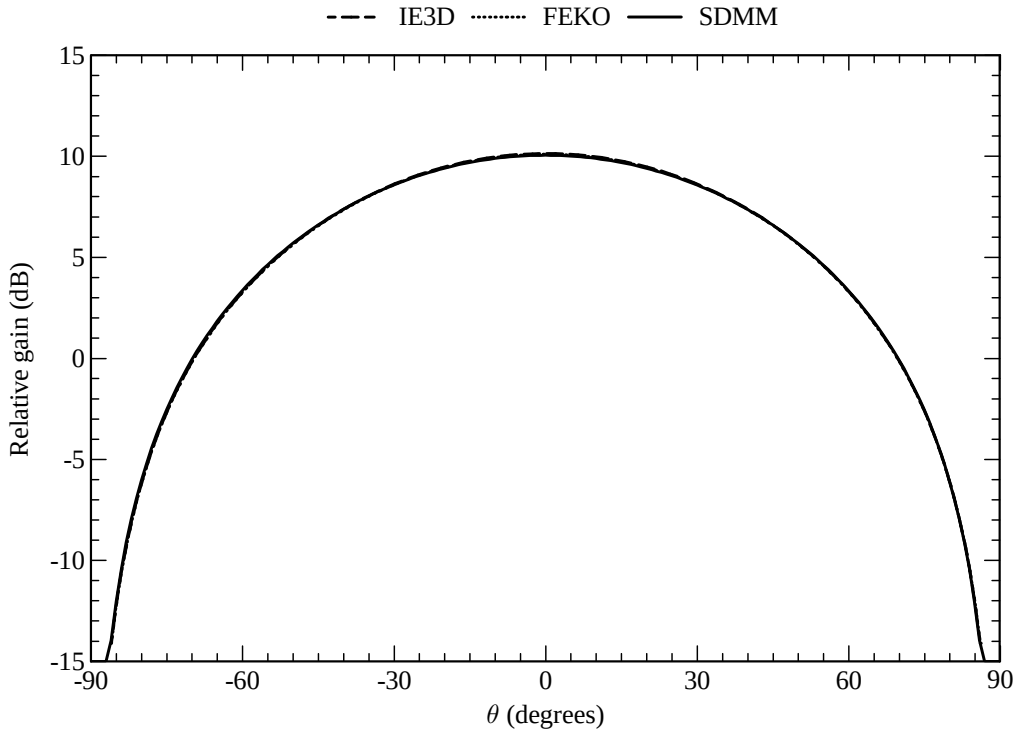


(b)

**Figure 4.37** Radiation patterns (at 1.8 GHz) of the two-element linearly-polarised array ($s$ = 30 mm). (a) Radiation pattern in the $E$-plane ($\phi = 0^\circ$). (b) Radiation pattern in the $H$-plane ($\phi = 90^\circ$).

### 4.4.4 Four-Element Vertically-Polarised Array

Many applications require the use of linear vertically-polarised antenna arrays. An example of such an array is shown in Figure 4.38. This particular one consists of a pair of two-element sub-arrays. Note that the resonant patches are all equally separated. As can be seen from Figure 4.38, two of the probes are excited exactly out of phase with respect to the other two probes. This is done to reduce cross-polarisation levels. The array was designed so that the input impedance at each port is equal to 50 $\Omega$.

The electric current density on the structure was modelled with eleven entire-domain sinusoidal basis functions on each resonant patch, the single higher-order circular attachment mode on each capacitor patch and four PWS basis functions on each probe (excluding the one associated with the attachment mode). For the entire-domain sinusoidal basis functions, the (1,0), (1,2), (2,0), (2,2), (3,0), (3,2), (5,0), (7,0) and (9,0) modes were used for the $y$-directed current, while the (2,0) and (2,1) modes were used for the $x$-directed current. The feed network was modelled with Sonnet's circuit analysis module. Table 4.1 shows how the computer-memory requirements, for the storage of the interaction matrix, varies among the three codes.[1] It can be seen that the memory requirements of the SDMM are substantially lower then that of the other two codes. Also, for the SDMM, the amount of duplicate entries in the interaction matrix equates to 67.88%.[2]

**Table 4.1**
Computer memory required for the storage of the interaction matrix associated with the four-element vertically-polarised antenna array.

| Method | Unknowns | Memory (MB) |
|---|---|---|
| IE3D | 2560 | 100.0 |
| FEKO | 2576 | 101.3 |
| SDMM | 64 | 0.063 |

Figure 4.39 shows the simulated reflection coefficient at the input port of the feed network. It can be seen that there is close agreement between the results of the FEKO and SDMM codes, but that the reflection coefficient, as simulated by IE3D, is somewhat lower. However, as shown in Table 4.2, the 10 dB return-loss bandwidths for all three codes seem to be comparable. Figure 4.40 shows the simulated radiation patterns in the *E*-plane and the *H*-plane of the antenna array. The

[1] For comparison, it is assumed that all the codes store the entire interaction matrix (i.e. $N^2$ values) in the computer's memory. This assumption is always valid for the SDMM code, while it is also valid for FEKO when the default settings are used, and for IE3D when the full matrix solver is used.

[2] The amount of duplicate entries within the interaction matrix makes no difference in the amount of matrix entries that are actually stored within the computer's memory (the entire matrix is always stored). It only gives an indication of the amount of matrix elements that are not calculated directly, but that are merely copied from other entries (i.e. the speedup in filling the matrix).

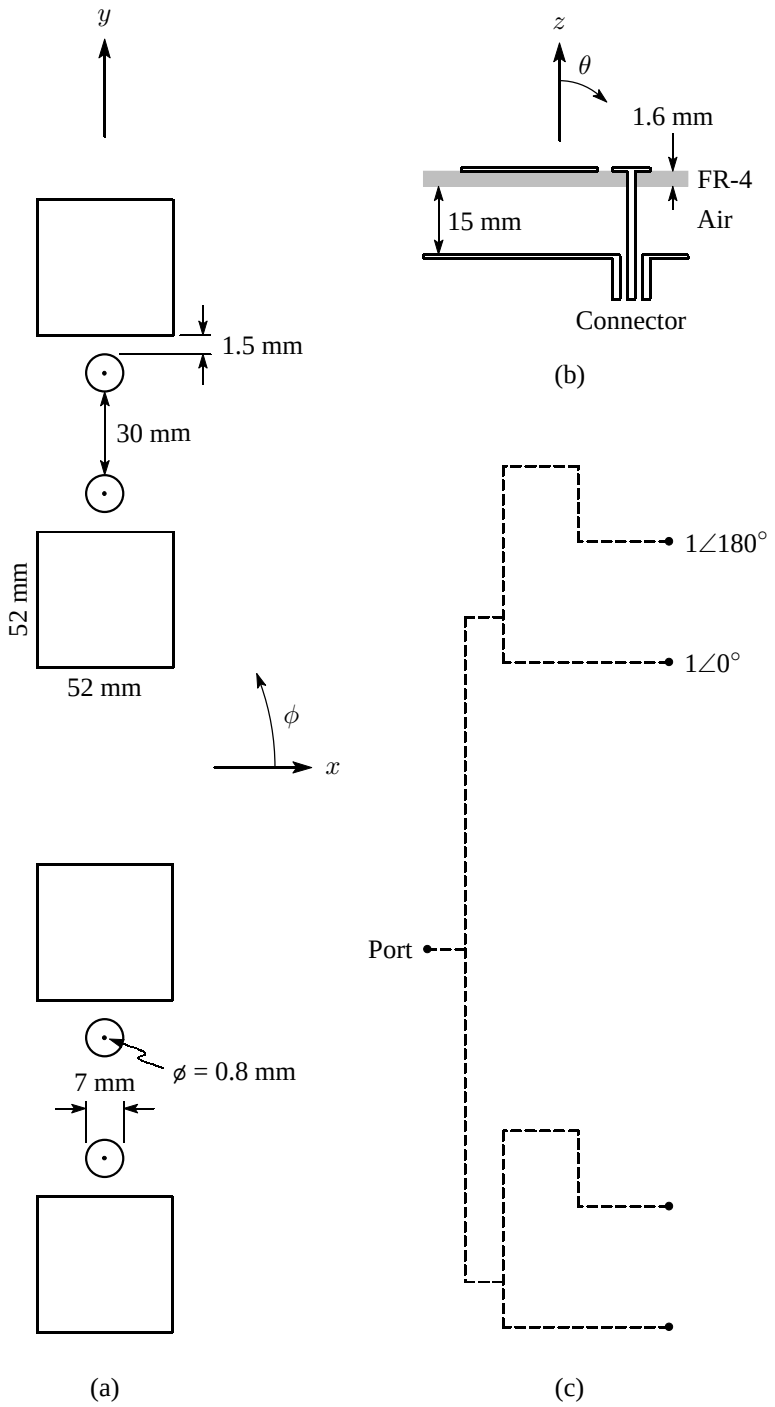


**Figure 4.38** Geometry of the four-element vertically-polarised array. (a) Top view of the array. (b) Side view of the multilayered substrate with $\varepsilon_r = 4.25$ and $\tan\delta_\varepsilon = 0.02$ for the FR-4 layers and with $\varepsilon_r = 1$ and $\tan\delta_\varepsilon = 0$ for the air layer. (c) Schematic of the feed network.

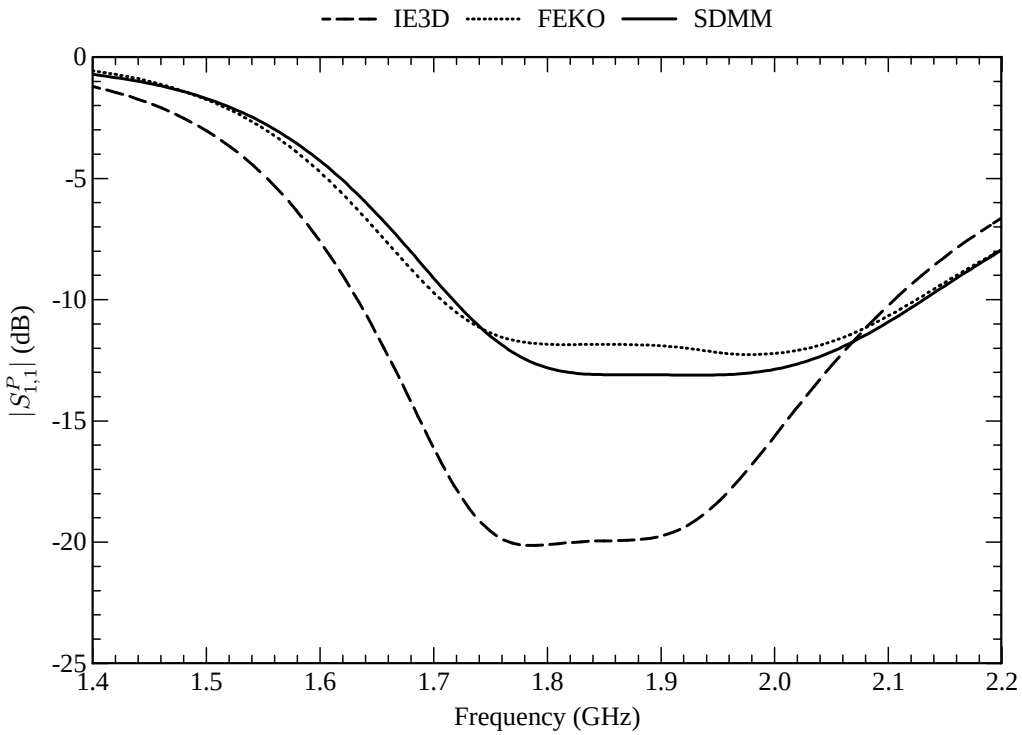


**Figure 4.39** Reflection coefficient at the input port of the feed network for the four-element vertically-polarised array.

cross-polar levels in both planes fall well below the range of the graph. In terms of the radiation patterns, the three codes show very good agreement. It can be seen that the beamwidth in the *E*-plane is narrowed due to the vertical alignment of the antenna elements.

**Table 4.2**
10 dB Return-loss bandwidth at the input port of the four-element vertically-polarised antenna array.

| Method | Bandwidth (%) |
|---|---|
| IE3D | 25.7 |
| FEKO | 21.9 |
| SDMM | 21.3 |

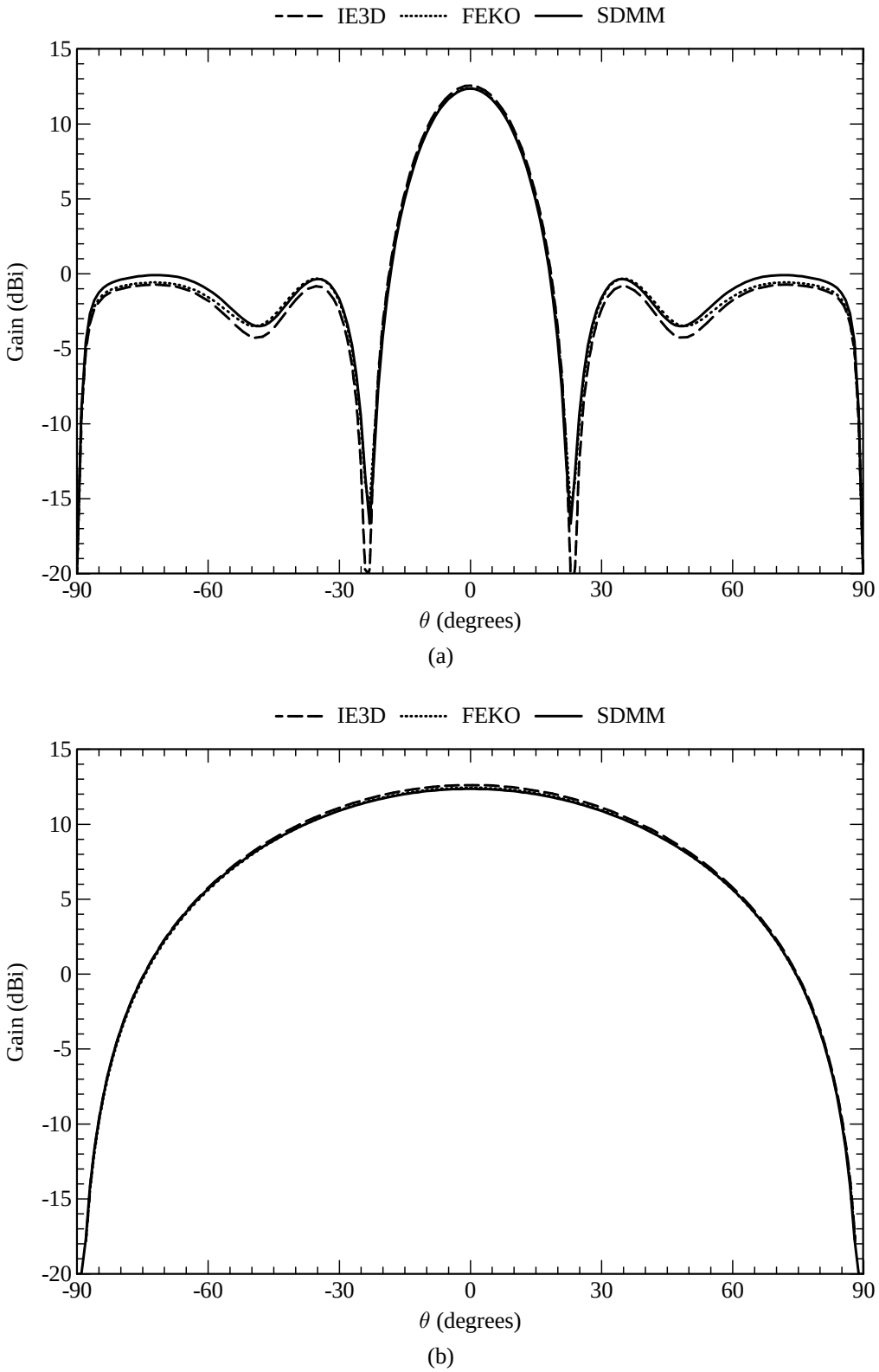


**Figure 4.40** Radiation patterns (at 1.8 GHz) of the four-element vertically-polarised array. (a) Radiation pattern in the $E$-plane ($\phi = 90°$). (b) Radiation pattern in the $H$-plane ($\phi = 0°$).

### 4.4.5 Four-Element Horizontally-Polarised Array

For some applications, a linear horizontally-polarised antenna array is more advantageous than vertically polarised ones. An example of such an array is shown in Figure 4.41. This particular one consists of four elements, each with two capacitor patches to reduce cross-polarisation levels. As can be seen from Figure 4.41, four of the probes are excited exactly out of phase with respect to the other four probes. The array was designed so that the input impedance at each port is equal to 50 $\Omega$.

The electric current density on the structure was modelled with eleven entire-domain sinusoidal basis functions on each resonant patch, the single higher-order circular attachment mode on each capacitor patch, and four PWS basis functions on each probe (excluding the one associated with the attachment mode). For the entire-domain sinusoidal basis functions, the (1,0), (1,2), (2,0), (2,2), (3,0), (3,2), (5,0), (7,0) and (9,0) modes were used for the $x$-directed current, while the (2,0) and (2,1) modes were used for the $y$-directed current. The feed network was modelled with Sonnet's circuit analysis module. Table 4.3 shows how the computer-memory requirements, for the storage of the interaction matrix, varies among the three codes. It can be seen that the memory requirements of the SDMM are once again substantially lower then that of the other two codes. Also, for the SDMM, the amount of duplicate entries in the interaction matrix equates to 83.11%.

**Table 4.3**
Computer memory required for the storage of the interaction matrix associated with the four-element horizontally-polarised antenna array.

| Method | Unknowns | Memory (MB) |
|---|---|---|
| IE3D | 4216 | 271.2 |
| FEKO | 2944 | 132.3 |
| SDMM | 84 | 0.108 |

Figure 4.42 shows the simulated reflection coefficient at the input port of the feed network. It can be seen that there is good agreement between the results of all three codes. The simulated 10 dB return-loss bandwidths are shown in Table 4.4, from which it can be seen that the agreement is also quite good. Figure 4.43 shows the simulated radiation patterns in the *E*-plane and the *H*-plane of the antenna array. The cross-polar levels in both planes fall well below the range of the graph. In terms of the radiation patterns, the three codes show very good agreement. The antenna gain, as simulated by IE3D, however, appears to be a fraction higher than that of the other two codes. It can also be seen that the beamwidth in the *H*-plane is narrowed due to the vertical alignment of the antenna elements.

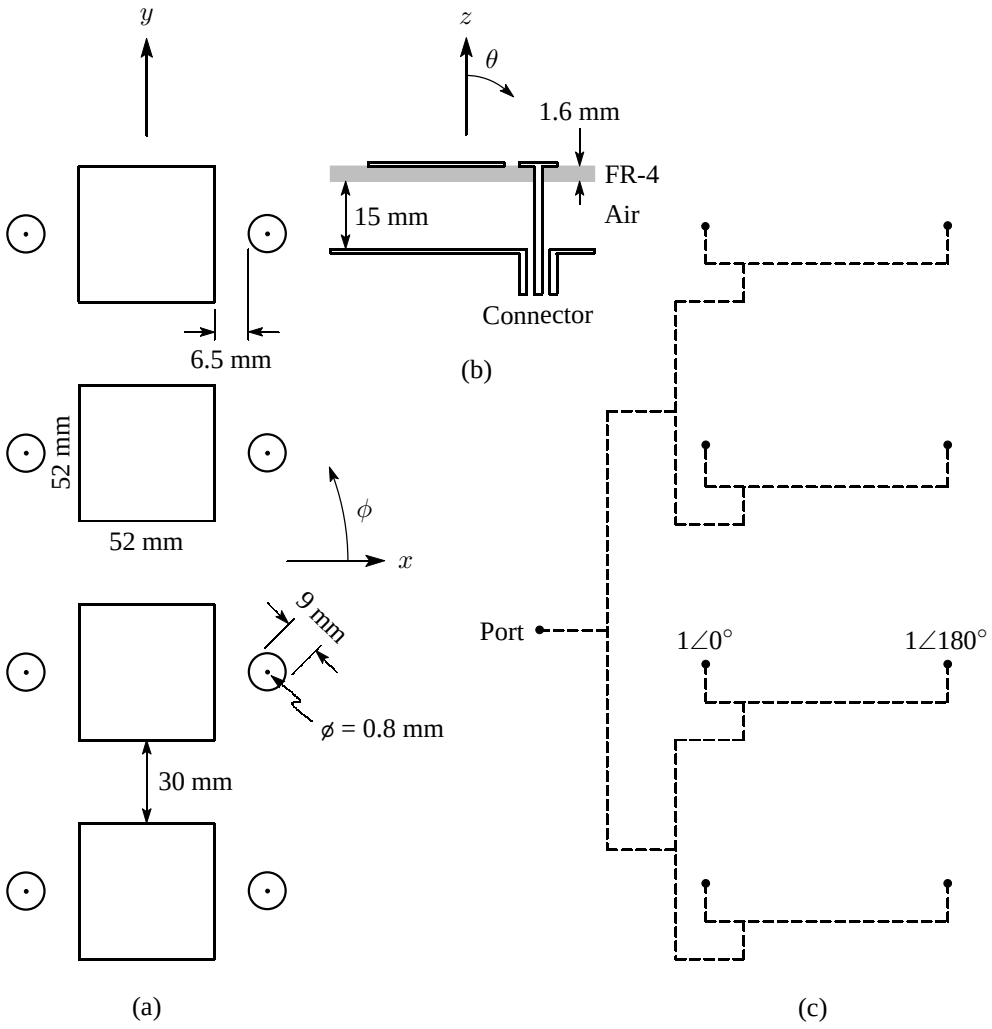


**Figure 4.41** Geometry of the four-element horizontally-polarised array. (a) Top view of the array. (b) Side view of the multilayered substrate with $\varepsilon_r = 4.25$ and $\tan\delta_\varepsilon = 0.02$ for the FR-4 layers and with $\varepsilon_r = 1$ and $\tan\delta_\varepsilon = 0$ for the air layer. (c) Schematic of the feed network.

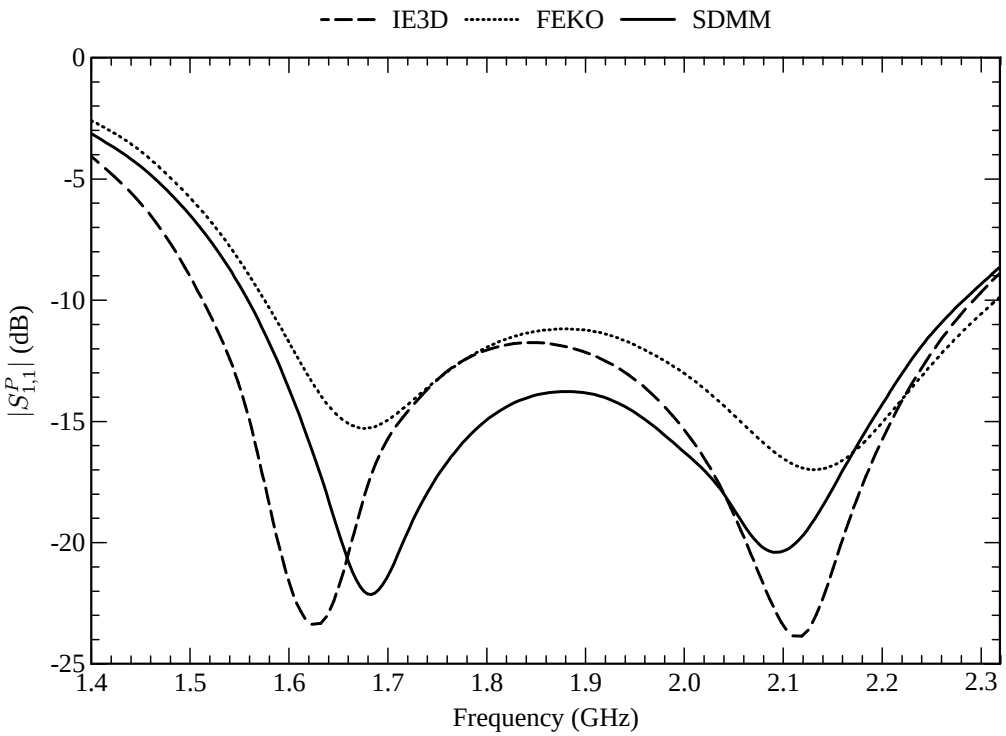


**Figure 4.42** Reflection coefficient at the input port of the feed network for the four-element horizontally-polarised array.

**Table 4.4**
10 dB Return-loss bandwidth at the input port of the four-element horizontally-polarised antenna array.

| Method | Bandwidth (%) |
|---|---|
| IE3D | 41.1 |
| FEKO | 38.6 |
| SDMM | 38.5 |

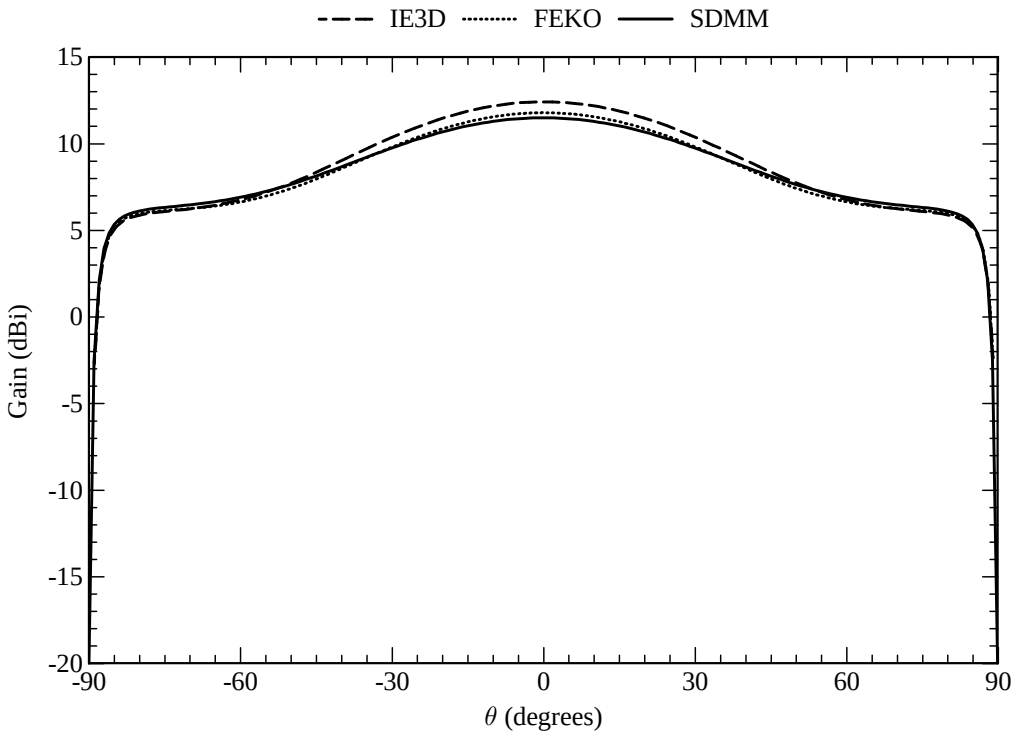


(a)

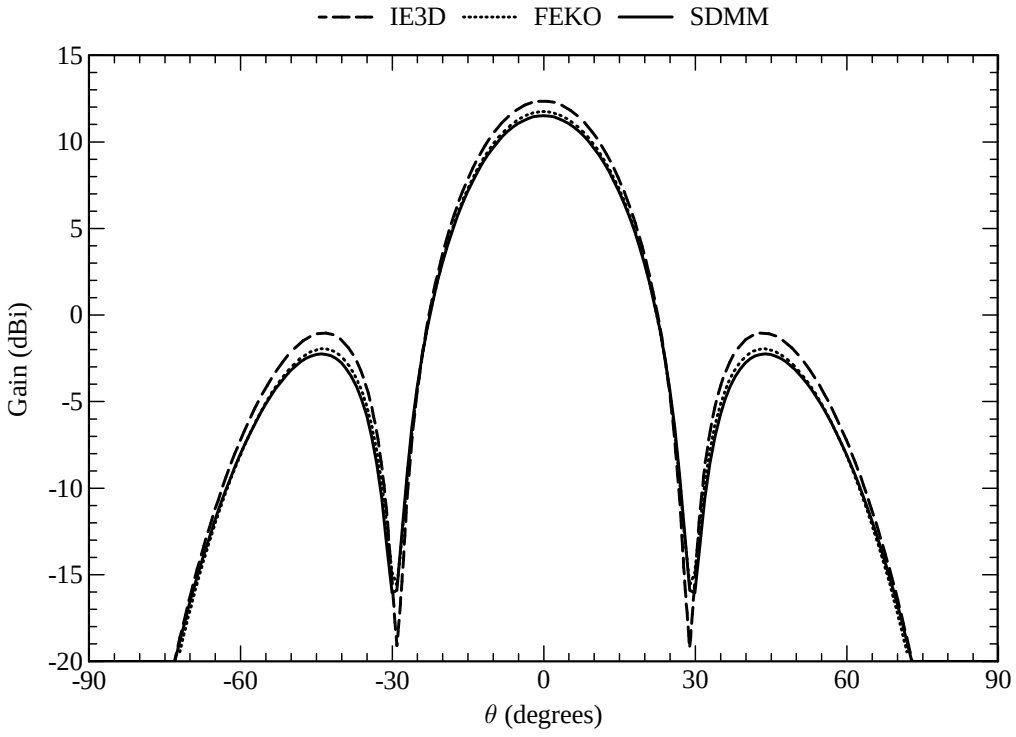


(b)

**Figure 4.43** Radiation patterns (at 1.8 GHz) of the four-element horizontally-polarised array. (a) Radiation pattern in the $E$-plane ($\phi = 0^\circ$). (b) Radiation pattern in the $H$-plane ($\phi = 90^\circ$).

### 4.4.6 Four-Element $\pm 45^\circ$ Slant-Polarised Array

Linear antenna arrays with $\pm 45^\circ$ slant polarisation are nowadays very popular for use on cellular base stations. Like other dual-polarised antennas, these antennas also have two ports, one for the $+45^\circ$ polarisation and one for the $-45^\circ$ polarisation. They are usually required to have a wide beamwidth in the azimuth plane and a narrow beamwidth in the elevation plane. To achieve these requirements, they are therefore usually also constructed as linear arrays. Figure 4.44 shows the geometry of such an array that can be realised by means of patch antenna elements with capacitive feed probes.

The array can be viewed as two subarrays, each consisting of two dual-polarised elements. In each subarray, the probes that are diagonally opposite to each other, provide the one polarisation, while the other two probes provide the orthogonal polarisation. The two probes that are diagonally opposite to each other, are excited exactly out of phase (i.e. a $180^\circ$ phase difference) so that the co-polarised fields add constructively and the cross-polarised fields cancel out. The input impedance at a specific probe is a function of the self-impedance at that probe as well as the mutual impedance between that probe and all the other probes. This array was designed by taking into account only the mutual impedance between two diagonally opposite probes in each subarray. The size of the capacitor patches, as well as the separation distance between them and the resonant patches, was then altered until (4.6) to (4.9) were satisfied for the two diagonally opposite probes. The array was designed so that the input impedance at each port is equal to 50 $\Omega$.

The electric current density on the structure was modelled with eighteen entire-domain sinusoidal basis functions on each resonant patch, the single higher-order circular attachment mode on each capacitor patch, and four PWS basis functions on each probe (excluding the one associated with the attachment mode). For the entire-domain sinusoidal basis functions, the (1,0), (1,2), (2,0), (2,1), (3,0), (3,2), (5,0), (7,0) and (9,0) modes were used for the $+45^\circ$-directed current, while the same set of modes were also used for the $-45^\circ$-directed current. The feed network was modelled with Sonnet's circuit analysis module. Table 4.5 shows how the computer-memory requirements, for the storage of the interaction matrix, varies among the three codes. It can be seen that the memory requirements of the SDMM are once again substantially lower then that of the other two codes. Also, for the SDMM, the amount of duplicate entries in the interaction matrix equates to 83.41%.

**Table 4.5**
Computer memory required for the storage of the interaction matrix associated with the four-element $\pm 45^\circ$ slant-polarised antenna array.

| Method | Unknowns | Memory (MB) |
|---|---|---|
| IE3D | 4076 | 253.5 |
| FEKO | 2912 | 129.4 |
| SDMM | 112 | 0.191 |

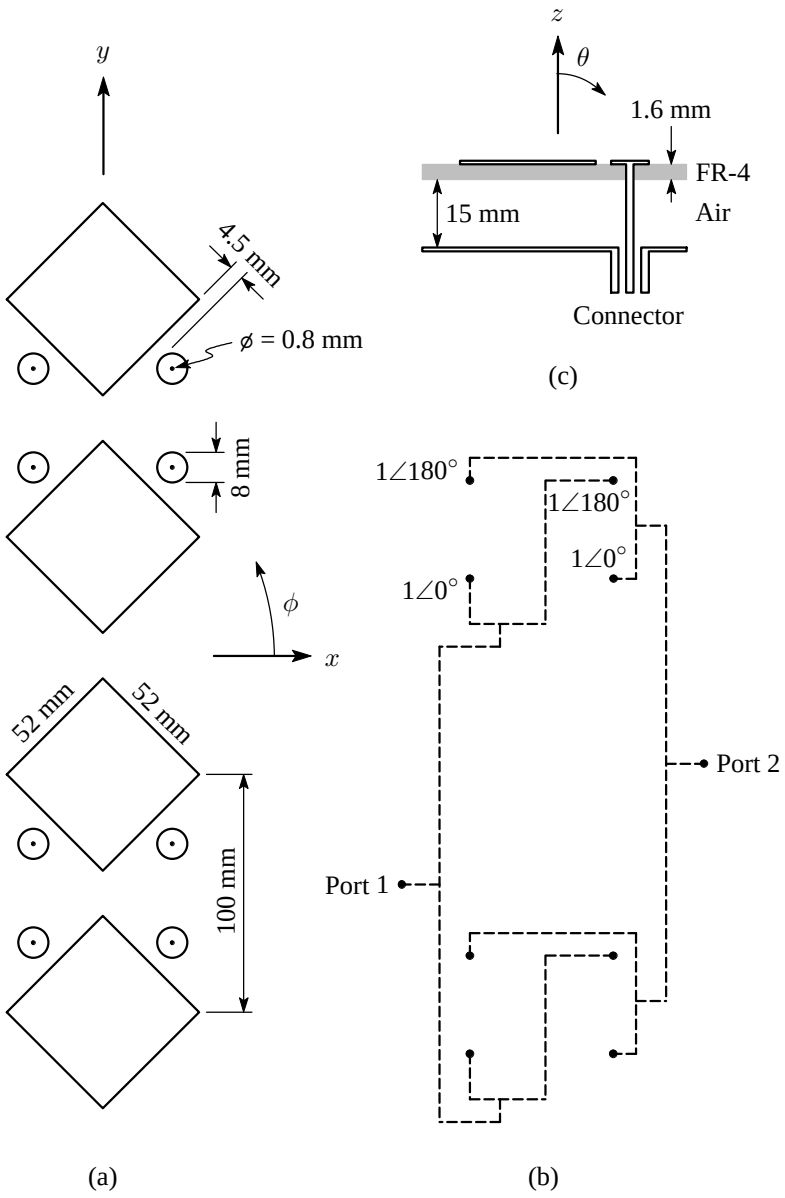


**Figure 4.44** Geometry of the four-element $\pm 45^{\circ}$ slant-polarised array. (a) Top view of the array. (b) Side view of the multilayered substrate with $\varepsilon_r = 4.25$ and $\tan\delta_\varepsilon = 0.02$ for the FR-4 layers and with $\varepsilon_r = 1$ and $\tan\delta_\varepsilon = 0$ for the air layer. (c) Schematic of the feed network.

Figure 4.45(a) shows the simulated reflection coefficient at port 1 of the feed network, while Figure 4.45(b) shows the simulated coupling between the two ports of the feed network. The simulated 10 dB return-loss bandwidths for port 1 are shown in Table 4.6. For the reflection coefficient, the results of the SDMM lies between those of IE3D and FEKO, while all three codes compare fairly well in terms of the coupling results. The coupling, as simulated by IE3D, is slightly higher than as simulated by the other two codes. Overall though, the impedance bandwidth of the array seems to be satisfactory for most cellular applications (the array was designed to roughly operate within the GSM 1800 frequency band, but was not optimised as such), while the decoupling of the two ports is close to the 25 dB to 30 dB that is normally used for cellular applications [194, 195].

**Table 4.6**
10 dB Return-loss bandwidth at port 1 of the four-element $\pm 45^{\circ}$ slant-polarised antenna array.

| Method | Bandwidth (%) |
|---|---|
| IE3D | 29.8 |
| FEKO | 27.8 |
| SDMM | 27.0 |

The gain associated with the co-polarised radiation patterns, $G_{\text{copol}}$, as well as the gain associated with the cross-polarised radiation pattern, $G_{\text{xpol}}$, can be calculated as

$$G_{\text{copol}}(\theta,\phi) = \frac{4\pi \left| E^{\text{scat}}_{\text{copol}}(\theta,\phi) \right|^2}{2\eta_{(0)} P_{\text{in}}} \tag{4.10}$$

and

$$G_{\text{xpol}}(\theta,\phi) = \frac{4\pi \left| E^{\text{scat}}_{\text{xpol}}(\theta,\phi) \right|^2}{2\eta_{(0)} P_{\text{in}}}, \tag{4.11}$$

where the absolute values of the co-polarised and cross-polarised electric fields, $E^{\text{scat}}_{\text{copol}}$ and $E^{\text{scat}}_{\text{xpol}}$, are given by

$$\left| E^{\text{scat}}_{\text{copol}}(\theta,\phi) \right| = \left| \frac{E^{\text{scat}}_{\theta}(\theta,\phi) + E^{\text{scat}}_{\phi}(\theta,\phi)}{\sqrt{2}} \right| \tag{4.12}$$

and

$$\left| E^{\text{scat}}_{\text{xpol}}(\theta,\phi) \right| = \left| \frac{E^{\text{scat}}_{\theta}(\theta,\phi) - E^{\text{scat}}_{\phi}(\theta,\phi)}{\sqrt{2}} \right| \tag{4.13}$$

respectively. Figure 4.46 shows the simulated co-polarised and cross-polarised radiation patterns in the azimuth and elevation planes of the antenna array. From these it can be seen that the agreement between the three codes is very good, and that the array has a cross-polar discrimination factor of about 18 dB to 20 dB. This should suffice for most cellular applications [195, 196]. The elevation beamwidth can be decreased by adding more elements to the array. This will also increase the gain of the array.

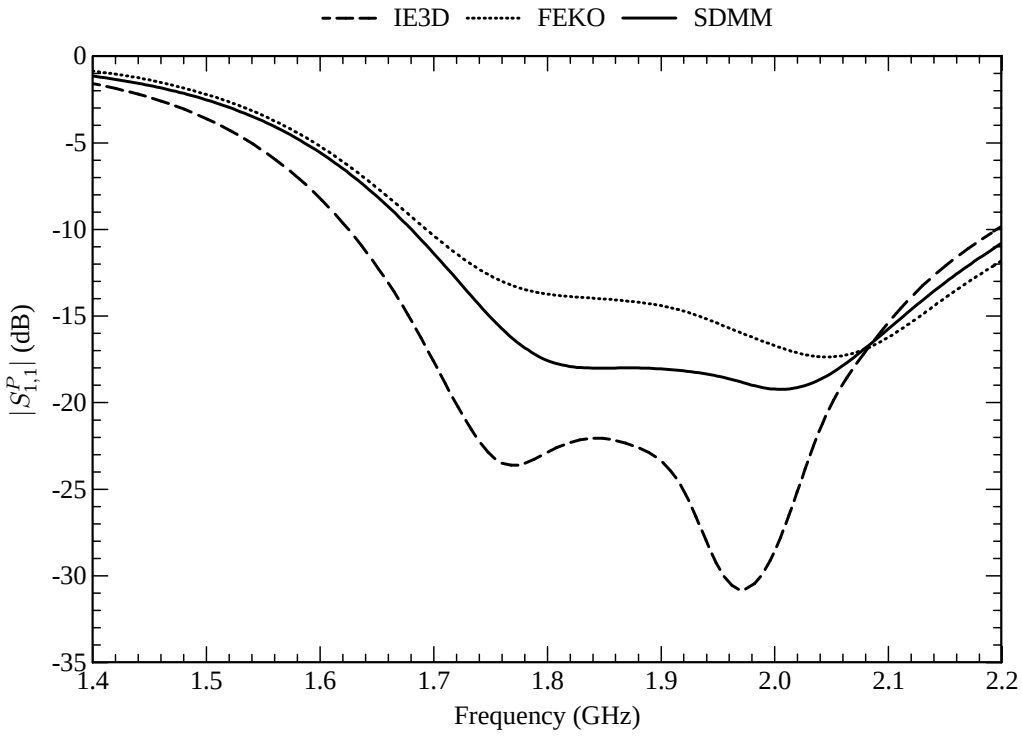


(a)

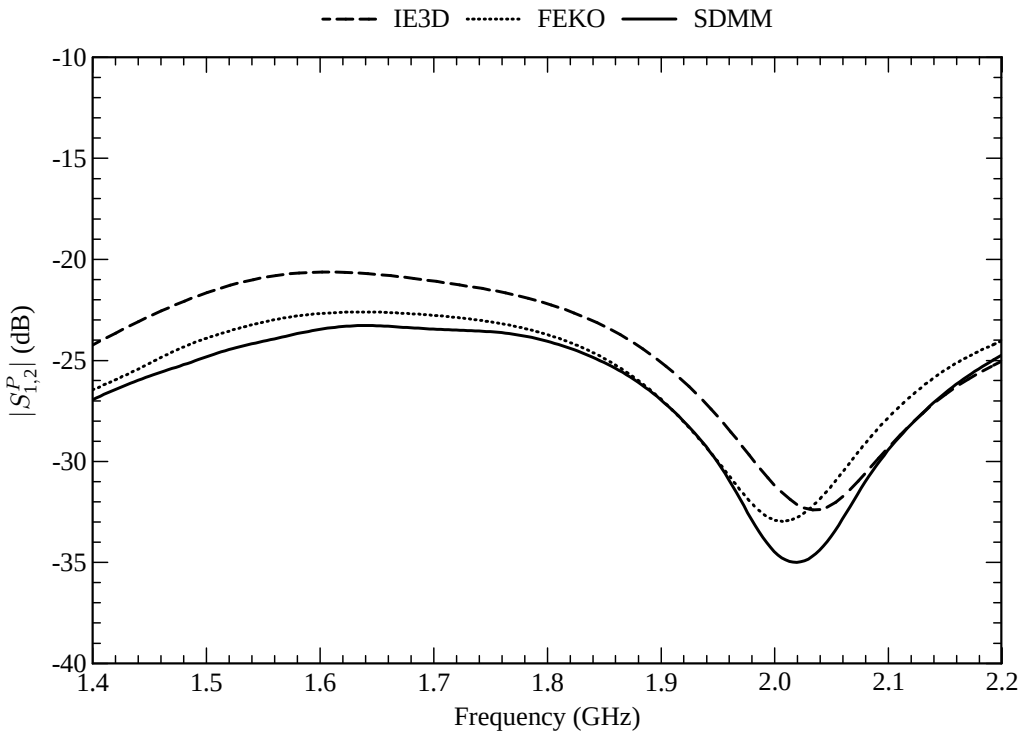


(b)

**Figure 4.45** *S*-parameters of the four-element $\pm 45^\circ$ slant-polarised array. (a) Reflection coefficient at port 1 of the feed network. (b) Coupling between the two ports of the feed network.

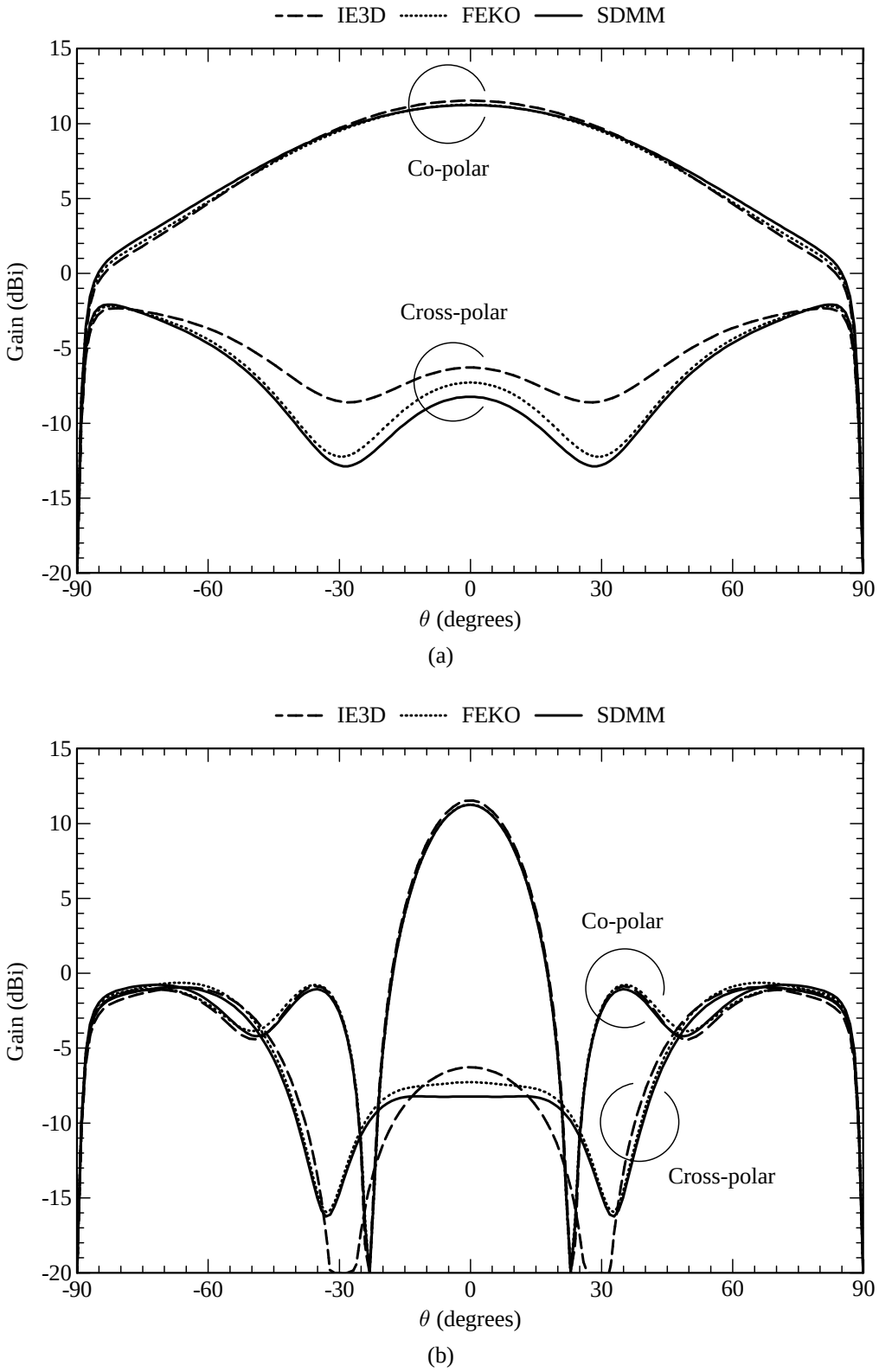


**Figure 4.46** Radiation patterns (at 1.8 GHz) of the four-element $\pm 45^{\circ}$ slant-polarised array. (a) Radiation pattern in the azimuth plane ($\phi = 0^{\circ}$). (b) Radiation pattern in the elevation plane ($\phi = 0^{\circ}$).

### 4.4.7 Five-Element $\pm 45^\circ$ Slant-Polarised Array

An alternative form of the $\pm 45^\circ$ slant-polarised antenna array is shown in Figures 4.47. It consists of a zig-zag type of arrangement where adjacent antenna elements are positioned in a back-to-back configuration. Of the five resonant patches, the bottom four patches provide the one polarisation, while the top four patches provide the orthogonal polarisation. It can therefore be seen that the topmost and bottommost patches only provide one polarisation each, but that the three patches in the middle provide both polarisations. All of the probes connected to port 1, are associated with the one polarisation, while those connected to port 2, are associated with the orthogonal polarisation. The antenna array was designed by only taking into account the mutual coupling between two adjacent probes. By following the same approach as in Section 4.4.3, the input impedance at each port was designed to be equal to 50 $\Omega$.

The electric current density on the structure was modelled with eighteen entire-domain sinusoidal basis functions on each resonant patch, the single higher-order circular attachment mode on each capacitor patch, and four PWS basis functions on each probe (excluding the one associated with the attachment mode). For the entire-domain sinusoidal basis functions, the (1,0), (1,2), (2,0), (2,1), (3,0), (3,2), (5,0), (7,0) and (9,0) modes were used for the $+45^\circ$-directed current, while the same set of modes were also used for the $-45^\circ$-directed current. The feed network was modelled with IE3D, after which the *S*-parameters of the array and the feed network were cascaded by means of Sonnet's circuit analysis module. Table 4.7 shows how the computer-memory requirements, for the storage of the interaction matrix associated with the array, varies among the three full-wave codes. It can be seen that the memory requirements of the SDMM are once again substantially lower then that of the other two codes. Also, for the SDMM, the amount of duplicate entries in the interaction matrix equates to 82.42%. An physical model of this antenna, as shown in Figure 4.48, was also constructed in order to compare the simulations to measurements.

**Table 4.7**
Computer memory required for the storage of the interaction matrix associated with the five-element $\pm 45^\circ$ slant-polarised antenna array.

| Method | Unknowns | Memory (MB) |
|---|---|---|
| IE3D | 5682 | 492.6 |
| FEKO | 3472 | 183.9 |
| SDMM | 130 | 0.258 |

Figure 4.49 shows the simulated and measured gain (all cases including losses in the feed network) of the antenna, from which it can be seen that the agreement between the three codes is very good, but that the measured gain is only slightly lower than the simulated gain. This can be ascribed to the rather small ground plane that was used for the physical antenna model.

Figure 4.50(a) shows the measured and simulated reflection coefficient at port 1 of the feed network, while Figure 4.50(b) shows the measured and simulated coupling between the two ports of the feed network. The simulated 10 dB return-loss bandwidths for port 1 are shown in Table 4.8. In terms of the reflection coefficient, there is close agreement between the measured results and the IE3D results, as well as close agreement between the SDMM results and the FEKO results. There is a small difference between the measured/IE3D results and the SDMM/FEKO results. The overall bandwidth, however, appears to be more or less the same for all four sets of results. As far as the coupling between the two ports goes, the measured results and simulated results all agree fairly well. From these results it can be seen that the impedance bandwidth of the antenna is sufficiently wide for most cellular applications and that the decoupling between the two ports seem to be slightly better than that of the array in Section 4.4.6.

**Table 4.8**
10 dB Return-loss bandwidth at port 1 of the five-element $\pm 45^{\circ}$ slant-polarised antenna array.

| Method | Bandwidth (%) |
|---|---|
| Measured | 28.4 |
| IE3D | 32.4 |
| FEKO | 30.0 |
| SDMM | 28.7 |

Figure 4.51 shows the measured and simulated co-polarised and cross-polarised radiation patterns in the azimuth plane of the antenna array, while Figure 4.52 shows the measured and simulated co-polarised and cross-polarised radiation patterns in the elevation plane of the antenna array. From these it can be seen that the agreement between the three codes is quite good and that the simulations compare fairly well with the measurements, given the finite size of the ground plane that was used for the physical antenna model. In this case it can be seen that the beamwidth of the co-polarised pattern in the azimuth plane is slightly narrower than that of the array in Section 4.4.6. This is due to the somewhat larger horizontal dimensions of the array. The cross-polar discrimination of this array is better than 20 dB over most of the usable beamwidth in the two planes.

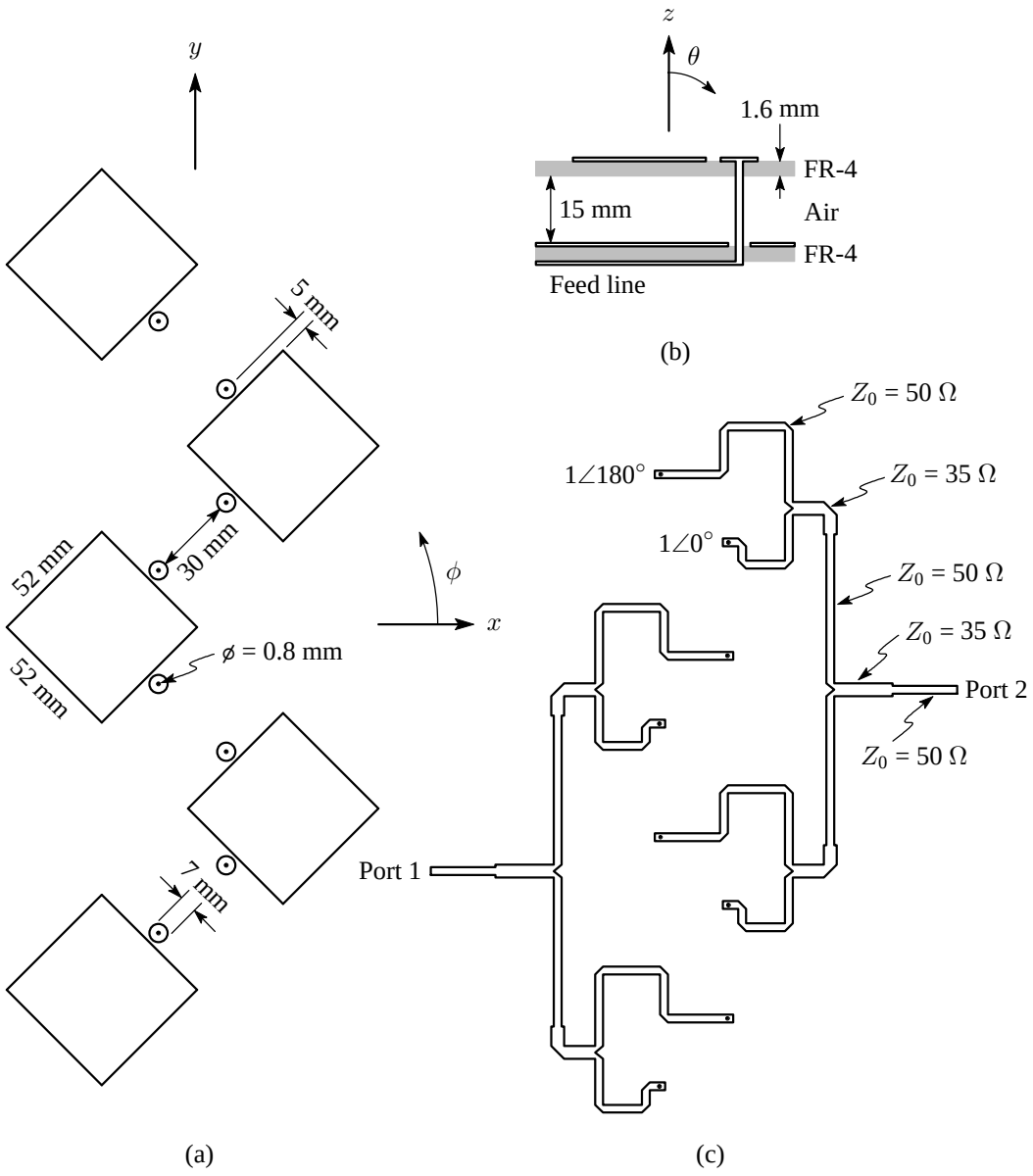


**Figure 4.47** Geometry of the five-element ±45° slant-polarised array. (a) Top view of the array. (b) Side view of the multilayered substrate with $\varepsilon_r = 4.25$ and $\tan\delta_\varepsilon = 0.02$ for the FR-4 layers and with $\varepsilon_r = 1$ and $\tan\delta_\varepsilon = 0$ for the air layer. (c) Feed network for the array.

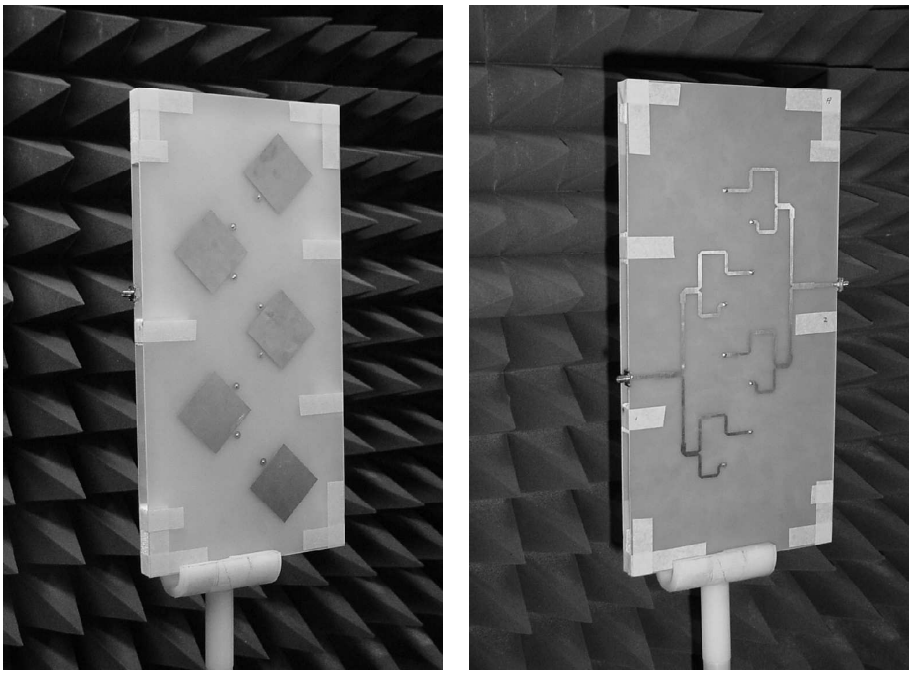

(a) (b)

**Figure 4.48** Photographs of the five-element $\pm 45^{\circ}$ slant-polarised array. (a) Antenna elements. (b) Feed network.

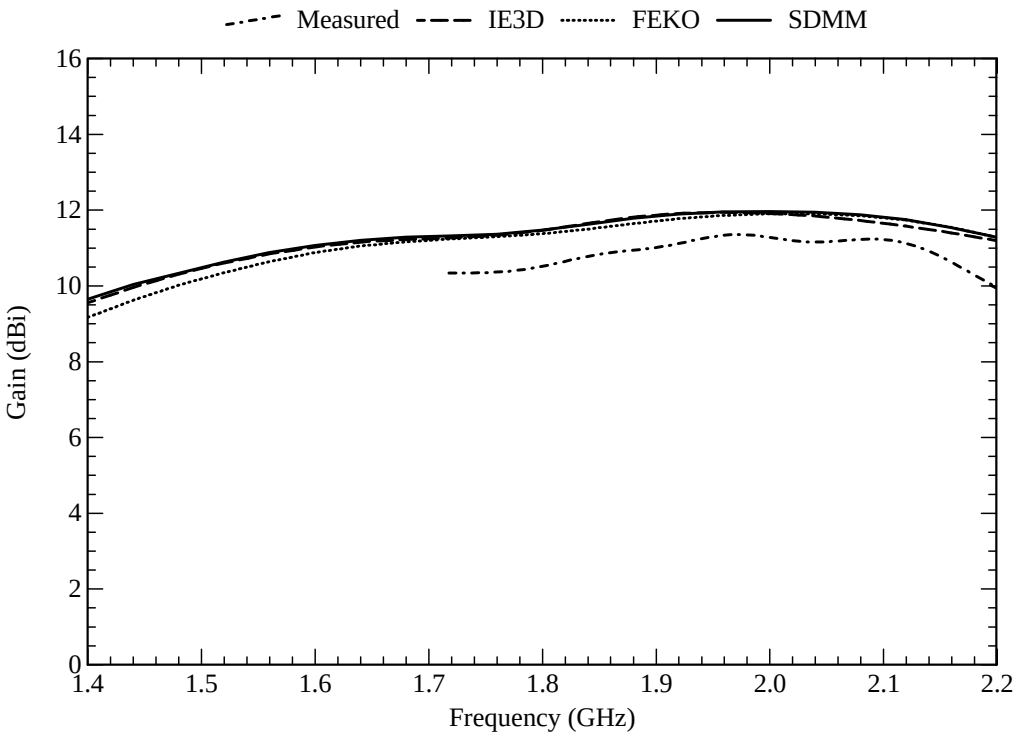


**Figure 4.49** Gain of the five-element $\pm 45^{\circ}$ slant-polarised array.

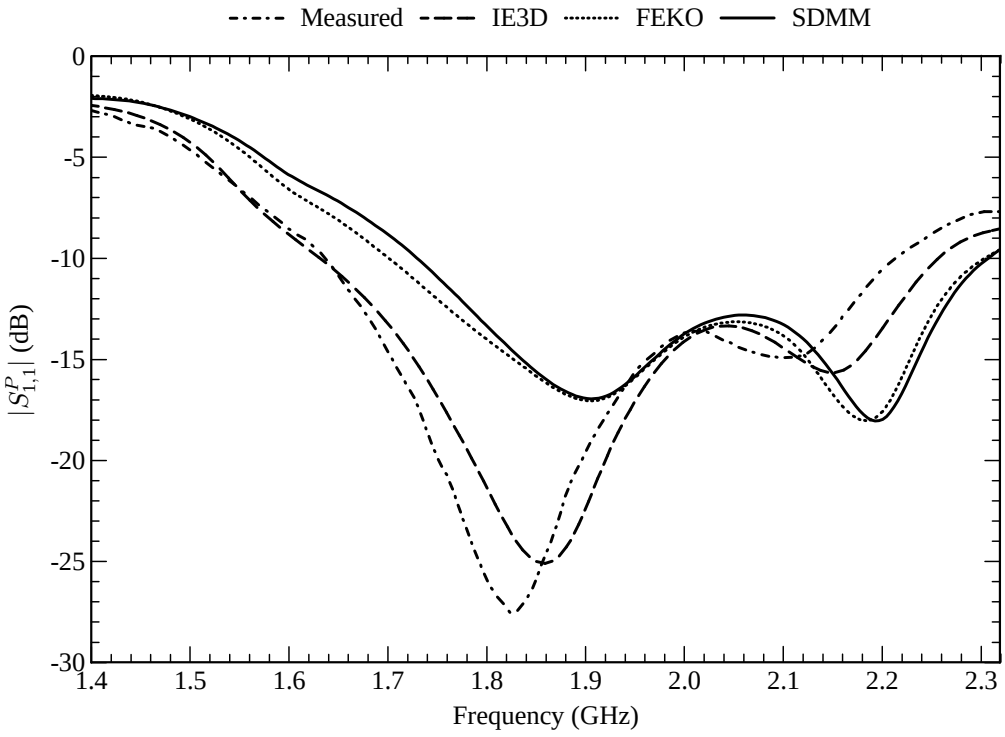


(a)

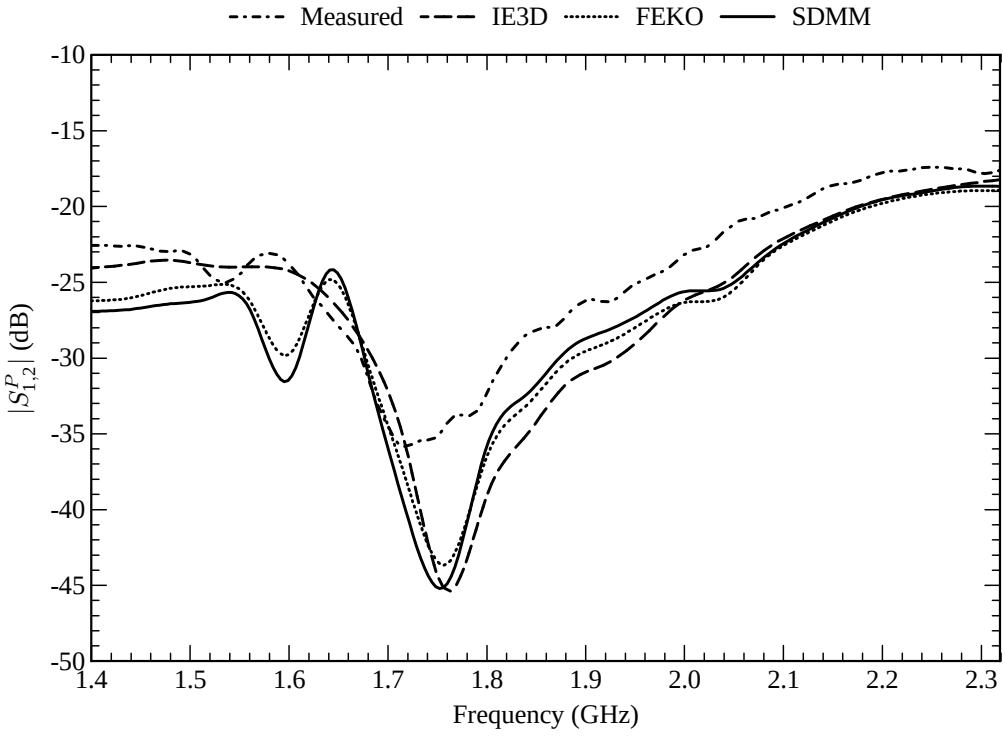


(b)

**Figure 4.50** *S*-parameters of the five-element $\pm 45^\circ$ slant-polarised array. (a) Reflection coefficient at port 1 of the feed network. (b) Coupling between the two ports of the feed network.

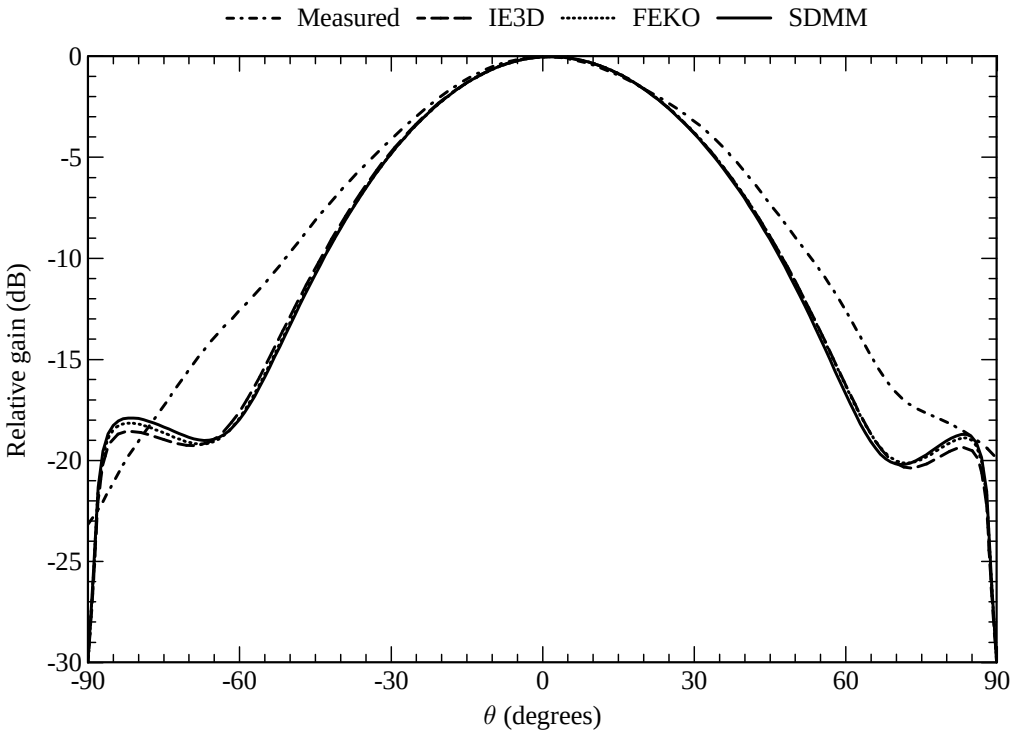


(a)

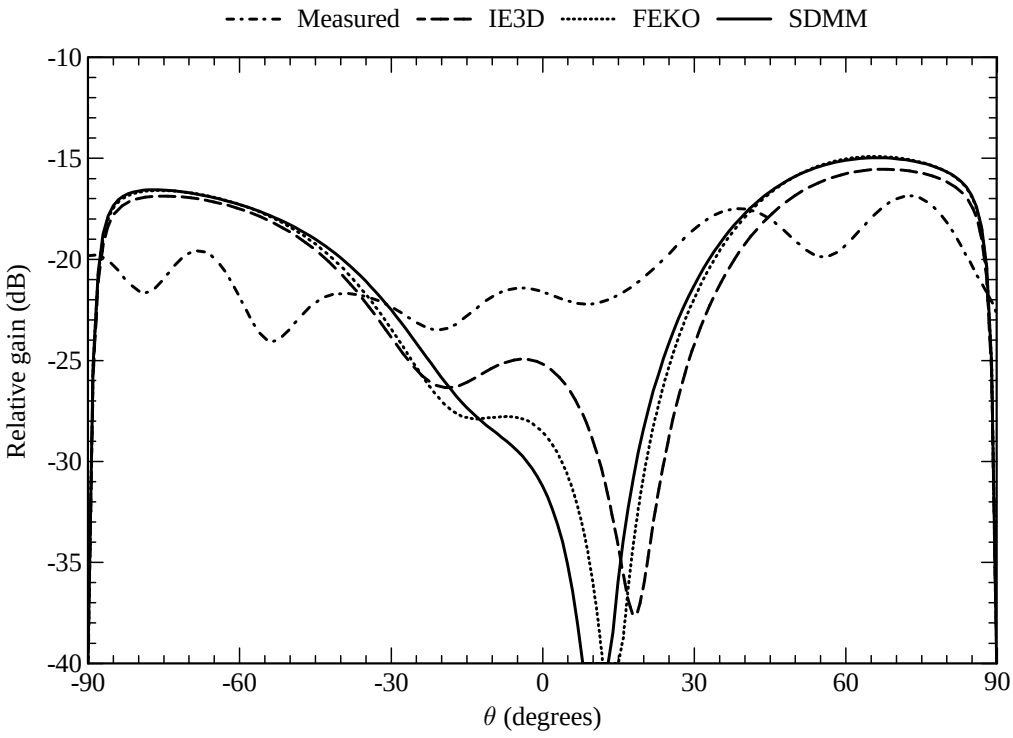


(b)

**Figure 4.51** Radiation patterns (at 1.8 GHz) in the azimuth plane ($\phi = 0^\circ$) of the five-element $\pm 45^\circ$ slant-polarised array. (a) Co-polarised pattern. (b) Cross-polarised pattern.

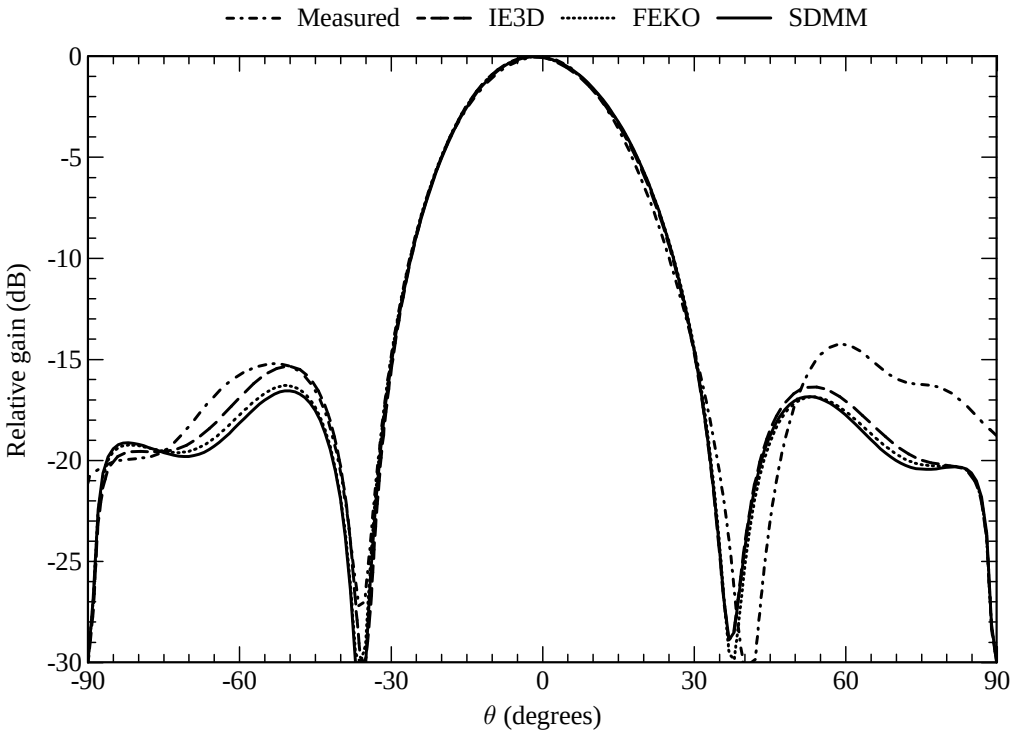


(a)

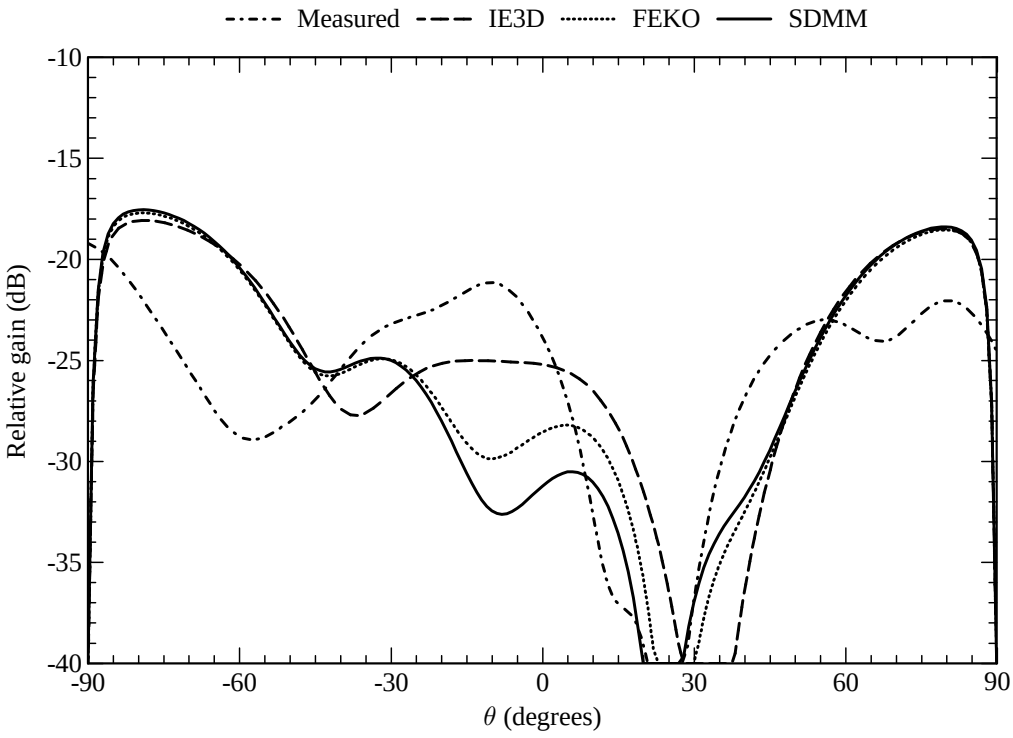


(b)

**Figure 4.52** Radiation patterns (at 1.8 GHz) in the elevation plane ($\phi = 90^\circ$) of the five-element $\pm 45^\circ$ slant-polarised array. (a) Co-polarised pattern. (b) Cross-polarised pattern.

### 4.4.8 Nine-Element $\pm 45^\circ$ Slant-Polarised Array

Many cellular base station installations require antennas with higher gains and narrower elevation beamwidths than those that have been presented to far. This can be achieved by adding more elements to the antenna array, thereby extending the length of the array. In this section, an antenna array is presented that is more or less comparable in size to that of a typical high-gain cellular base station antenna.

Consider the antenna array in Figure 4.53. It is a somewhat larger version of the one in Section 4.4.7. The electric current density on the structure was modelled with eighteen entire-domain sinusoidal basis functions on each resonant patch, the single higher-order circular attachment mode on each capacitor patch, and four PWS basis functions on each probe (excluding the one associated with the attachment mode). For the entire-domain sinusoidal basis functions, the (1,0), (1,2), (2,0), (2,1), (3,0), (3,2), (5,0), (7,0) and (9,0) modes were used for the $+45^\circ$-directed current, while the same set of modes were also used for the $-45^\circ$-directed current. The feed network was modelled with Sonnet's circuit analysis module. Table 4.9 shows how the computer-memory requirements, for the storage of the interaction matrix associated with the array, varies among the three full-wave codes. It can be seen that the memory requirements of the SDMM are basically insignificant, but that those for the other two codes are greater than the available memory on most personal computers. For the SDMM, the amount of duplicate entries in the interaction matrix equates to 90.07%.

**Table 4.9**
Computer memory required for the storage of the interaction matrix associated with the nine-element $\pm 45^\circ$ slant-polarised antenna array.

| Method | Unknowns | Memory (MB) |
|---|---|---|
| IE3D | 7747 | 915.8 |
| FEKO | 6176 | 582.0 |
| SDMM | 242 | 0.894 |

Figure 4.54(a) shows the simulated reflection coefficient at port 1 of the feed network, while Figure 4.54(b) shows the simulated coupling between the two ports of the feed network. The simulated 10 dB return-loss bandwidths for port 1 are shown in Table 4.10. In terms of the reflection coefficient, there is close agreement between the SDMM results and the FEKO results, but there is a slight frequency shift when compared to the IE3D results. The overall bandwidth, however, appears to be more or less the same for all three sets of results. As far as the coupling between the two ports goes, the simulated results all agree fairly well. From these results it can be seen that the impedance bandwidth of the antenna is sufficiently wide for most cellular applications and that the decoupling between the two ports is also quite good.

**Table 4.10**
10 dB Return-loss bandwidth at port 1 of the nine-element $\pm 45^{\circ}$ slant-polarised antenna array.

| Method | Bandwidth (%) |
|---|---|
| IE3D | 20.8 |
| FEKO | 20.5 |
| SDMM | 19.4 |

Figure 4.55 shows the simulated co-polarised and cross-polarised radiation patterns in the azimuth and elevation planes of the antenna array. From these it can be seen that the agreement between the three codes is quite good. It can also be seen that the extra elements have raised the gain of the antenna and that the beamwidth in the elevation plane has been narrowed. The cross-polar discrimination of this array is also better than 20 dB over most of the usable beamwidth in the two principal planes.

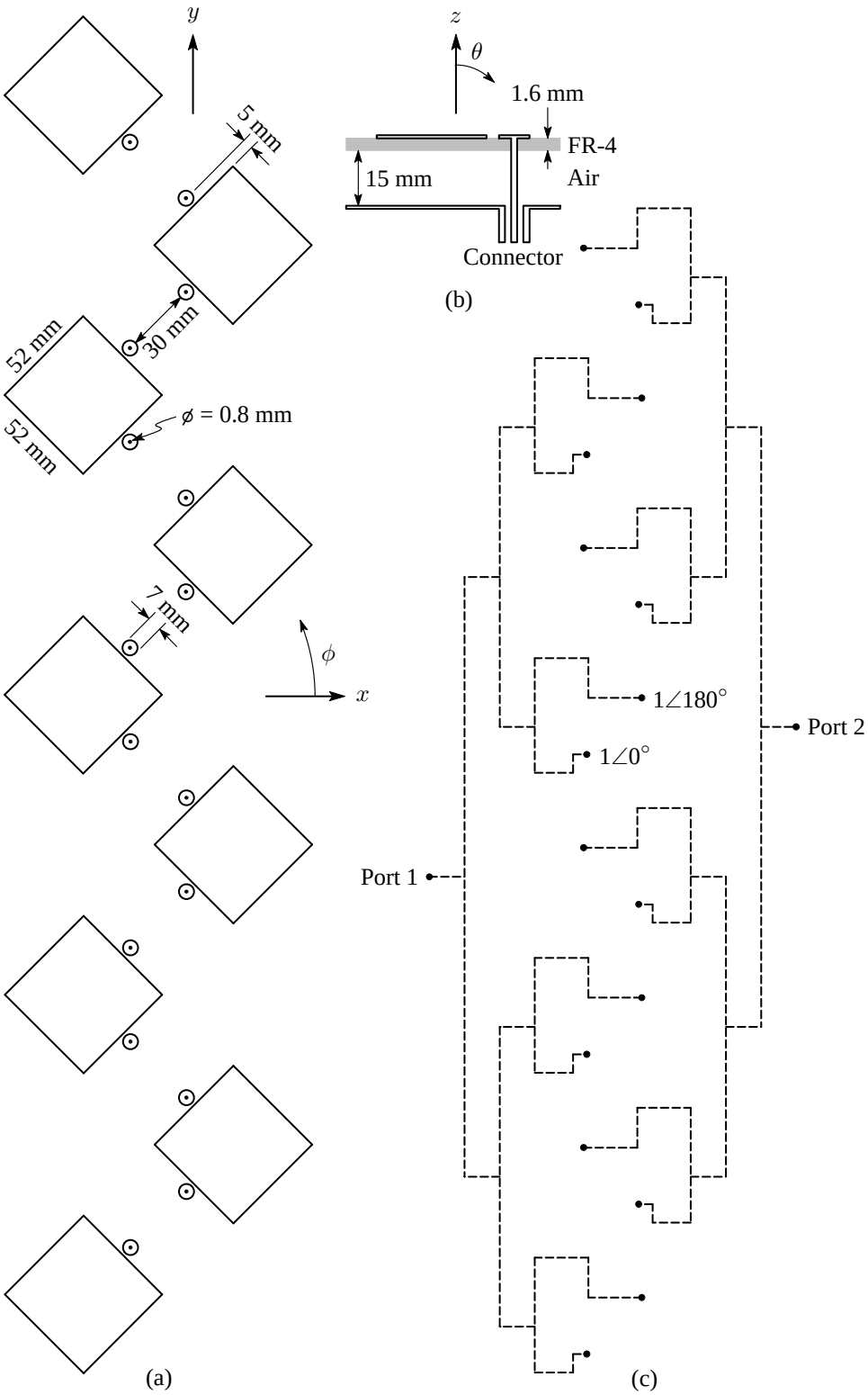


**Figure 4.53** Geometry of the nine-element $\pm 45^{\circ}$ slant-polarised array. (a) Top view of the array. (b) Side view of the multilayered substrate with $\varepsilon_r = 4.25$ and $\tan\delta_\varepsilon = 0.02$ for the FR-4 layers and with $\varepsilon_r = 1$ and $\tan\delta_\varepsilon = 0$ for the air layer. (c) Schematic of the feed network.

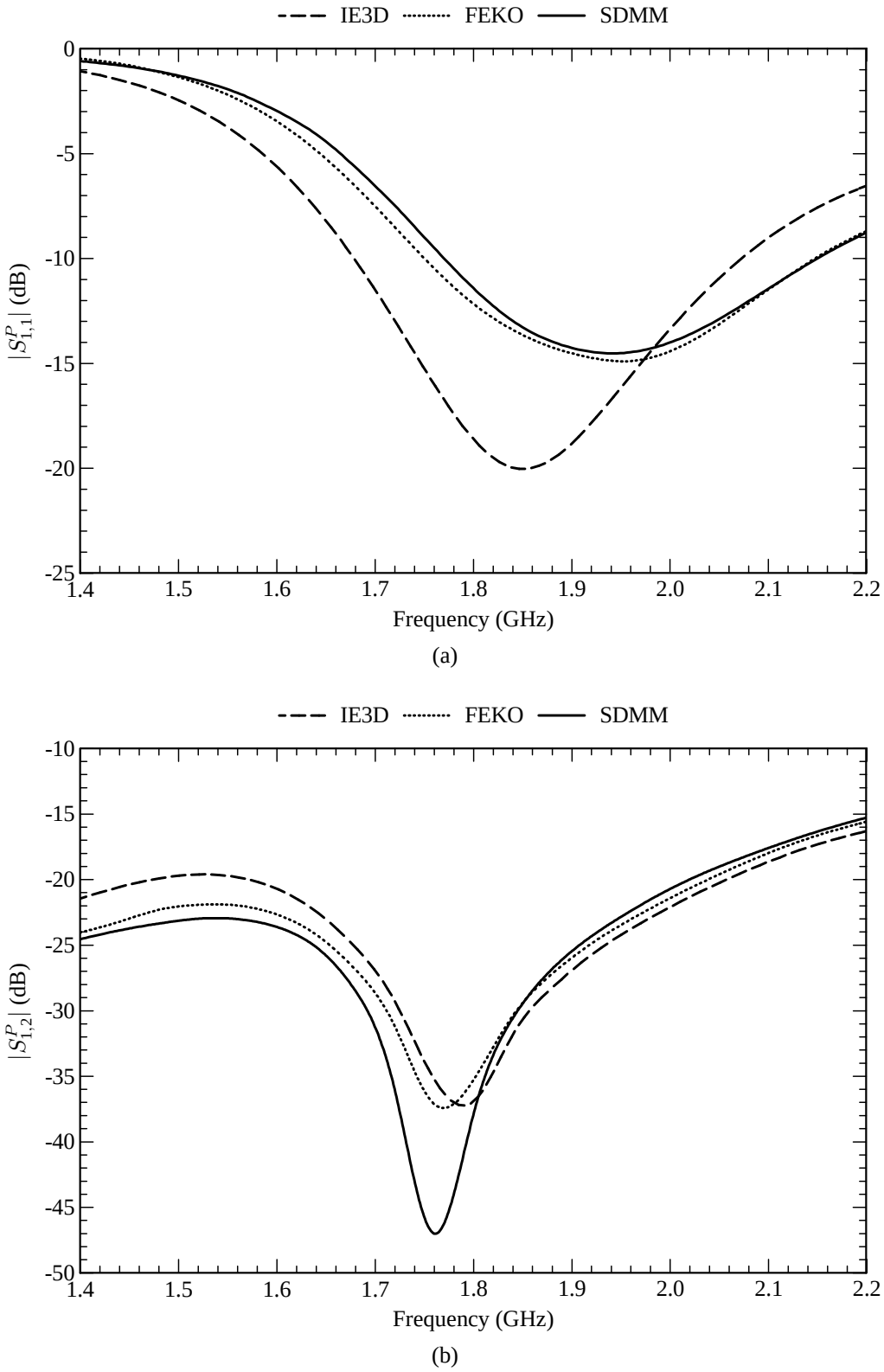


**Figure 4.54** *S*-parameters of the nine-element $\pm 45^\circ$ slant-polarised array. (a) Reflection coefficient at port 1 of the feed network. (b) Coupling between the two ports of the feed network.

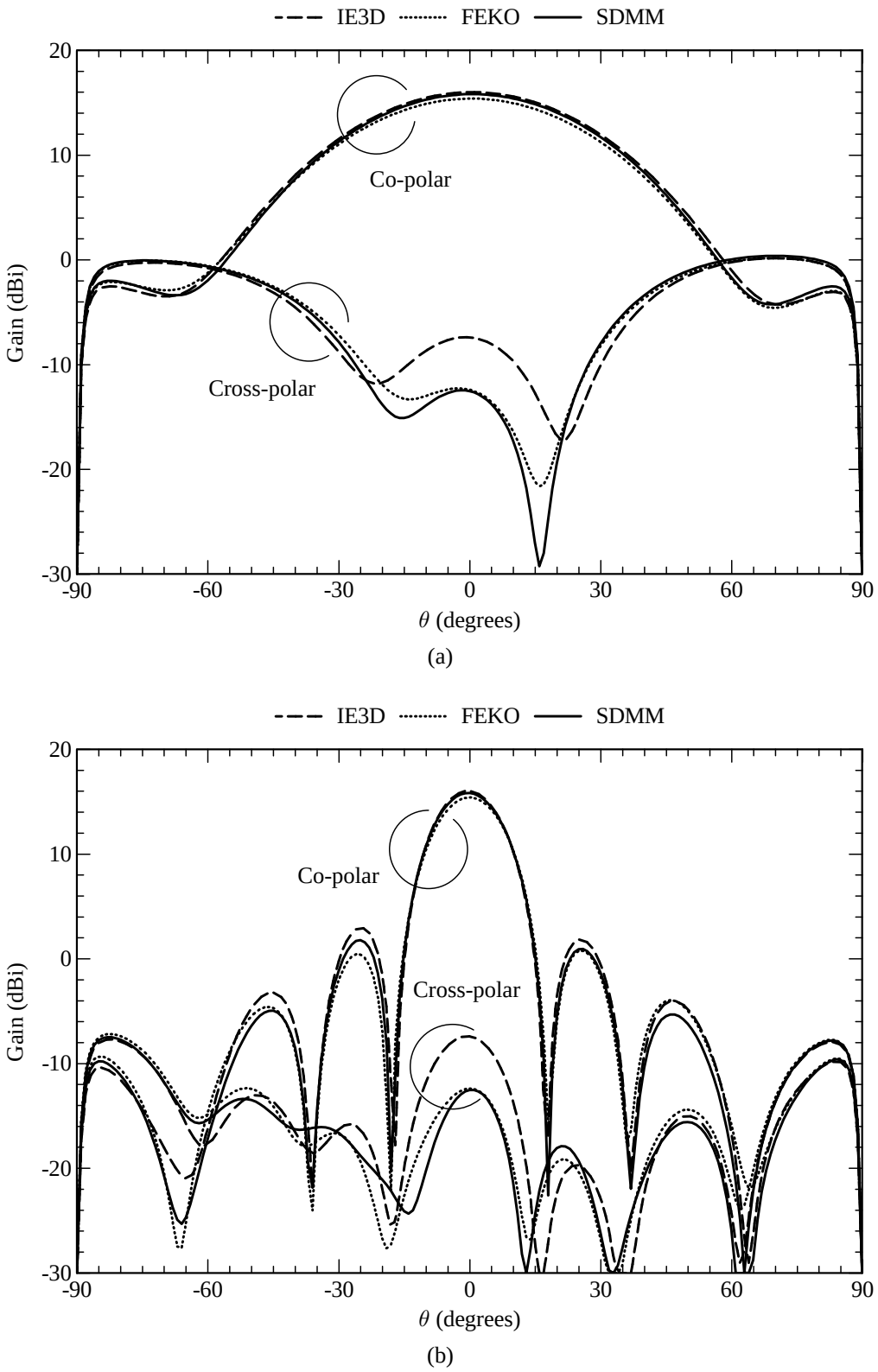


**Figure 4.55** Radiation patterns (at 1.8 GHz) of the nine-element $\pm 45^{\circ}$ slant-polarised array. (a) Radiation pattern in the azimuth plane ($\phi = 0^{\circ}$). (b) Radiation pattern in the elevation plane ($\phi = 0^{\circ}$).

### 4.4.9 Thirty Six-Element $\pm 45^\circ$ Slant-Polarised Array

The concept of adaptive antenna systems, also called smart antennas, has lately been a topic of extensive research. It can be used to increase the capacity of cellular communications systems. Essentially, it is an antenna array of which a relatively narrow beam can be steered towards the mobile subscriber. As such, the antenna effectively suppresses interference that comes from other directions. A common way to realise an adaptive antenna, is to place a number of linear antenna arrays next to each other, and to connect the input/output ports of the individual arrays by means of a suitable beamforming network [194, 197]. Usually, it is required that these arrays should only be able to scan in the azimuth plane [198].

In this section, four of the nine-element $\pm 45^\circ$ slant-polarised arrays, as presented in Section 4.4.8, are positioned next to each other in order to form an array that is suitable for adaptive beamforming in the azimuth plane. The geometry of the array is shown in Figure 4.56. The dimensions of the antenna elements, as well as the spacings between them, are exactly the same as those in Figure 4.53. Each subarray also has a feed network with two ports, similar to the one in Figure 4.53.

The electric current density on the structure was modelled with eighteen entire-domain sinusoidal basis functions on each resonant patch, the single higher-order circular attachment mode on each capacitor patch, and four PWS basis functions on each probe (excluding the one associated with the attachment mode). For the entire-domain sinusoidal basis functions, the (1,0), (1,2), (2,0), (2,1), (3,0), (3,2), (5,0), (7,0) and (9,0) modes were used for the $+45^\circ$-directed current, while the same set of modes were also used for the $-45^\circ$-directed current. The feed networks were modelled with Sonnet's circuit analysis module. Due to the size of the antenna array, it was only modelled with the SDMM, which makes extensive use of entire-domain basis functions. Table 4.11 illustrates how the computer-memory requirements of the SDMM would compare to that of IE3D and FEKO. It can be seen that, for a non-iterative solution, the memory requirements of the two commercial codes would be greater than the available memory on most personal computers. For the SDMM, the amount of duplicate entries in the interaction matrix equates to 97.55%.

**Table 4.11**
Computer memory required for the storage of the interaction matrix associated with the thirty six-element $\pm 45^\circ$ slant-polarised antenna array.

| Method | Unknowns | Memory |
|---|---|---|
| IE3D | 30988 | 14.3 GB (estimated) |
| FEKO | 24704 | 9.1 GB (estimated) |
| SDMM | 968 | 14.3 MB |

Figure 4.57 shows the coupling between the different subarrays. This includes coupling between

co-polar ports (e.g. two $+45^\circ$ ports), as well as coupling between cross-polar ports (e.g. a $+45^\circ$ port and a $-45^\circ$ port). As shown in Figure 4.56, subarray 1 represents a subarray at the edge of the array, while subarray 2 represents a subarray in the middle of the array. Figure 4.57(a) shows the coupling between subarray 1 and all of the other subarrays, while Figure 4.57(b) shows the coupling between subarray 2 and all of the other subarrays. From these two figures, it can be seen that the coupling between all ports in the array is relatively low. In most cases the coupling is below 30 dB.

Figure 4.58 shows the simulated co-polarised and cross-polarised radiation patterns in the azimuth and elevation planes of the antenna array when all the co-polar ports are driven with equal amplitude and phase. It can be seen that the horizontal distribution of the subarrays effectively narrows the beamwidth in the azimuth plane. The cross-polar discrimination of this array is in the order of 25 dB over most of the usable beamwidth in the two principal planes.

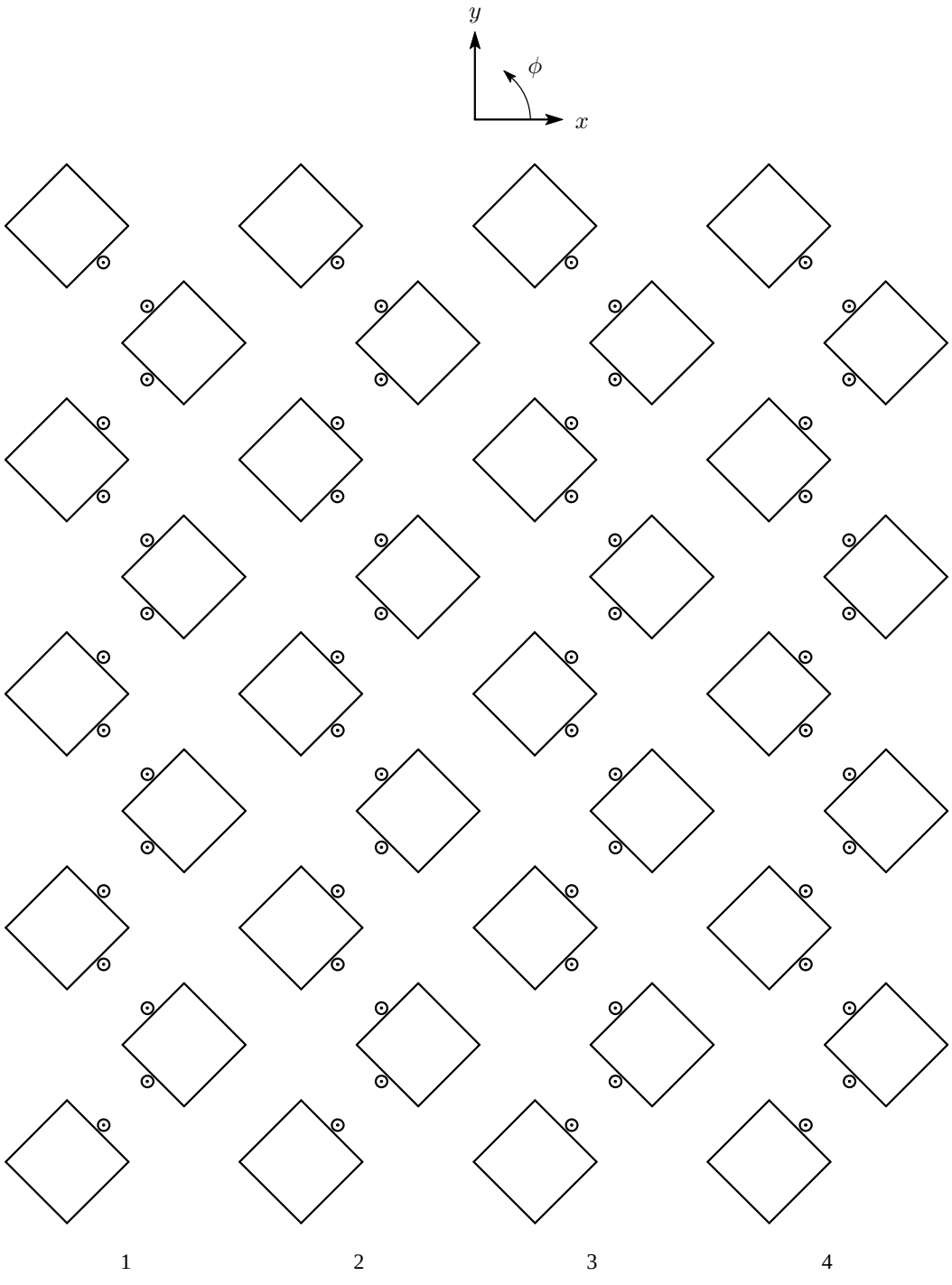


**Figure 4.56** Geometry of the thirty six-element $\pm 45^{\circ}$ slant-polarised array. This array consists of four linear subarrays that are positioned next to each other.

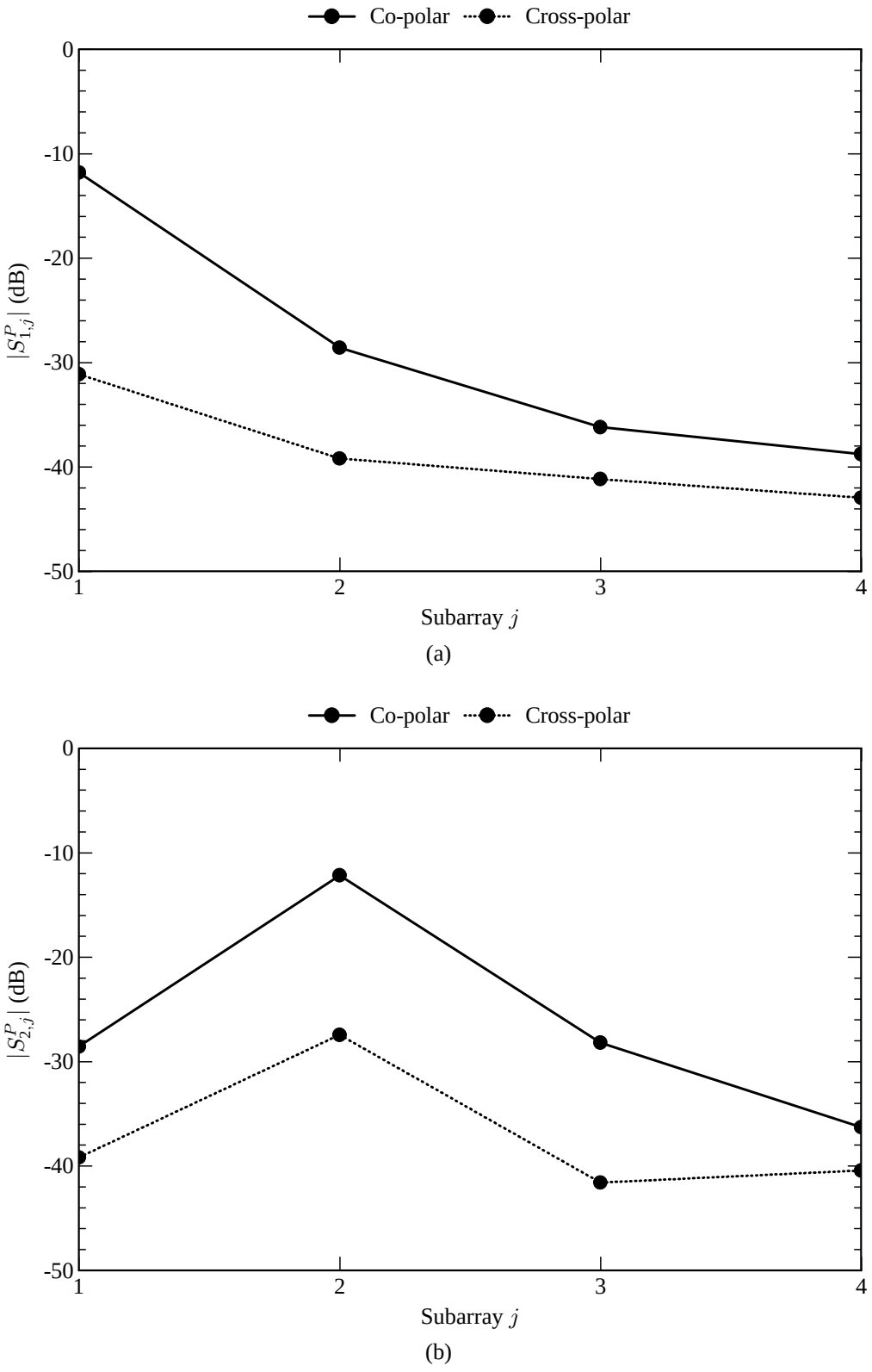


**Figure 4.57** Co-polar and cross-polar coupling (at 1.8 GHz) between the linear subarrays of the thirty six-element $\pm 45^\circ$ slant-polarised array. (a) Coupling to subarray 1. (b) Coupling to subarray 2.

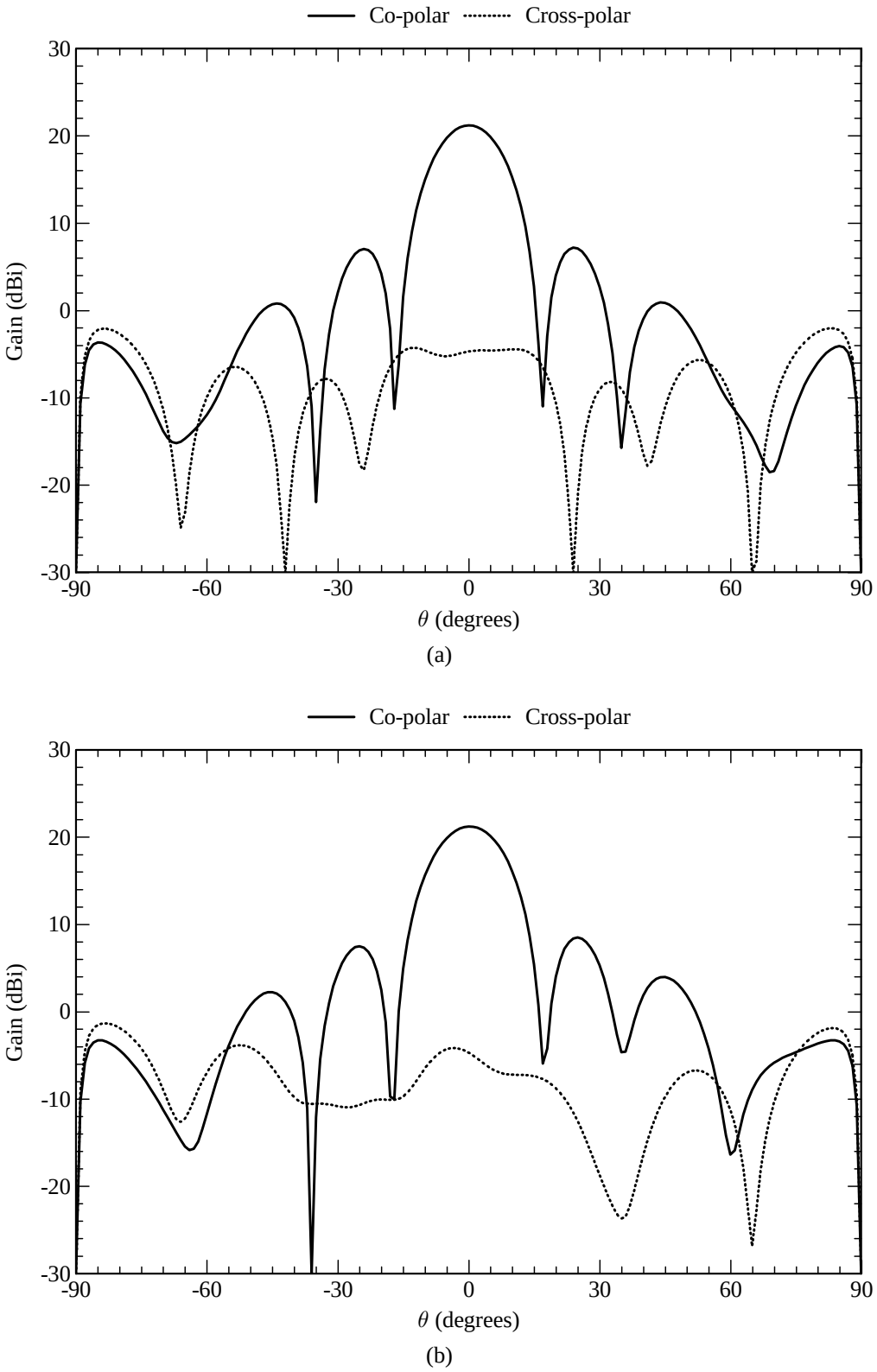


**Figure 4.58** Radiation patterns (at 1.8 GHz) of the thirty six-element $\pm 45^{\circ}$ slant-polarised array when the co-polar ports are excited with equal amplitude and phase. (a) Radiation pattern in the azimuth plane ($\phi = 0^{\circ}$). (b) Radiation pattern in the elevation plane ($\phi = 0^{\circ}$).

### 4.4.10 Eighty-Element $\pm 45^\circ$ Slant-Polarised Array

Lindmark [194] has shown how up to twelve subarrays can be used to realise an adaptive antenna. In order to illustrate the computational benefits of the SDMM for such large problems, this section presents an antenna array that consists of ten linear subarrays, each one being $\pm 45^\circ$ slant polarised. The geometry of the array is shown in Figure 4.59. The dimensions of the antenna elements, as well as the spacings between them, are exactly the same as those in Figure 4.44. Each subarray also has a feed network with two ports, one for each polarisation.

The electric current density on the structure was modelled with eighteen entire-domain sinusoidal basis functions on each resonant patch, the single higher-order circular attachment mode on each capacitor patch, and four PWS basis functions on each probe (excluding the one associated with the attachment mode). For the entire-domain sinusoidal basis functions, the (1,0), (1,2), (2,0), (2,1), (3,0), (3,2), (5,0), (7,0) and (9,0) modes were used for the $+45^\circ$-directed current, while the same set of modes were also used for the $-45^\circ$-directed current. The feed networks were modelled with Sonnet's circuit analysis module. Once again, due to the size of the antenna array, it was only modelled with the SDMM. Table 4.12 illustrates how the computer-memory requirements of the SDMM would compare to that of IE3D and FEKO. It can be seen that, for a non-iterative solution, the memory requirements of the two commercial codes would far outweigh the available memory on any personal computer. For the SDMM, the amount of duplicate entries in the interaction matrix equates to 98.89%.

**Table 4.12**
Computer memory required for the storage of the interaction matrix associated with the eighty-element $\pm 45^\circ$ slant-polarised antenna array.

| Method | Unknowns | Memory |
|---|---|---|
| IE3D | 81520 | 99.0 GB (estimated) |
| FEKO | 58240 | 50.5 GB (estimated) |
| SDMM | 2240 | 76.6 MB |

Figure 4.60 shows the coupling between some of the subarrays. This includes coupling between co-polar ports (e.g. two $+45^\circ$ ports), as well as coupling between cross-polar ports (e.g. a $+45^\circ$ port and a $-45^\circ$ port). As shown in Figure 4.59, subarray 1 represents a subarray at the edge of the array, while subarray 5 represents a subarray in the middle of the array. Figure 4.60(a) shows the coupling between subarray 1 and all of the other subarrays, while Figure 4.60(b) shows the coupling between subarray 5 and all of the other subarrays. From these two figures, it can be seen that the coupling between the subarrays is substantially higher than the coupling for the configuration in Figure 4.56.

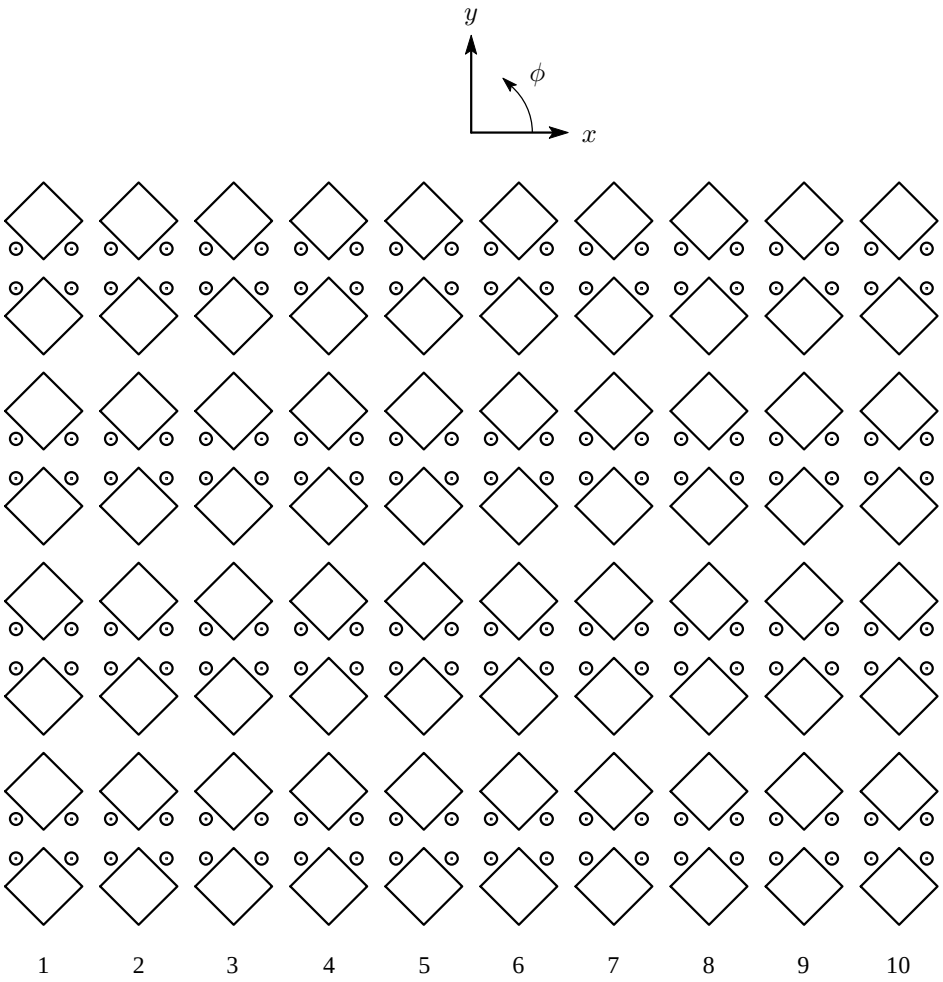


**Figure 4.59** Geometry of the eighty-element $\pm 45^{\circ}$ slant-polarised array. This array consists of ten linear subarrays that are positioned next to each other.

Figure 4.61 shows the simulated co-polarised and cross-polarised radiation patterns in the azimuth and elevation planes of the antenna array when all the co-polar ports are driven with equal amplitude and phase. It can be seen that the ten subarrays narrows the beamwidth in the azimuth plane significantly. However, the cross-polar discrimination of this array is not good at all. It appears to be only about 10 dB.

The results in this section and the previous section show that the layout of the antenna elements is very important when good isolation between subarrays, as well as low cross-polarisation levels, is required. In terms of these requirements, the zig-zag configuration of Figure 4.56 is definitely superior.

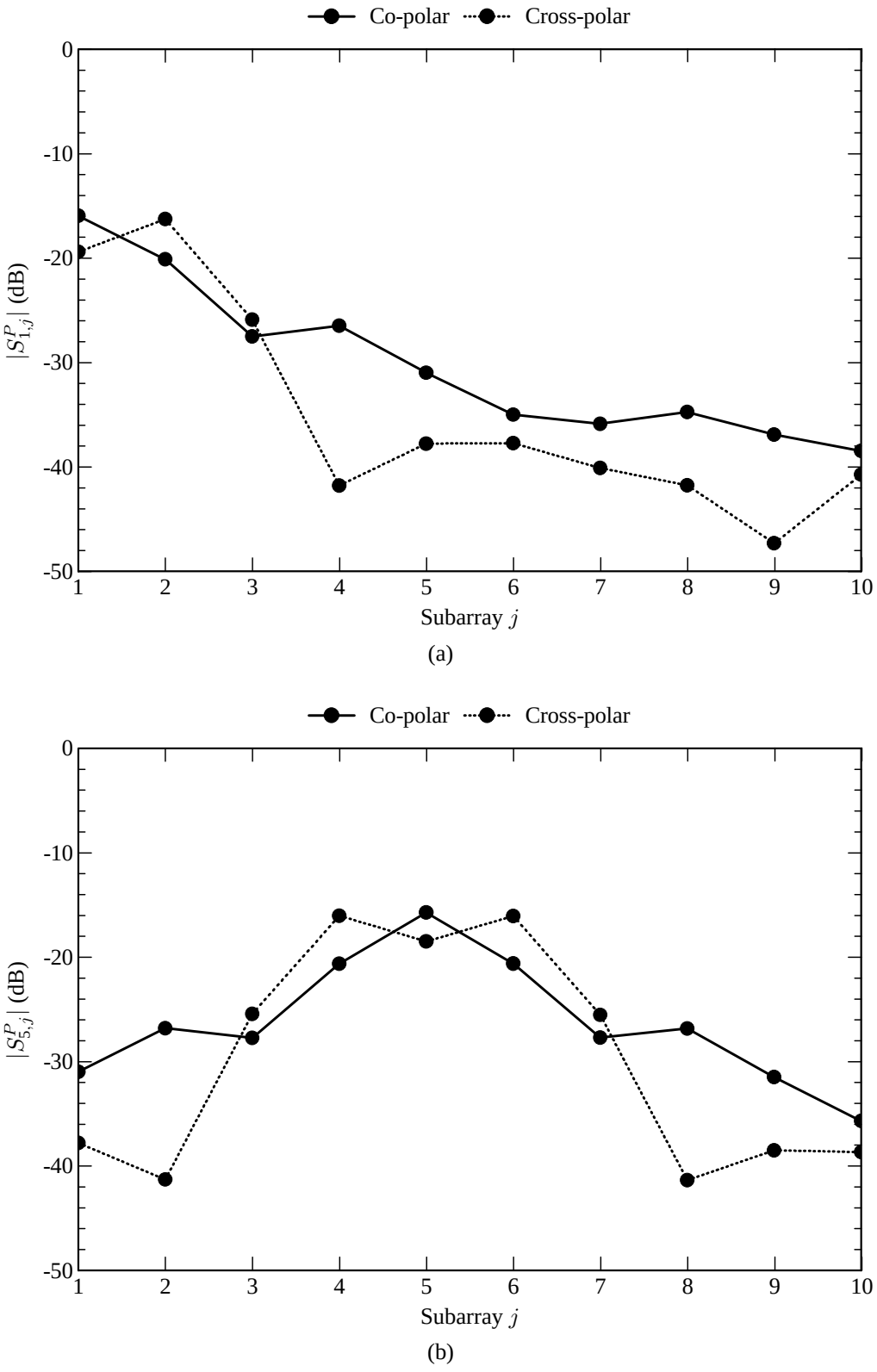


**Figure 4.60** Co-polar and cross-polar coupling (at 1.8 GHz) between the linear subarrays of the eighty-element $\pm 45^\circ$ slant-polarised array. (a) Coupling to subarray 1. (b) Coupling to subarray 5.

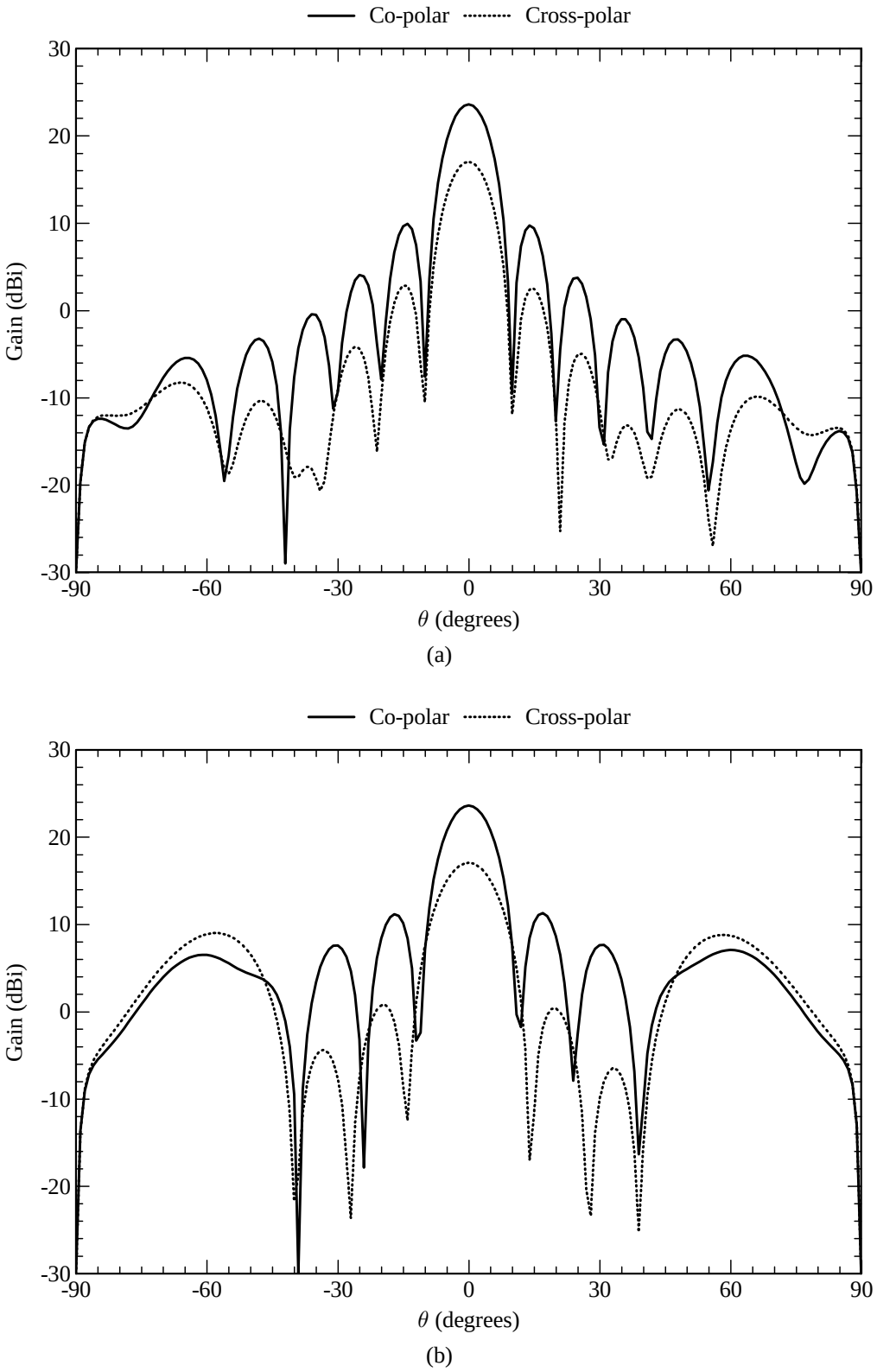


**Figure 4.61** Radiation patterns (at 1.8 GHz) of the eighty-element $\pm 45^{\circ}$ slant-polarised array when the co-polar ports are excited with equal amplitude and phase. (a) Radiation pattern in the azimuth plane ($\phi = 0^{\circ}$). (b) Radiation pattern in the elevation plane ($\phi = 0^{\circ}$).

## 4.5 ALTERNATIVELY-SHAPED PATCHES

So far, only antenna elements with rectangular resonant patches have been investigated. However, it is possible to use alternative shapes for the resonant patches. Two shapes that have been found to be useful, are the circular patch and annular-ring patch. Figures 4.62 and 4.63 depict the geometry of two antenna elements that were designed to operate at a centre frequency of more or less 1.8 GHz. The annular ring was designed to operate in its $TM_{11}$ mode. The capacitive feed probe is an ideal feeding mechanism for the annular ring as it is impossible to obtain an impedance match for the annular ring in its $TM_{11}$ mode when using a direct feed to the ring. This happens to be the case even when using thin substrates.

The antenna elements in Figures 4.62 and 4.63 were analysed with IE3D, as the SDMM implementation in this thesis only applies to antenna elements with rectangular resonant patches. For verification purposes, a physical model of each antenna element was constructed on a 150 mm $\times$ 150 mm ground plane. Both these antenna elements have impedance loci that are very similar to that of the antenna element with the rectangular resonant patch. Table 4.13 shows the measured and simulated 10 dB return-loss bandwidths of the two antenna elements. The measured and simulated bandwidth values compare very well, while they are also comparable to that of the antenna element with a rectangular resonant patch.

**Table 4.13**
Measured and simulated 10 dB return-loss bandwidths of the antenna elements with alternatively-shaped patches.

| | Circular | Annular ring |
|---|---|---|
| Measured | 27.9% | 26.1% |
| IE3D | 26.8% | 25.9% |

Figure 4.64 shows the measured and simulated radiation patterns in the *E*-plane and the *H*-plane of the antenna element with a circular resonant patch, while Figure 4.65 shows the same for the the antenna element with a annular-ring resonant patch. The corresponding gain values are shown in Table 4.14. All the measured and simulated results compare favourably, while the radiation patterns and gain values of the two elements are also very similar.

**Table 4.14**
Measured and simulated gain values of the antenna elements with alternatively-shaped patches.

| | Circular | Annular ring |
|---|---|---|
| Measured | 8.6 dBi | 8.5 dBi |
| IE3D | 8.8 dBi | 8.0 dBi |

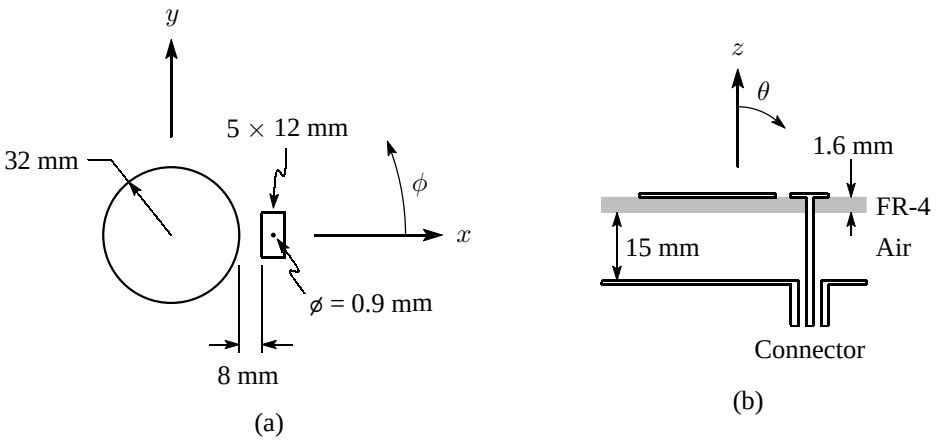


**Figure 4.62** Geometry of the antenna element with a circular resonant patch. (a) Top view of the antenna element. (b) Side view of the multilayered substrate with $\varepsilon_r = 4.25$ and $\tan\delta_\varepsilon = 0.02$ for the FR-4 layer and with $\varepsilon_r = 1$ and $\tan\delta_\varepsilon = 0$ for the air layer.

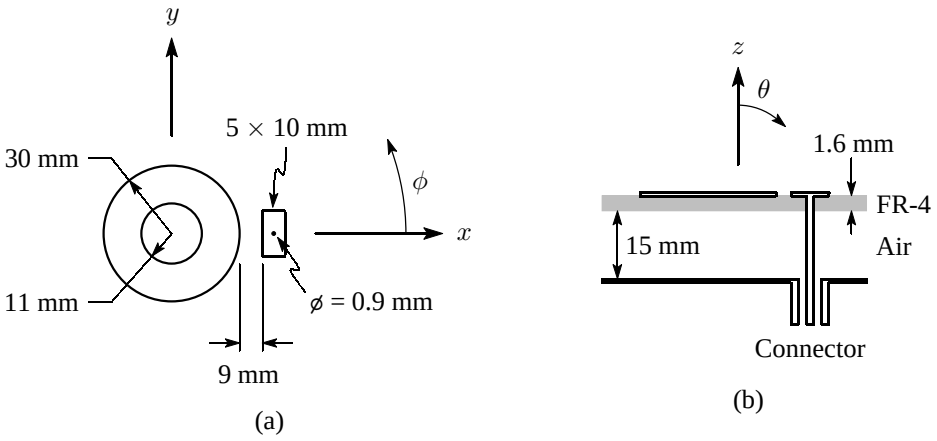


**Figure 4.63** Geometry of the antenna element with an annular-ring resonant patch. (a) Top view of the antenna element. (b) Side view of the multilayered substrate with $\varepsilon_r = 4.25$ and $\tan\delta_\varepsilon = 0.02$ for the FR-4 layer and with $\varepsilon_r = 1$ and $\tan\delta_\varepsilon = 0$ for the air layer.

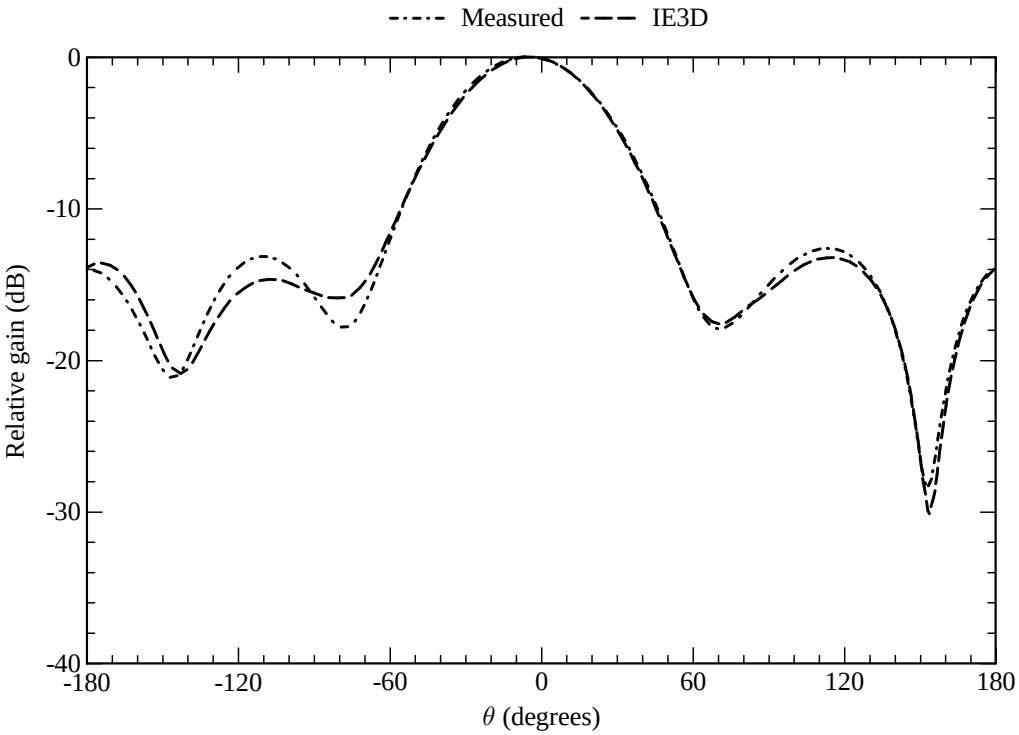


(a)

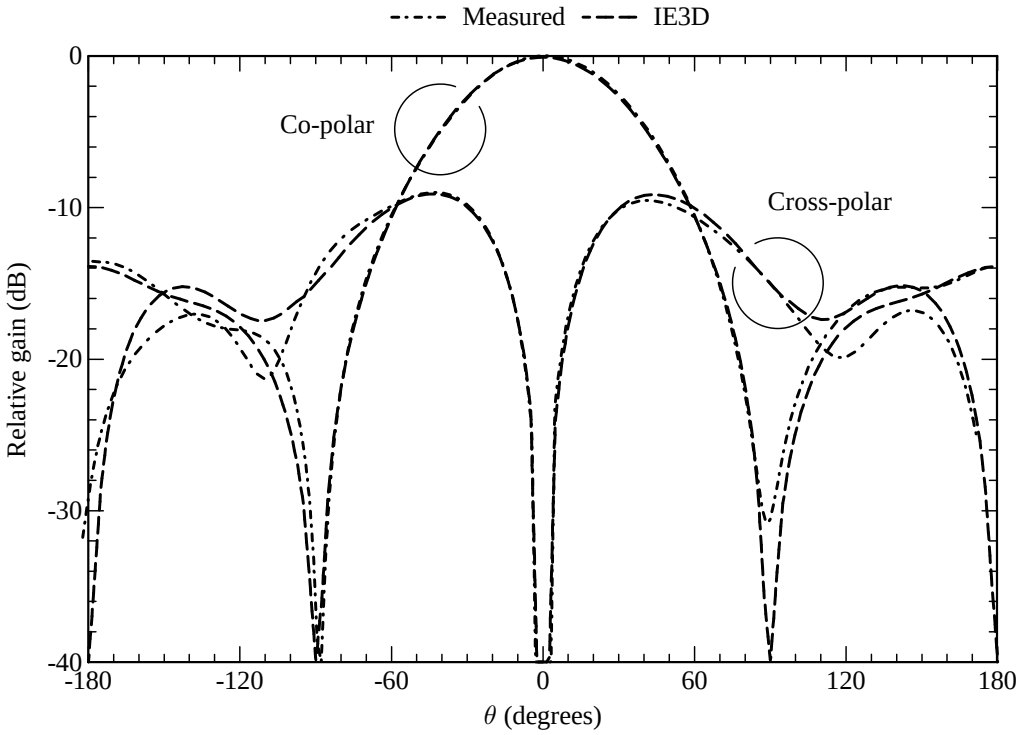


(b)

**Figure 4.64** Radiation patterns (at 1.8 GHz) of the antenna element with a circular resonant patch. (a) Co-polar radiation pattern in the *E*-plane ($\phi = 0^\circ$). (b) Co-polar and cross-polar radiation patterns in the *H*-plane ($\phi = 90^\circ$).

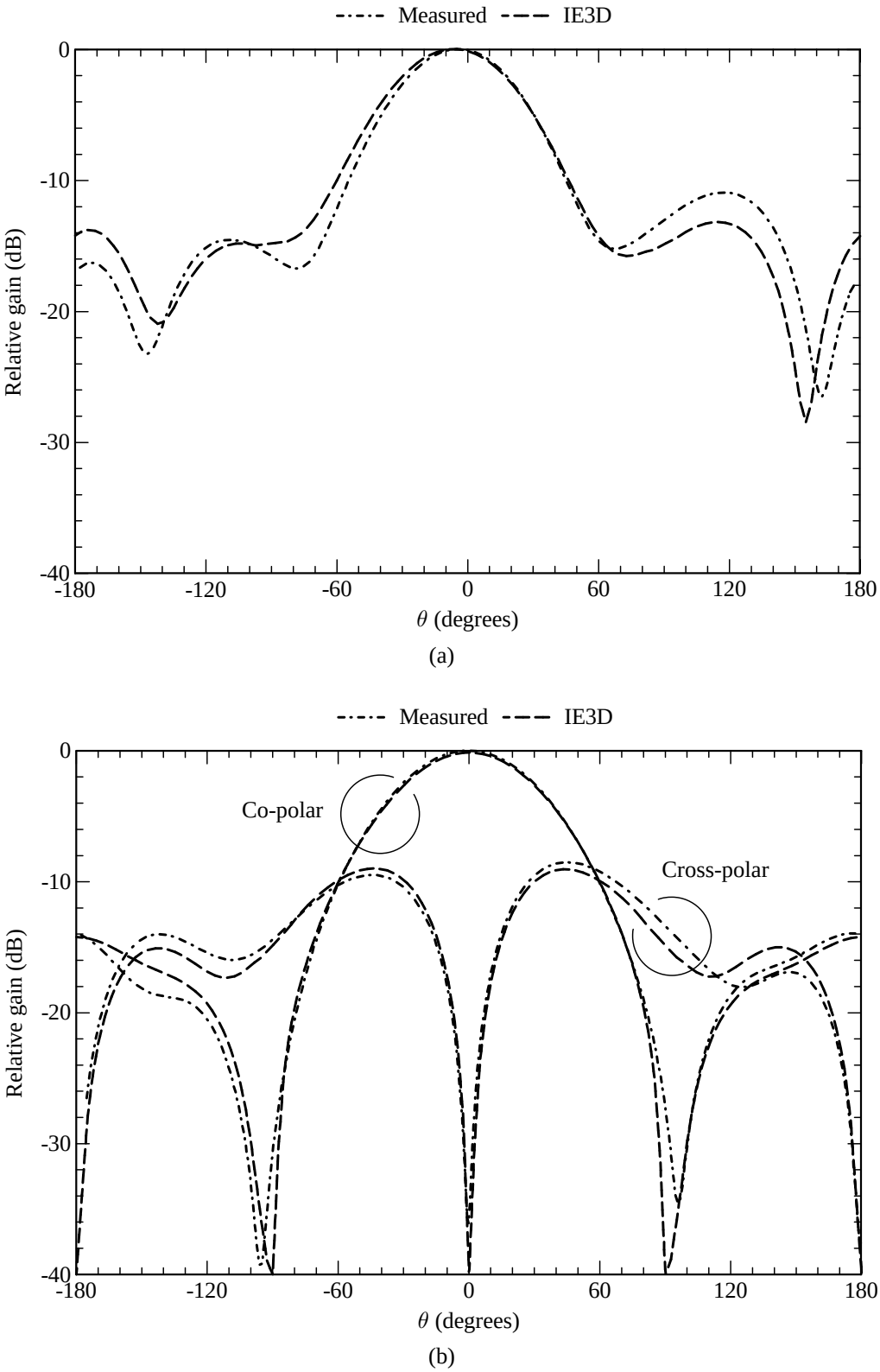


**Figure 4.65** Radiation patterns (at 1.8 GHz) of the antenna element with an annular-ring resonant patch. (a) Co-polar radiation pattern in the *E*-plane ($\phi = 0^\circ$). (b) Co-polar and cross-polar radiation patterns in the *H*-plane ($\phi = 90^\circ$).

## 4.6 CONCLUDING REMARKS

This chapter presented a number of numerical and experimental results, in order to verify that the SDMM implementation is accurate, to characterise the new antenna elements and to show how they can be used for different applications.

The SDMM implementation was verified by first analysing isolated parts of the antenna elements, such as the probes and probe-fed capacitor patches. The results compares favourably to published data. The circular and rectangular attachment-mode approaches were weighed up against each other in terms of their abilities to model rectangular probe-fed patches of various sizes and on various substrate thicknesses. It turned out that the circular attachment mode is more versatile than the rectangular attachment mode. The rectangular attachment mode was unable to model the electric current density on very small probe-fed patches, such as those that are used for the capacitor patches. The higher-order circular attachment mode proved to be quite successful for the modelling of the electric current density on the circular capacitor patches. Most importantly, the SDMM implementation also proved to be accurate for the analysis of complete antenna elements, consisting of a resonant patch that is excited by a small probe-fed capacitor patch. Throughout, the SDMM results compared well with published results, measurements and the results of other commercial codes.

The new antenna elements were characterised in order to show how the various dimensions of the structure affects the input impedance and impedance bandwidth of the antenna element. This knowledge is very important in the design of such elements or antenna arrays consisting of such elements. It was shown that the size of the capacitor and the gap width between the capacitor patch and the resonant patch, are the two important parameters for controlling the input impedance of the antenna element. The size of the capacitor patch has a more profound effect on the input reactance, while the gap width largely affects the input resistance. The bandwidth of the antenna element increases together with the thickness of the air substrate, but only to a certain point, after which it would appear that the gap width between the capacitor patch and the resonant element becomes too large. Also, for a rather thin air substrate, the capacitor patch cannot be placed close enough to the resonant patch, therefore also placing a lower limit on the impedance bandwidth. On the high end, it was shown that impedance bandwidths of well over 30% can be achieved for a VSWR of 2:1.

It was also shown how the antenna element can be used in a number of different applications. The examples included linear vertically-polarised arrays, linear horizontally-polarised arrays, as well as a number of $\pm 45^{\circ}$ slant-polarised arrays. These are often required in applications such as cellular communications. Some of the arrays that were analysed, are electrically large and served as good examples to show how efficient the SDMM implementation is in terms of computer-memory requirements. For a fixed amount of computer memory, the SDMM implementation can be used

to analyse much larger arrays than what is possible with the commercial codes. Throughout all the applications that were presented, the simulation results of the SDMM also compared well with measurements and the results of the two commercial codes that were used.

One feature of the SDMM implementation that proved to be very successful, is the identification of duplicate entries within the interaction matrix. This is done so that these entries do not need to be evaluated more than once. Figure 4.66 shows a typical relation between the number of unknowns and the number of entries in the interaction matrix that has to be evaluated after all the duplicate entries have been identified. The relation in Figure 4.66 is based on the problems that were solved in this chapter and is of course very dependant on the antenna geometry and types of basis functions that are used. However, it can be seen that, in general, it would appear that there is a linear relation between the number of entries to be evaluated and the number of unknowns. Without this feature, the number of entries to be evaluated would be proportional to the square of the number of unknowns. As shown in Figure 4.67, it turned out that the time required to evaluate the relevant entries in the interaction matrix, also has a linear relation with the number of unknowns. Once again, this is based on the problems that were analysed in this chapter.

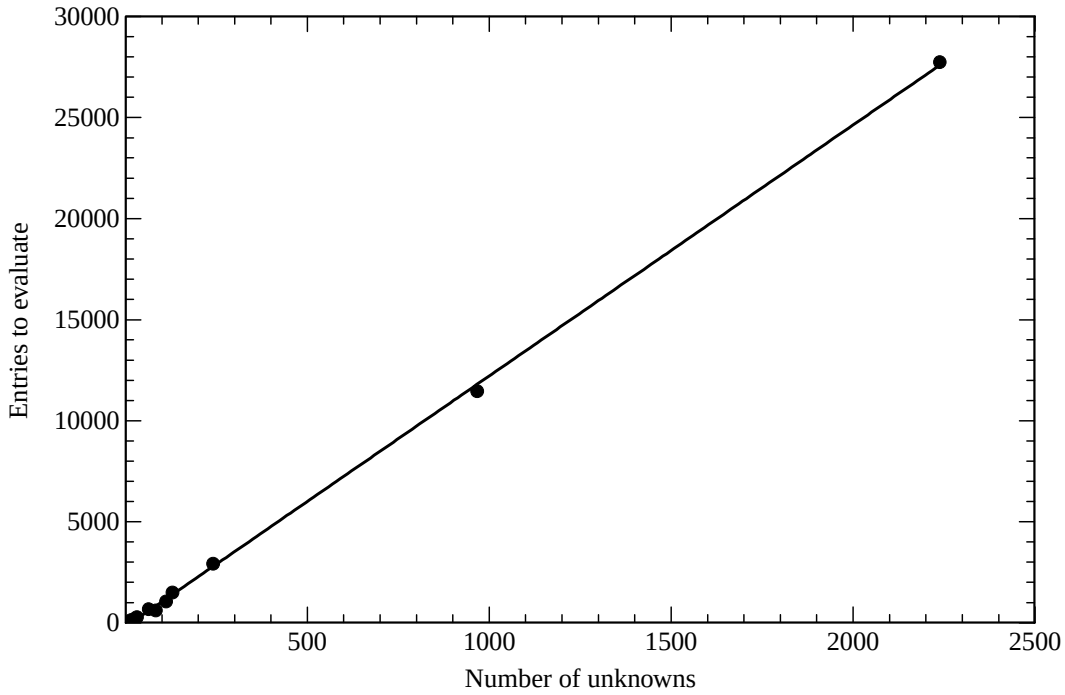


**Figure 4.66** Number of entries in the interaction matrix of the SDMM that has to be evaluated after all duplicate entries have been identified.

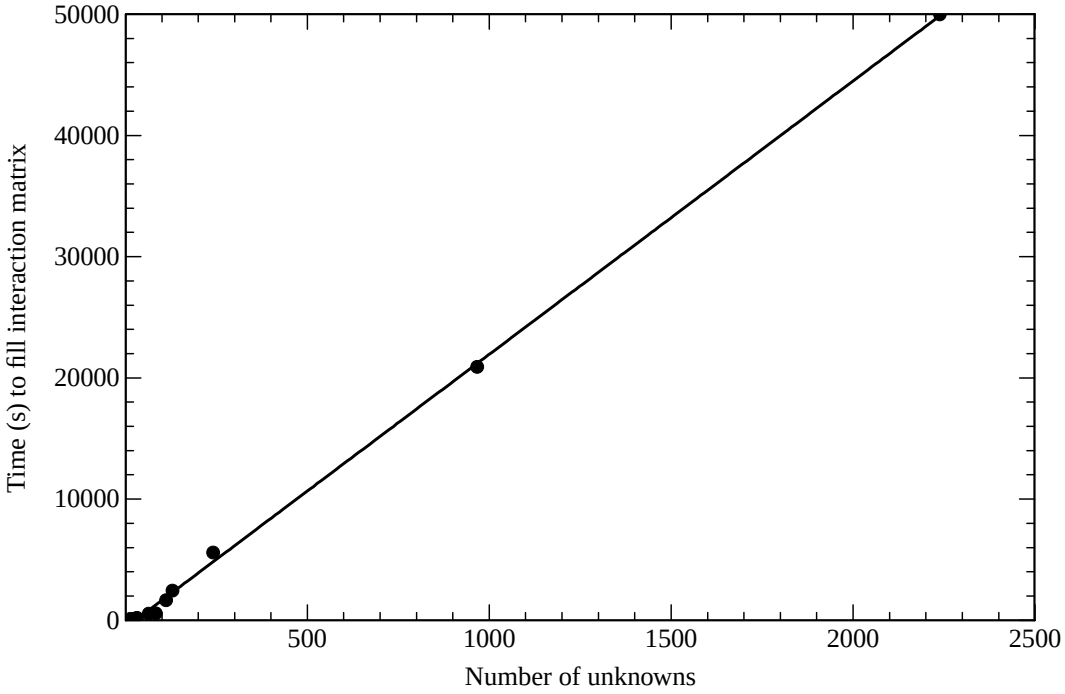


**Figure 4.67** Time required to fill the interaction matrix of the SDMM on a 2.6 GHz Pentium 4 processor at one frequency point.